



## Supplementary Materials for

### **Observing the cell in its native state: Imaging subcellular dynamics in multicellular organisms**

Tsung-Li Liu,\* Srigokul Upadhyayula,\* Daniel E. Milkie, Ved Singh, Kai Wang, Ian A. Swinburne, Kishore R. Mosaliganti, Zach M. Collins, Tom W. Hiscock, Jamien Shea, Abraham Q. Kohrman, Taylor N. Medwig, Daphne Dambournet, Ryan Forster, Brian Cunniff, Yuan Ruan, Hanako Yashiro, Steffen Scholpp, Elliot M. Meyerowitz, Dirk Hockemeyer, David G. Drubin, Benjamin L. Martin, David Q. Matus, Minoru Koyama, Sean G. Megason, Tom Kirchhausen, Eric Betzig†

\*These authors contributed equally to this work.

†Corresponding author. Email: [betzige@janelia.hhmi.org](mailto:betzige@janelia.hhmi.org)

Published 20 April 2018, *Science* **360**, eaq1392 (2018)

DOI: 10.1126/science.aq1392

#### **This PDF file includes:**

Supplementary Text  
Figs. S1 to S20  
Table S1  
Captions for Movies S1 to S8  
References

#### **Other Supplementary Material for this manuscript includes the following:**

(available at [www.sciencemag.org/content/360/6386/eaq1392/suppl/DC1](http://www.sciencemag.org/content/360/6386/eaq1392/suppl/DC1))

Movies S1 to S8

Contents: Adaptive Optics Lattice Light Sheet Microscopy Supplementary Material

<u>Section</u>	<u>Page</u>
SUPPLEMENTARY NOTES .....	4
1. Detailed Optical Path .....	4
a. Laser Combiner.....	4
b. Lattice Light Sheet Path.....	4
c. Detection Correction Path.....	5
d. Excitation Correction Path.....	6
2. Correction of aberrations in the detection light path .....	7
a. Calibration of deformable mirror.....	7
b. Determination and correction of system aberrations .....	7
c. Calibration of Shack-Hartmann wavefront sensor.....	8
d. Correction of sample induced aberrations .....	8
3. Correction of aberrations in the excitation light path .....	10
a. Calibration of spatial light modulator .....	10
b. Determination and correction of systems aberrations.....	10
c. Calibration of Shack-Hartmann wavefront sensor.....	10
d. Correction of sample induced aberrations .....	11
4. Estimation of curvature-induced tip/tilt/displacement of a lattice light sheet .....	13
5. AO correction and autofocus sequence.....	15
6. Sample Preparation and Imaging Conditions .....	18
a. Ethics statements.....	18
b. Zebrafish .....	18
c. Gene-edited intestinal epithelial organoids.....	19
d. Isolated gene-edited human breast epithelial cells.....	21
e. C. elegans.....	22
f. Arabidopsis .....	22
7. DNA Sequences for the Zebrafish constructs used to label intracellular markers .....	22
a. tagRFPT 3xGGS linker Dr.sec61 (endoplasmic reticulum and nuclear envelope).....	22
b. Dr.clta 3xGGS linker mNeonGreen (clathrin light chain A).....	23

c.	Dr.b4galt1(1-60) 3xGGS linker mNeonGreen (trans-Golgi apparatus) .....	24
d.	Dr.cox8a(1-34) 3xGGS linker mCardinal (mitochondria).....	24
e.	Tg(actb2:mem-mCardinal) <sup>hm36</sup> (Mm.2x-lyn(1-16); linker; mCardinal) .....	25
8.	Image Analysis & Visualization .....	25
a.	Simultaneous detection of multicellular boundaries in zebrafish embryos .....	26
b.	Segmentation of the cell nucleus based on signal exclusion .....	26
c.	Segmentation of the trans-Golgi apparatus.....	27
d.	Surface area and volume of segmented objects .....	27
e.	Tracking of crawling immune cells .....	27
f.	3D detection of diffraction limited fluorescent spots .....	28
g.	Trajectories and lifetimes of coated pits and vesicles and endocytic rates.....	28
h.	Relative intracellular location of organelles in a dividing cell in the brain zebrafish embryo .....	29
i.	Software-aided displacement.....	29
j.	Wavefront Reconstruction for Visualization .....	30
9.	Control Electronics .....	30
	Supplementary Figures .....	31
	Supplementary Table .....	53
	Captions for Supplementary Movies .....	55
	Full Reference List:.....	63

## SUPPLEMENTARY NOTES

### 1. Detailed Optical Path

The detailed optical layout of the AO-LLSM is shown in fig. S1.

#### *a. Laser Combiner*

The combiner housed six lasers: 405 nm (250mW, RPMC, Oxxius LBX-405-300-CIR-PP), 445 nm (100mW, RPMC, Oxxius LBX-445-100-CIR-PP), 488 nm (300 mW, MPB Communications, 2RU-VFL-P-300-488-B1R), 560 nm (500 mW, MPB Communications, 2RU-VFL-P-500-560-B1R), 589 nm (500 mW, MPB Communications, 2RU-VFL-P-500-589-B1R) and 642 nm (500 mW, MPB Communications, 2RU-VFL-P-500-642-B1R). As described previously (6), each beam was independently expanded to a  $1/e^2$  diameter of 2.5mm and aligned such that they were translated vertically with respect to each other. The beams were then focused onto an acousto-optic tunable filter (AA Quanta Tech, Optoelectronic AOTF AOTFnC-400.650-TN) and expanded using 150 mm and 200 mm FL lenses (25mm dia, Edmunds 49-362, 49-364), respectively.

#### *b. Lattice Light Sheet Path*

The light sheet excitation path was designed as described previously (6). Up to three different laser wavelengths could be used for a given experiment. Following the AOTF, the beams were passed through a half wave plate (HWP1, Thorlabs, AHWP10M-600) and a pair of cylindrical lenses (CL1, 25 mm FL/12.5 mm dia, Edmund NT68-160, and CL2, 200 mm FL/25.4 mm dia, Thorlabs, ACY254-200-A) to expand them along the  $x$  axis. Each elliptically expanded beam illuminated a thin horizontal stripe on a greyscale spatial light modulator (VIS-SLM, Holoeye, PLUTO-Vis-014), with the stripes vertically separated by 1.5 mm from one another. The light diffracted by the SLM was then focused by a 400 mm FL lens (L20, 40mm dia, Edmunds 49-386) onto an annular mask (MSK, Photo Sciences Inc) to physically block the zeroth order and any other unwanted diffraction orders. The desired diffracted light was then demagnified by 0.75x (using achromatic lens pair L19, 300 mm FL/40 mm dia, Edmunds 49-385 and L18, 225mm FL/25mm dia, Edmunds 49-365), and reflected from a pair of galvanometer mirrors (G3 & G4, 3 mm mirror, Cambridge Tech Inc, 8315H), conjugated to one another with two more achromatic lenses (L16 & L17, 100 mm FL/25 mm dia, Edmunds 49-360), that scan the light sheet along the

$x$  and  $z$  axes. Following the galvos, the light passed through a transform lens (L15, 50 mm FL/25 mm dia, Edmunds 49-356) and reflected from a sample-conjugate resonant galvanometer (Electro-Optical Products Corp. 7 x 8 mm, SC-30) used to wobble the light sheet in the  $xy$  plane before passing through a relay lens (L14, 50 mm FL/25 mm dia, Edmunds 49-356) and a 3.2x beam expander (L13, 125 mm FL/25 mm dia, Edmund 49-361, and L12, 400 mm FL/25 mm dia, Edmund 47-650) to conjugate the annular mask and the scanning galvos to the back focal plane of a custom manufactured excitation objective (EO, Special Optics, 0.65 NA, 3.74 mm WD). The resulting light sheet within the specimen then generated fluorescence that was collected by the detection objective (DO, Nikon, CFI Apo LWD 25XW, 1.1 NA, 2 mm WD), projected onto the deformable mirror (DM, ALPAO 97-15) using an achromatic lens pair (L1, 400 mm FL/40 mm dia, Edmunds 49-386 and L2, 300mm FL/40mm dia, Edmunds 49-385), and demagnified with another lens pair (L3, 400 mm FL/40 mm dia, Edmunds 49-386, and L4, 85 mm FL/25 mm dia, Edmunds 49-359), and focused onto an sCMOS camera (CAM1, Hamamatsu Orca Flash 4.0 v2) with a final lens (L5, 85 mm FL/25 mm dia, Edmunds 49-359) at an overall magnification of 66.7x. As noted earlier, two inspection cameras (ACE2 & ACE1, Basler acA1600-60gm and acA2040-25gm GigE, respectively) conjugate to either the sample plane or the back focal plane of EO were installed to help verify the alignment. An epifluorescence objective (EPO, Olympus LUMPLFLN40XW, 0.8 NA, 3.3 mm WD) with a large field of view was also included to image the specimen from below the sample chamber in order to locate the region of interest.

### *c. Detection Correction Path*

In order to correct sample-induced aberrations in the detection path, infra-red light (red) from a Ti:Sapphire ultrafast pulsed laser (Coherent, Chameleon Ultra II) was first passed through a Pockel cell (Conoptics 350-80, controller 302 RM) to control the intensity of TPE at the focus of the detection objective (DO). It was then ported to the detection arm of the LLSM by a switching galvanometer (3 mm mirror, Cambridge Technology, 8315H) and expanded to a  $1/e^2$  diameter of 3 mm by a relay lens pair (L11, 30 mm FL/25 mm dia, Thorlabs AC254-30 and L10, FL/25 mm dia, Thorlabs AC254-075). The expanded beam was then reflected from a pair of scanning galvanometer mirrors (G1 & G2, 3 mm mirror, Cambridge Technology, 6215H) conjugated to one another by a pair of matched focal length achromatic relay lenses (L5 & L6, 100mm FL/25 mm dia, Edmunds 49-360), reflected from a switching galvo (G6, 10 mm mirror, Cambridge Technology, 6230HM50) that directs emission light to either the imaging camera or the detection wavefront sensor, and sent to the deformable mirror by another conjugate lens pair (L3, 400 mm FL/40 mm dia, Edmunds 49-386, and L4, 85 mm FL/25 mm dia, Edmunds 49-359). From there, a pair of conjugation lenses (L1, 400 mm FL/40 mm dia, Edmunds 49-386 and L2, 300mm

FL/40mm dia, Edmunds 49-385) was used to send the TPE beam into the rear pupil of DO, where it created a scanning fluorescent guide star within the specimen.

On return, the TPE-induced fluorescence was collected by DO, reflected off the deformable mirror, and directed by switching galvo G6 to galvos G1 & G2, where it was descanned. It was then reflected by a dichroic mirror (Semrock, 801 nm edge BrightLine® single-edge dichroic beamsplitter FF801-Di02-25x36, 25.2 mm x 35.6 mm x 1.1 mm), and magnified 2.25x by a lens pair (L7, 100 mm FL/25 mm dia, Edmunds 49-360, and L8, 225mm FL/25mm dia, Edmunds 49-365 achromatic relay lenses) before being directed onto a Shack-Hartmann wavefront sensor consisting of a microlens array (LA1, Edmunds 64-483, 10 x 10mm, 500 $\mu$ m Pitch, 0.25° Divergence, Plano-Convex 46.7 mm EFL), an emission filter (Semrock 680 nm blocking edge BrightLine® multiphoton short-pass emission filter FF01-680/SP-25, 25 mm x 3.5 mm) and an EMCCD camera (CAM2, Andor iXon 3, model DU8201 BV).

#### *d. Excitation Correction Path*

In order to correct sample-induced aberrations in the excitation path, the aforementioned switching galvo G7 was used to direct the Ti:Sapphire laser beam to the excitation arm, where it was expanded to a  $1/e^2$  diameter of 4 mm through relay lenses (L25, 30 mm FL/25 mm dia, Edmund 49-352-INK, and L24, 100 mm FL/25 mm dia, Edmund 49-360), and inserted into the excitation path by reflecting off a dichroic mirror (DC2, Semrock, FF670-SDi01-25x36 670 nm edge BrightLine® multiphoton short-pass dichroic beamsplitter 25.2 mm x 35.6 mm x 1.1 mm). Thereafter it was reflected by the same pair of galvos G3 & G4 used for scanning the light sheet, and sent to the excitation objective EO. The TPE guide star fluorescence thereby generated within the sample was then collected by EO, reflected back off galvos G3 & G4 to descann the guide star, reflected from a dichroic filter (DC3, 405/488/561 nm or 442/488/561 nm, Yokogawa dichroic beamsplitter, Di01-T405/488/561 or Di01-T442/488/561-13x15x0.5 13 mm x 15 mm x 0.5 mm), and magnified 1.8x (by achromatic lenses L21, 125 mm FL/25 mm dia, Edmunds 49-361 and L22, 225mm FL/25mm dia, Edmunds 49-365) to match the input pupil of a Shack-Hartmann wavefront sensor consisting of a microlens array (LA2, Edmunds 64-479, 10 x 10mm, 500 $\mu$ m Pitch, 1.2° Divergence, Plano-Convex 13.8 mm EFL) focused onto an EMCCD camera (CAM2, Andor iXon EM+, model DU-897E-CSO-BV).

## 2. Correction of aberrations in the detection light path

### a. Calibration of deformable mirror

Using a homebuilt Michaelson interferometer, we directly measure the phase  $\Phi_{DMoff}(x', y')$  introduced by the deformable mirror (DM, ALPAO DM97) in its initial state when zero voltage applied. We then measure the change from this phase across the entire mirror when we apply voltage to each of its 97 actuators, one by one. This yields a set of  $I = 97$  linearly independent impulse functions  $\Phi_i(x', y')$  which serves as a basis set for decomposition of any arbitrary pupil phase function. In particular, the pupil phase can be described by a sum over orthogonal Zernike polynomials  $Z_n^m(x', y')$ ,  $m = -n, -n+2 \dots n-2, n$  and each Zernike polynomial can be approximated by a linear combination of the measured impulse functions:

$$Z_n^m(x', y') = \sum_{i=1}^{97} a_{imn} \Phi_i(x', y') \quad (1)$$

Empirically, we have found here and elsewhere (11) that the Zernike polynomials up through  $n=9$  (a total of 55 polynomials) are sufficient to describe the aberrations we have seen in the systems we have studied. The coefficients  $a_{imn}$  tell us individual actuators voltages needed to generate any desired Zernike mode of any desired amplitude from the DM.

### b. Determination and correction of system aberrations

With the DM installed in the complete microscope, we record seven different 2D images of a 100 nm diameter fluorescent bead on a cover slip at the detection path camera CAM1 (Hamamatsu, Orca Flash 4.0 v2 sCMOS, fig. S1) as we apply seven different Zernike modes (flat phase, +/- defocus, +/- x astigmatism, and +/- y astigmatism) of  $2\lambda$  amplitude, one after the other, to the DM. Phase retrieval (44) based on the Gerchberg-Saxton algorithm (45) then yields the aberration  $\Phi_{sys}(x', y')$  introduced by the microscope itself. The inverse of this aberration is then decomposed into Zernike modes:

$$-\Phi_{sys}(x', y') = \sum_{n=0}^9 \sum_{m=-n}^n b_{mn} Z_n^m(x', y') \quad (2)$$

From Eqs. (1) and (2), the actuator voltages needed to cancel system aberrations are given by:

$$V_i^{syscorr} = \sum_{n=0}^9 \sum_{m=-n}^n a_{imn} b_{mn} \quad (3)$$

These voltages are then applied to DM to bring the detection path to diffraction-limited performance, so that all comparisons of performance before and after AO that follow thereafter refer to only sample-induced aberrations.

*c. Calibration of Shack-Hartmann wavefront sensor*

Pulsed light from an ultrafast Ti:sapphire laser (Coherent Cameleon Ultra) is reflected from galvanometers G1 and G2 (Cambridge Technology, 6215H, fig. S1) as well as DM and focused through the detection objective (DO, Nikon CFI Apo LWD 25XW, 1.1 NA, 2 mm WD) to excite fluorescent dye solution in the imaging chamber, thereby creating a scanning guide star (GS). Light from GS collected with DO is then descanned by back reflection off galvos G1 and G2 and sent to the input pupil of the Shack-Hartmann wavefront sensor DSH, which is conjugate to DM and the rear focal plane of DO. DSH consists of a 10 mm x 10 mm lenslet array of 0.5 mm pitch and 46.7 mm focal length (LA1, Edmunds 64-483) focused on camera CAM2 (Andor iXon 3). With DM set for detection path system correction, the light from GS creates an array of  $J = 12 \times 12$  focal spots on CAM2 of DSH whose locations serve as the reference positions for wavefront measurement. Thereafter, displacement  $(x'_j, y'_j)$  of each spot from its reference position is proportional to the local slope of the wavefront, mapped back to the pupils of DO and DM, due to sample-induced aberrations and/or corrective patterns applied to DM.

To complete the calibration of DSH, it is also necessary to measure, within the assembled microscope, the spot displacements produced by an orthogonal basis set of corrective patterns at DM. This permits us to take into account small misalignments between DM and DSH and the optics in between. To do so, a scanning GS is generated as above and the spot positions  $(x'_{jmn}, y'_{jmn})$  are recorded as each of the Zernike modes from Eq (1) through  $n = 9$  are applied in turn to DM. In principle, it would be possible to calibrate in terms of the spot displacements of the impulse functions  $\Phi_i(x', y')$  rather than Zernike modes. However, we choose to work through the intermediary of a Zernike expansion because: a) these modes have well defined physical meanings in terms of the aberrations to which they correspond (e.g., defocus, spherical aberration, astigmatism, etc.); and b) their measurement is influenced by spot displacements across the entire pupil, so they are less sensitive to a single bad displacement measurement than are the impulse functions, each of which is dominantly affected by at most a few such measurements.

*d. Correction of sample induced aberrations*

For post-calibration aberration correction, GS is first scanned over a series (usually five) of xy planes (in the coordinate system of DO) equally spaced axially within a presumed isoplanatic

volume inside the specimen, while the resulting fluorescence signal is integrated at DSH. The displacements  $(x_{err}'_j, y_{err}'_j)$  of the resulting spots on DSH represent the remaining wavefront error  $\Phi_{err}(x', y')$ , averaged over the isoplanatic volume, which must be corrected to achieve diffraction-limited performance within the specimen. However, since  $\Phi_{err}(x', y')$  can be expressed in terms of a Zernike expansion,

$$\Phi_{err}(x', y') = \sum_{n=0}^9 \sum_{m=-n}^n c_{mn} Z_n^m(x', y') \quad (4)$$

its displacements  $(x_{err}'_j, y_{err}'_j)$  can be expressed in terms of an expansion of the measured displacements  $(x'_{jmn}, y'_{jmn})$  of Zernike modes having the same coefficients:

$$(x_{err}'_j, y_{err}'_j) = \sum_{n=0}^9 \sum_{m=-n}^n c_{mn} (x'_{jmn}, y'_{jmn}) \quad (5)$$

The coefficients  $c_{mn}$  are determined by a weighted 2D least squares fit, with the weighting proportional to the intensity of each spot. Spots falling below a minimum intensity threshold are assigned a weighting of zero. Weighting ensures that displacements for which we have the highest confidence have the most influence in determining the modal structure of  $\Phi_{err}(x', y')$ , and that weak spots (such as those associated with marginal rays at the edge of the pupil that are more susceptible to scattering) or missing spots (such as those associated with rays that intersect absorptive bodies) do not introduce excessive error.

Finally, given  $c_{mn}$ , the voltages at DM required to achieve diffraction-limited performance within the isoplanatic volume are determined by combining Eqs (1) and (4):

$$V_i^{AOcorr} = \sum_{n=0}^9 \sum_{m=-n}^n a_{imn} c_{mn} \quad (6)$$

A key advantage of this approach is that it is photon efficient. In a typical round of aberration measurement,  $\sim 200$  photons/lenslet from  $\sim 100$  lenslets is sufficient to achieve an accurate correction. These photons are emitted from five planes across the isoplanatic volume, each typically  $\sim 400 \times 700$  pixels in xy extent (c.f., table S1), for an average contribution to the measurement of only  $\sim 0.014$  photons/pixel. Even if only 1% of these pixels contain fluorescent material, the photon load required from these only rises to 1.4 photons/pixel, or a minute fraction of the total photons emitted per pixel when imaging over the course of a typical time series.

### 3. Correction of aberrations in the excitation light path

#### a. Calibration of spatial light modulator

Using a homebuilt Michaelson interferometer, we directly measure the phase  $\Phi_{SLM}(0, x, y)$  introduced by an 8-bit, phase only spatial light modulator (SLM, Holoeye PLUTO-VIS-014, 1920 x 1080 pixels) when the grey level of all pixels is set to zero. We then measure, at each excitation wavelength  $\lambda$  that will be used for imaging, the change from this phase across SLM as several different grey levels from 0 to 255 are applied, and then interpolate to find a relationship between any grey level  $GL$  and phase change  $\Phi_{SLM}(GL, \lambda, x, y)$  it yields across SLM. In general, this relationship is constant across SLM:

$$\Phi_{SLM}(GL, \lambda, x, y) \approx \Phi_{SLM}(GL, \lambda) \quad (7)$$

and can be inverted to tell the grey level  $GL(\Phi, \lambda)$  at any pixel for any desired phase change  $\Phi$  at that pixel.

#### b. Determination and correction of systems aberrations

Because SLM is conjugate to the sample plane and not the rear pupil of the excitation objective (EO, Special Optics custom water immersion 0.7 NA lens), pupil-based phase retrieval as described above cannot be used to measure the aberration across the entire excitation path. Fortunately, at the lower NA of EO, the dominant source of aberration in this path is the phase  $\Phi_{SLM}^{err}(0, x, y)$  introduced by the deviation from flatness of SLM itself. Thus, if SLM is installed in the microscope in the same mount used during the measurement of  $\Phi_{SLM}^{err}(0, x, y)$  above, so that its shape does not change, then system correction is achieved by applying:

$$GL_{syscorr}(\lambda, x, y) = GL(-\Phi_{SLM}^{err}(0, x, y), \lambda(y)) \quad (8)$$

across SLM. The wavelength  $\lambda$  is a function of the row position  $y$  on SLM because the lattice light sheet pattern for every wavelength is written on the SLM at all times, with each pattern vertically offset from the next.

#### c. Calibration of Shack-Hartmann wavefront sensor

Calibration of the Shack-Hartmann excitation wavefront sensor (ESH) proceeds similarly to DSH. Light from the Ti:sapphire laser is ported to the excitation optical path by galvanometer G7 (3 mm mirror, Cambridge Technology, 6215H, fig. S1), reflected from galvanometers G3 and G4

(Cambridge Technology, 6215H) and focused through EO to excite fluorescent dye solution in the imaging chamber, thereby creating a scanning guide star (GS). Light from GS collected with EO is then descanned by back reflection off galvos G3 and G4 and ported by dichroic mirror DC3 to the input pupil of the Shack-Hartmann wavefront sensor ESH, which is conjugate to the rear focal plane of EO. ESH consists of a 10 mm x 10 mm lenslet array of 0.5 mm pitch and 13.8 mm focal length (LA2, Edmunds 64-479) focused on camera CAM3 (Andor iXon EM+). The light from GS creates an array of  $J = 12 \times 12$  focal spots on CAM3 of ESH whose locations serve as the reference positions for wavefront measurement. Thereafter, displacement  $(x'_j, y'_j)$  of each spot from its reference position is proportional to the local slope of the wavefront, mapped back to the pupils of EO, due to sample-induced aberrations.

*d. Correction of sample induced aberrations*

For post-calibration aberration correction, GS is first scanned over an  $xy$  plane (in the coordinate system of EO) axially centered within a presumed isoplanatic volume inside the specimen, and the displacements  $(x_{err\ j}, y_{err\ j})$  of the resulting spots on ESH are measured. These displacements represent the sample induced wavefront error  $\Phi_{sample}(x', y')$  which must be corrected to achieve diffraction-limited performance within the specimen.

There are two important differences between AO excitation and AO detection correction. First, because SLM is used for lattice generation as well as wavefront correction, the annular mask (MSK Photosciences Inc) must be in the beam path between SLM and EO in order to filter out unwanted diffraction orders. However, MSK cannot be in the beam path between ESH and EO, or else all but a narrow annular ring of the wavefront from GS would be blocked from reaching ESH. Thus, AO excitation correction occurs in open loop mode, where the spot displacements at ESH are independent of the wavefront applied at SLM. In contrast, AO detection correction occurs in closed loop mode, where DM is in the beam path between DSH and DO, and where the displacements at DSH represent a combination of the sample induced wavefront error and the current wavefront correction applied at DM.

The second difference is that, whereas DM is conjugate to the rear pupil of DO, SLM is conjugate to the sample plane, because we can generate a more precise lattice light sheet with greater efficiency there. However, if we additionally wish to use SLM for AO correction in order to save cost and reduce complexity, the corrective algorithm at the sample plane is more complex than simply applying the inverse of the measured wavefront error, as we do in the detection path. Instead, we start by considering the initial phase pattern at SLM required for system correction and lattice generation in the absence of sample-induced aberrations:

$$\Phi_{lattice}^{syscorr}(x, y, \lambda) = \Phi_{lattice}^{ideal}(x, y, \lambda) - \Phi_{SLM}^{err}(0, x, y) \quad (9)$$

If each lattice pattern is illuminated uniformly with its appropriate wavelength, this pattern produces an electric field at SLM of:

$$E_{lattice}^{syscorr}(x, y, \lambda) = e_o(\lambda) \exp\left[i\Phi_{lattice}^{syscorr}(x, y, \lambda)\right] \quad (10)$$

Since SLM is conjugate to the sample plane of EO, and the annular mask MSK is conjugate to the rear focal plane of EO, in the Fraunhofer approximation  $E_{lattice}^{syscorr}(x, y, \lambda)$  produces a corresponding electric field at MSK given by its 2D Fourier transform:

$$E_{mask}^{syscorr}(x', y', \lambda) = \mathbb{F}\left[E_{lattice}^{syscorr}(x, y, \lambda)\right] \quad (11)$$

where  $\mathbb{F}$  is the Fourier transform operator,  $x, y$  refer to coordinates in planes conjugate to the sample plane, and  $x', y'$  refer to coordinates in planes conjugate to the rear pupil of EO. After spatial filtering by the annular mask, this produces an electric field at the rear pupil plane of EO of:

$$E_{rear\_pupil}^{syscorr}(x', y', \lambda) = H(\rho_{max} - \rho)H(\rho - \rho_{min})\mathbb{F}\left[E_{lattice}^{syscorr}(x, y, \lambda)\right] \quad (12)$$

where  $H(x)$  is the Heaviside step function ( $H(x) = 0$  for  $x < 0$ ,  $H(x) = 1$  for  $x > 0$ ), and  $\rho_{max}$  and  $\rho_{min}$  are the maximum and minimum radii of the annulus, respectively.

Given this electric field in the rear pupil necessary to create the system corrected lattice pattern, and given that the sample induced aberration  $\Phi_{sample}(x', y')$  was measured by ESH at a plane also conjugate to the rear pupil, the total electric field at the pupil required to create an aberration corrected lattice within the specimen is given by subtracting  $\Phi_{sample}(x', y')$  from the phase of  $E_{rear\_pupil}^{syscorr}(x', y', \lambda)$ :

$$E_{rear\_pupil}^{total-corr}(x', y', \lambda) = H(\rho_{max} - \rho)H(\rho - \rho_{min})\mathbb{F}\left[E_{lattice}^{syscorr}(x, y, \lambda)\right] \exp\left[-i\Phi_{sample}(x', y')\right] \quad (13)$$

This can then be projected back to find the field at SLM required for complete correction by applying an inverse Fourier transform  $\mathbb{F}^{-1}$ :

$$E_{SLM}^{total-corr}(x, y, \lambda) = \mathbb{F}^{-1}\left[E_{rear\_pupil}^{total-corr}(x', y', \lambda)\right] \quad (14)$$

However, since SLM manipulates only phase and not amplitude, the pattern we apply to SLM to create an AO corrected lattice within the specimen is given by the phase of  $E_{SLM}^{total-corr}(x, y, \lambda)$ :

$$\Phi_{SLM}^{total-corr}(x, y, \lambda) = \text{Arg}\left[E_{SLM}^{total-corr}(x, y, \lambda)\right] \quad (15)$$

which, by the inversion of Eq (7), can be used to determine the grey level  $GL_{SLM}^{total-corr}(x, y, \lambda)$  required to generate the AO corrected lattice.

#### 4. Estimation of curvature-induced tip/tilt/displacement of a lattice light sheet

In addition to the classical optical aberrations defined by the Zernike modes, the penetration of a light sheet into a curved specimen of refractive index  $n_2$  different from the index  $n_1$  of the surrounding media for which EO is designed can result in yaw and pitch of the light sheet within the specimen (fig. S3). Yaw in the plane lateral to the axis of DO poses little problem as long as the camera field of view is adjusted to follow suit, but pitch at an angle  $\beta$  relative to the original light sheet direction, which is coincident with the focal plane of DO, raises the risk that the light sheet will no longer be in focus over the desired field of view  $y_{FOV}$ , either because the center of the light sheet is then axially displaced a distance:

$$z_{focus\_offset} = y_{penetration\_distance} \tan(\beta) \quad (16)$$

from its original position at the focal plane of DO (fig. S3) after it has penetrated a distance  $y_{penetration\_distance}$  within the specimen or, if an autofocus mechanism is used to bring  $z_{focus\_offset}$  to zero, because the light sheet is then axially displaced at the edges of the FOV with respect to the center position by:

$$\Delta z_{focus} = \pm y_{FOV} \tan(\beta) / 2 \quad (17)$$

We need to estimate these quantities to evaluate the risk of each.

To begin, by Snell's law, the angle  $\theta_2$  the pitch-deflected light sheet within the specimen makes with the vector (yellow line, fig. S3) normal to the surface of the specimen at the point of penetration is related to the angle  $\theta_1$  the incident light sheet makes with this same vector by:

$$\theta_2 = \sin^{-1}[n_1 \sin(\theta_1) / n_2] \quad (18)$$

From simple geometry (fig. S3) we then deduce the pitch angle:

$$\beta = \theta_1 - \theta_2 = \theta_1 - \sin^{-1}[n_1 \sin(\theta_1) / n_2] \quad (19)$$

from which  $\Delta z_{focus}$  and  $z_{focus\_offset}$  can be determined using Eqs (16) and (17).

Now we can make numerical estimates. We first consider the case where an autofocus mechanism has been used if necessary to return the center of the light sheet to the focal plane of DO, i.e.,  $z_{focus\_offset} = 0$ . In that case, we estimate that a tilted light sheet will remain in focus at the edges of the field of view if:

$$\Delta z_{focus} \leq z_{PSF}^{HWHM} \quad (20)$$

where  $z_{PSF}^{HWHM}$  is the half width at half maximum of the axial profile of the PSF of DO. Assuming  $\lambda = 520$  nm and an imaging buffer of  $n_1 = 1.34$ ,  $z_{PSF}^{HWHM} \approx 460$  nm at the 1.1 NA of DO.

In AO-LLSM, we mount cylindrical embryos such as zebrafish and *C. elegans* such that their long axes are aligned perpendicular to the plane of EO and DO, and generally try to limit our imaging to the upper half of the cylinder (e.g., Fig. 4). Given that the light sheet is at an angle of  $32^\circ$  relative to the plane of the cover slip, the incident angle relative to the specimen surface then covers the range  $-32^\circ \leq \theta_1 \leq 58^\circ$ , where the upper limit occurs at the top of the embryo, and the bottom limit occurs at the midline. Thus, the worst case with the largest tilt angle  $\beta$  occurs at the top of the embryo, where we find that light sheets of  $y_{FOV} = 15, 25, \text{ or } 50$   $\mu\text{m}$  will remain in focus for specimen refractive indexes of  $n_2 \leq 1.389, 1.365, \text{ and } 1.349$ , respectively. However, for many applications it is not necessary to image at the top of the embryo, and we can restrict the incident angle to the range  $|\theta_1| \leq 32^\circ$  or less. In this case, light sheets of  $y_{FOV} = 15, 25, \text{ or } 50$   $\mu\text{m}$  will remain in focus for specimen refractive indexes of  $n_2 \leq 1.480, 1.418, \text{ and } 1.374$ , respectively.

Accurate measurements of the mean refractive index of different biological specimens is hard to come by, but one such measurement yielded  $n_2 = 1.382 \pm 0.004$  for bovine muscle tissue (46). Using this as a likely upper bound for  $n_2$  in zebrafish, the above estimates suggest that a lattice light sheet will remain in focus over a field of view of at least 50  $\mu\text{m}$  if it intersects the fish anywhere from the midline up to  $64^\circ$  from the midline. Since this is comparable to the maximum isoplanatic patch size we see in zebrafish, beyond which we need to tile anyway to cover larger fields of view, it suggests that active correction of the light sheet tilt angle is not necessary. Furthermore, even at the top of the embryo, where the tilt angle is the largest, we estimate that a 25  $\mu\text{m}$  field of view should still remain in focus.

These estimates are consistent with or even conservative compared to our experimental observations in zebrafish, suggesting a refractive index of somewhat less than 1.38 in the fish. Thus, although we included sample-conjugate galvanometer G5 in our microscope design (fig. S1) in order to actively correct the sample-induced pitch of the light sheet, in practice we did not find its use necessary.

Of course, these results assume that the center of the field of view has been corrected to place it coincident with the focal plane of DO, and hence we also need to find the extent to which such correction is necessary. Assuming  $n_1 = 1.34$  and  $n_2 = 1.375$ , Eq (16) predicts that the light sheet will be axially displaced by  $\Delta z = 0.45, 0.93, 1.46, 2.12, 2.98, 3.95,$  and  $23.0 \mu\text{m}$  for incident angles of  $\theta_1 = 10, 20, 30, 40, 50, 58,$  and  $90^\circ$ , respectively, for every  $100 \mu\text{m}$  of penetration within the specimen. Given that we routinely image at depths of  $100\text{-}200 \mu\text{m}$ , autofocus is therefore essential. Furthermore, given that the incident angle can change significantly with axial position of the incident light sheet near the top of a cylindrical embryo, the amount of focal displacement of the light sheet within the specimen can change significantly even over a single tiled region, requiring multiple rounds of autofocus correction to maintain alignment with the detection focal plane.

It is also worth noting from the above estimates that, when using conventional Gaussian light sheets to cover fields of view of hundreds of microns or more, both autofocus *and* adaptive correction of the pitch angle  $\beta$  is essential. This is particularly true in the case of *in toto* imaging where, in the absence of sample rotation, the light sheet is tangent ( $\theta_1 = 90^\circ$ ) to the specimen surface at some point, and  $\beta$  is its largest there. A light sheet microscope that adaptively corrects for both light sheet tilt and axial displacement errors has been introduced (12), although it does not include adaptive optics to correct for other sample-induced aberrations.

Another recent innovation of note is the addition of non-toxic Iodixanol to tune the refractive index  $n_1$  to match the mean index  $n_2$  of the specimen (47). This should greatly reduce the deflection of the light sheet at the media-specimen interface, possibly eliminating the need for tilt correction even over large fields of view. However, adaptive optics and autofocus correction are likely still required to compensate for defocus and higher order aberrations due to the refractive index inhomogeneity of the specimen itself.

## 5. AO correction and autofocus sequence

Excitation correction, detection correction, and autofocus occur on a tile-by tile basis. The first tile at the first time point is AO corrected starting from system corrected patterns on SLM and DM. However, subsequent tiles are visited in a serpentine pattern. Therefore, for the first time point, we start with the corrective patterns from the previous adjacent tile when measuring the corrections needed for the next tile. For all later time points, for any tile we start with the corrective patterns we determined at the last time point for that tile and then measure the changes to these patterns needed for the current time point. Since AO correction of excitation or detection aberrations can shift the position of the light sheet or detection focal plane, these corrections are

performed first at each tile, as described in supplementary notes 3 and 2 above, before executing the autofocus sequence.

For the autofocus sequence itself, we need to perform an initial calibration for axial chromatic aberration in the detection path, once the microscope is assembled and system aberration corrections are applied to SLM and DM. Since DO is color corrected across the visible spectrum, the focal offset between different fluorescence emission wavelengths is negligible, but the offset between these wavelengths and the infrared two-photon excitation (TPE) wavelengths can be substantial. Thus, for each TPE wavelength  $\lambda_{TPE}$  we might use, we image a 100 nm fluorescent bead which can be excited at that wavelength, and use it to record a 3D PSF by scanning the TPE spot laterally with galvos G1 and G6, and axially by translating DO with a piezo (Physik Instrumente, P-726.1CD). We then calculate the axial centroid of the PSF, and note the piezo voltage  $V_{z_{TPE}}(\lambda_{TPE})$  to which it corresponds. Next, we illuminate the same bead with visible excitation through EO, and record a 3D widefield PSF by axially scanning the DO piezo and imaging each plane at CAM1. We then calculate the axial centroid of this PSF, and note its corresponding piezo voltage  $V_{z_{VIS}}$ . The difference:

$$\Delta V_{z_{TPE}}^{VIS}(\lambda_{TPE}) = V_{z_{VIS}} - V_{z_{TPE}}(\lambda_{TPE}) \quad (21)$$

gives the offset voltage needed to move from the plane of the scanning TPE guide star to the focal plane of DO at visible wavelengths.

After this initial calibration, we choose one of two different paths to autofocus correction depending on whether the distribution of fluorescence within the current tile is sparse or dense. If it is sparse, so that it is likely that there is only a single bright feature within the current tile, we first use the DO piezo to position the visible light focal plane of DO at the axial center of the tile and then sweep z galvo G4 (fig. S1) to axially scan the light sheet through the tile while recording the fluorescence signal on CAM1 at every plane. After identifying the brightest plane, we park G4 to position the light sheet at this plane, and park DO such that its visible focal plane would be coincident with the light sheet plane if the sample were not present. Of course, with the sample present, the light sheet might be axially displaced as described in supplementary note 4, or the detection focal plane might be displaced by sample-induced defocus aberration. Therefore, to restore the coincidence of these planes, we first collect the fluorescence generated by the lattice light sheet back through EO, and record a side-on image of the light sheet at CAM4. We then turn off the light sheet excitation, turn on the TPE excitation, scan across the TPE focal plane of DO at the chosen excitation wavelength  $\lambda_{TPE}$ , collect with EO the fluorescence thereby generated, and record a side-on image of the TPE excitation plane at CAM4. We then fit curves to the side-

on profiles of the light sheet and TPE excitation plane to find their centers to sub-pixel precision. The axial distance  $\Delta z_{LS}^{TPE}(\lambda_{TPE})$  between these planes determines the corrective voltage  $\Delta V z_{LS}^{TPE}(\lambda_{TPE})$  that must be applied to G4 to bring them into alignment. However, we wish to align the light sheet with the visible focal plane, not the TPE focal plane, so we must also add the calibration offset voltage  $\Delta V z_{TPE}^{VIS}(\lambda_{TPE})$  from Eq (21) to G4 as well:

$$\Delta V z_{LS}^{VIS}(\lambda_{TPE}) = \Delta V z_{LS}^{TPE}(\lambda_{TPE}) + \Delta V z_{TPE}^{VIS}(\lambda_{TPE}) \quad (22)$$

This then brings the light sheet into alignment with the visible focal plane of DO, completing the autofocus procedure for the current tile.

If the fluorescence is densely distributed, we repeat this process across a series (usually five) of planes  $z = z_1 \dots z_N$  equally spaced within the tile to determine the offset voltages  $\Delta V z_{LS}^{VIS}(\lambda_{TPE}, z_n)$  at G4 required to keep the light sheet at the visible focal plane of DO. We then fit a second order polynomial to this data, weighted by the peak TPE fluorescence signal recorded at CAM4 at each plane, to yield a continuous curve of the voltage offset vs axial position  $\Delta V z_{LS}^{VIS}(\lambda_{TPE}, z)$  required to maintain focus anywhere within the tile. In subsequent imaging, this offset curve is added to the linear voltage ramp normally applied to G4 when scanning the light sheet axially through the tile.

As demonstrated in supplementary note 4, using a z-dependent calibration curve to maintain autofocus within the specimen throughout a given tile rather than using a single offset voltage is essential in regions of rapidly changing specimen curvature, where the axial displacement  $\Delta z_{focus}$  and pitch angle  $\beta$  of the light sheet change quickly even within a single isoplanatic volume. However, given that the procedure involves scanning the TPE focus laterally at several axial focal planes within the tile, which is the same procedure used to measure the sample-induced aberration in the detection path, at no additional cost of time or photobleaching we can simultaneously collect the TPE emission with DO as well as EO, and thus perform a second round of detection AO correction while the autofocus measurement is in progress. This allows us to correct any residual aberrations remaining after the first corrective round within the tile, or to compensate for any creep in the position of DM after the initial correction is applied.

## 6. Sample Preparation and Imaging Conditions

### a. Ethics statements

Zebrafish were housed at 28.5°C using standard protocols (48). The zebrafish work was authorized by the Harvard Medical Area Standing Committee on Animals under protocol number 04487, the Janelia Research Campus IACUC under protocol number 13-104. The generation of teratoma in mice was approved by the ACUC of University of California, Berkeley.

### b. Zebrafish

#### b.1 Zebrafish lines used in this study

Adult zebrafish, 3 months to 2 years of age, were mated to produce embryos and larvae using the AB wild-type strain and the following transgenic lines: *Tg(actb2:mem-citrine-citrine)<sup>hm30</sup>*, *Tg(actb2:mem-citrine)/(actb2:Hsa.H2b-tdTomato)<sup>hm32</sup>*, *Tg(actb2:mem-citrine)/(actb2:Hsa.H2b-tdTomato)<sup>hm33</sup>* (although *actb2:Hsa.H2b-tdTomato* of these divergent constructs in transgenic fish tends to be silenced), *Tg(actb2:mem-mCherry2)<sup>hm29</sup>* and *Tg(actb2:mem-mCardinal)<sup>hm61</sup>* generated at Harvard Medical School (18, 49, 50); *mem* corresponds to 2 copies of the sequence containing the palmitoylation and myristoylation motifs of the lyn kinase that targets fused fluorescent proteins to the plasma membrane. *Tg(Xl.eef1a1:clta-dsRed monomer)* was provided by Steffen Scholpp (13, 50). *Tg(elavl3:TetA-EcR-2a-mCherry)* that expresses dually inducible Tet-On activator (TetA-EcR) (51) and mCherry under the promoter of *elavl3* (52), an early marker for neuronal differentiation (53), was generated using Tol2 transgenesis (54).

#### b.2 Zebrafish reagents

Plasmids encoding *Dr.clta-3xGSS-mNeonGreen*, *tagRFPT-3xGSS-Dr.sec61*, *Dr.b4galt1(1-60)-3xGSS-mNeonGreen*, and *Dr.cox8a(1-34)-3xGSS-mCardinal* (see annotated sequences under supplementary note 7) were generated as follows: a zebrafish cDNA library was made by first extracting RNA from 24 hpf embryos using Trizol (Thermo Fisher Scientific, Waltham, MA), then cleaning the RNA using the RNeasy mini-kit (Qiagen, Hilden, Germany), followed by conversion of mRNA to cDNA using SuperScript First-Strand Synthesis System (Thermo Fisher Scientific). Open reading frames were cloned from the cDNA library into the pMTB plasmid backbone downstream of the *actb2* and *sp6* promoters using isothermal assembly strategies (55). mRNAs were synthesized from linearized plasmid using the mMessage mMachine SP6 Transcription kit (Thermo Fisher Scientific) and purified before injection into the zebrafish embryos using RNaseasy Mini Kit (Qiagen).

A plasmid was built to express Autobow (31) under control of the under tetracycline responsive element (TRE) TRE:Autobow.

Plasmids encoding mCherry-CAAX and mApple-Lifeact were obtained from the Michael Davidson Fluorescent Protein Collection (<https://www.addgene.org/fluorescent-proteins/davidson/>) and stably transfected within MDA-MB-231 cells.

### *b.3 Zebrafish embryo treatments*

*Labeling of organelles.* A mixture containing 23 pg of mRNA for each organelle marker was injected into the 1 cell-stage embryos from crosses of *Tg(actb2:mem-mCardinal)<sup>hm36</sup>* parents. Mitochondria were labeled by incubating the embryos in 1  $\mu$ M MitoTracker Deep Red (Thermo Fisher Scientific) from 4 hpf until 14 hpf followed by five consecutive washes with Danieau buffer prior to imaging. This resulted in mosaic labeling of cells because the dye did not reach deeper cells. General labeling of all intracellular membranes was achieved by first incubating embryos with 50  $\mu$ M BODIPY TR methyl ester dye (Thermo Fisher Scientific) for 1 hr and then rinsing five times with Danieau buffer prior to imaging. Fluid phase uptake into endosomes by cells exposed to the blood circulation was visualized by injecting ~10 ng of 3 kDa dextran-Texas red neutral (Thermo Fisher Scientific) into the zebrafish heart at 60 hpf.

*Zebrafish xenografts.* MDA-MB-231 human breast cancer cells (ATCC) stably expressing mCherry-CAAX or mApple-lifeact were suspended using Nunc UpCell dishes (ThermoFisher). Approximately 50-100 cells were injected into the common cardinal vein of 48 hpf *kdrl:gfp* transgenic zebrafish embryos using a CellTram Vario (Eppendorf) (56). Host embryos were maintained at 33°C, and those containing injected cells in the tail vasculature were identified under a fluorescent dissecting microscope.

*Brainbow labeling of newly differentiated neurons.* TRE:Autobow was injected into *Tg[elavl3:TetA-EcR-2a-mCherry]* at the one cell stage at the concentration of 25 ng/ $\mu$ l. Injected embryos were dechorionated at 48 hpf and bathed in E3 medium containing Tebufenozide (50  $\mu$ M) and Doxycycline (50  $\mu$ g/ml) for 4 hours. This protocol labeled immature neurons with growing axons in the spinal cord in stochastic combinations of Cerulean, PhiYFP and mKate2.

### *c. Gene-edited intestinal epithelial organoids*

*Cell culture.* hESCs (WIBR3, NIH stem cell registration #0079) were cultured as described (57, 58). Briefly, hESCs were maintained on a layer of inactivated mouse embryonic fibroblast (MEFs) in hESC medium (DMEM/F12 (Lifetechnologies)) supplemented with 20% KnockOut™ Serum Replacement (Gibco™ 10828028), 1 mM glutamine (Gibco™ 25030-081), 1% non-essential

amino acids (Gibco™ 11140076), 0.1 mM  $\beta$ -mercaptoethanol (Sigma-Aldrich M6250), 1000 U/ml penicillin/streptomycin (Gibco™15140122), and 4 ng/ml FGF-Basic full (Invitrogen [PHG0263](#)). Cultures were passaged every 7 days with 1.5 mg/ml collagenase type IV (Gibco™ 17104019) and gravitational sedimentation by washing 3 times in wash media (DMEM/F12 (Gibco™ 11320-033) supplemented with 5% fetal bovine serum (Gibco™ [10437028](#)) and 1000 U/ml penicillin/streptomycin (Gibco™15140122).

*Gene editing.* The clathrin light chain *CLTA* gene was targeted into hESCs as previously described using a paired ZFN that targets exon 7 (59). Cas9 and sgRNAs were expressed using the pX330 plasmid (Addgene plasmid # 42230). The *DNM2* gene was targeted in exon 22 with cctgctcgactaggcctcga as sgRNA target site.  $1-2 \times 10^7$  hESCs were electroporated with 5  $\mu$ g of each ZFN (or 10  $\mu$ g of pX330 Cas9 plasmid) and 40  $\mu$ g of repair donor plasmid. Cells were sorted for expression of GFP and/or TagRFP fluorescence 72h after electroporation. Clonal populations were isolated and characterized as described (60).

*Generation of intestinal epithelial organoids.* Intestinal organoids were derived for genome-engineered hESCs as described previously (61). Briefly, genome-engineered hESCs were collected by collagenase treatment (1.5 mg/mL) and separated from feeder cells by sedimentation. Cells were resuspended in 250  $\mu$ L of PBS and injected subcutaneously into NOD- SCID mice (Taconic). Teratomas (<2 cm) formed within 6–8 weeks when they were isolated and disaggregated into a single cell suspension using trypsin digestion and mechanical dissociation with scalpels. Next, cells were strained through a 45  $\mu$ m mesh and approximately  $5 \times 10^4$  cells embedded in 50  $\mu$ L Matrigel (Corning® [354234](#)) in a well of a 24 well plate. Cells were incubated at 37 °C for 15 min and after the Matrigel solidified, growth media (see below) was added to the well. Organoids formed over the period of a week before cultures were passaged by 30 min dissociation in Dispase (5 U/mL Stemcell Technologies™) and gravity sedimentation of newly forming organoids (3X 2 min at 40G in 12.5 mL of DMEF12 (Gibco™ 11320-033) with 0.5% BSA (Sigma, A4503). Single cells were aspirated with the supernatant of each wash to mechanically enrich for the faster-sedimenting organoids. This procedure combined with the biological attrition of other cell types resulted in almost homogenous organoid cultures after three passages over three one week intervals. Subsequent passages were done by mechanical shearing with a P1000 pipette after 5 min exposure to 2mM EDTA 0.5%BSA in PBS.

*Organoid culture medium.* Organoids were cultured using conditioned medium produces are previously described (62). Low passage L-WRN cells (producing Wnt-3A, R-spondin 3, and noggin were cultured as described previously (62) in DMEM with high glucose (Sigma, D6429) supplemented with 10% FBS, 50 mg/ml G418 (Gibco™ 11965-092), 100 mg/ml hygromycin (Millipore Sigma 400050) to confluence and passaged 1:4. When confluent again, 20 ml new

media per 150 cm<sup>2</sup> flask comprising Advanced DMEM/F12 (Gibco 12634010), 200 mM L-glutamine (Gibco™ 25030-081), 10,000 units/ml penicillin and 10 mg/ml streptomycin (Gibco™15140122) and 0.5% BSA (Sigma, A4503) was added and collected each day for 4 days and stored at 4°C before filtration and freezing. This conditioned base media was supplemented 1:1 with a volume of unconditioned base media comprising Advanced DMEM/F-12 (Gibco™ 12634010), N2 (Gibco™ 17502-048), B27(Gibco™ 12587-010), L-glutamine (Gibco™ 25030-081), 10,000 units/ml penicillin and 10 mg/ml streptomycin (Gibco™15140122), nonessential amino acids (Gibco™ 11140076), 10,000 units/ml penicillin/ streptomycin (Sigma, P4333) and stored in frozen aliquots. Immediately before use the media was supplemented with EGF (50 ng/mL)(R&D Systems 236-EG-01M) and added into the well containing Matrigel (Corning 47743-716) embedded organoids. Media, stored no longer than 2 weeks at 4°C, was replaced every two days. Two days before imaging, organoids were released by Dispase (5 U/mL Stemcell Technologies digestion and resuspended in 10-20µL Matrigel without phenol-red (Corning® 47743-716), placed at 4°C on a 5 mm diameter cover slip (Warner Instruments, 64-0700) and incubated at 37°C before adding medium. Medium was replaced with DMEM/F12 without phenol red (Gibco™21041025) with 10mM HEPES (Gibco™ 15630080) for imaging.

*d. Isolated gene-edited human breast epithelial cells.*

*Culture conditions.* Gene-edited SUM159 cells expressing AP2-EGFP in both alleles (18) were grown in SUM-media made of DMEM/F-12/GlutaMAX (10565-042; Thermo Fisher Scientific, Waltham, MA) supplemented with 5% fetal bovine serum (FBS; S11150; Atlanta Biologicals, Flowery Branch, GA), 100 U/ml penicillin and streptomycin (45000-652; VWR International, Radnor, PA), 1 µg/ml hydrocortisone (H4001; Sigma-Aldrich, St. Louis, MO), 5 µg/ml insulin (I9278; Sigma-Aldrich), and 10 mM 4-(2-hydroxyethyl)- 1-piperazineethanesulfonic acid (HEPES; 25-060-CI; Mediatech, Manassas, VA), pH 7.4. Four hours before imaging, the cells were plated at ~ 50% confluency on 5mm diameter glass coverslips pre-cleaned by the NaOH treatment procedure described above. The coverslips were then cover with 50 uL Matrigel diluted 1:10 with Leibovitz's L-15 medium without phenol red (21083-027; Life Technologies) and incubated for 10 min at 37°C before mounting them on the sample holder. The sample holder was then immersed in ~8 ml of Leibovitz's L-15 medium without phenol red supplemented with 5% FBS and 20mM HEPES, pH 7.4 and imaged at 37°C.

e. *C. elegans*

Rearing and handling of *C. elegans* was done using standard culture conditions at 25°C as previously described (63). Synchronized larvae were generated using hypochlorite treatment of gravid adults, and grown at 25°C to the L3 stage. The AC and basement membrane were visualized in a strain containing the following allele and transgenes, *qyIs227[cdh-3>mCherry::moeABD]*; *LGX qyIs7[laminin::GFP]*. L3 stage animals were anesthetized for 30 minutes as described previously (64) using 0.2% (E10621; Sigma-Aldrich, St. Louis, MO) and 0.02% levamisole (L9756; Sigma-Aldrich, St. Louis, MO) in M9 buffer in a staining dish. A mounting solution of 1% low melt agarose (0815; VWR International, Radnor, PA) in M9 with the same concentration of anesthetics was prepared and cooled to 37C in a water bath. A sample holder was coated in a thin layer of mounting solution and cooled to 4C. This process was repeated a second time. L3 stage *C. elegans* larvae were then transferred by mouth pipette to the sample holder, and excess anesthetic solution was removed. While larvae were held in place with a hair pick, mounting solution was added on top of the larvae. The sample holder was cooled to 4C for 90 seconds to ensure rapid gelling of the mounting solution. Imaging was performed in M9 which also contained the same concentration of anesthetics.

f. *Arabidopsis*

*Arabidopsis p35S::GFP-MBD* seeds described previously (65) were vapor-sterilized in an air-tight container with 4% hydrochloric acid in bleach, vernalized in the dark at 4°C for 3 days, and grown under constant light at 20°C on 0.8% agar at pH5.7, supplemented with 0.32% Gamborg's B-5 basal medium (G5893; Sigma-Aldrich). Epidermal cells of cotyledons were imaged 3 days after germination.

## 7. DNA Sequences for the Zebrafish constructs used to label intracellular markers

a. *tagRFPr* *3xGGS linker* *Dr.sec61* (endoplasmic reticulum and nuclear envelope)

```
ATGGTGTCTAAGGGCGAAGAGCTGATTAAGGAGAACATGCACATGAAGCTATACAT
GGAGGGCACCGTGAACAACCACCACTTCAAGTGCACATCCGAGGGCGAAGGCAAGC
CCTACGAGGGCACCCAGACCATGAGAATCAAGGTGGTTCGAGGGCGGCCCTCTCCCC
TTCGCCTTCGACATCCTGGCTACCAGCTTCATGTACGGCAGCAGAACCTTCATCAAC
CACACCCAGGGCATCCCCGATTTCTTTAAGCAGTCCTTCCCTGAGGGCTTCACATGG
GAGAGAGTCACCACATACGAAGACGGGGGCGTGCTGACCGCTACCCAGGACACCAG
```

CCTCCAGGACGGCTGCCTCATCTACAACGTCAAGATCAGAGGGGTGAACTTCCCATC  
 CAACGGCCCTGTGATGCAGAAGAAAACACTCGGCTGGGAGGCCAACACCGAGATGC  
 TGTACCCCGCTGACGGCGGCCTGGAAGGCAGAACCGACATGGCCCTGAAGCTCGTG  
 GGCGGGGGCCACCTGATCTGCAACTTCAAGACCACATACAGATCCAAGAAACCCGC  
 TAAGAACCTCAAGATGCCCCGGCGTCTACTATGTGGACCACAGACTGGAAAGAATCA  
 AGGAGGCCGACAAAGAGACCTACGTTCGAGCAGCACGAGGTGGCTGTGGCCAGATA  
 CTGCGACCTCCCTAGCAAACCTGGGGCACAACTTAATGGCATGGACGAGCTGTACA  
 AGGGCGGATCCGGTGGATCCGGTGGATCTATGCCTGGACCCGCAGCTAGTGCAACA  
 AATGTTGGTGCCTCCAGCCGTTCCCCCAGTAAGACGGTGGCTCCCCGCACTGCTGGT  
 ACCTCAGCCAGACAAAGGAAAGCCACAAGCAGCAGTGCACGCAGCGGAGGCAGAT  
 CCACAGCTTCTGCAGGCACAGGAGGAATGTGGCGCTTTTACACTGAAGATTCACCAG  
 GGCTTAAAGTTGGCCAGTTCAGTTTTGGTGATGAGTCTGCTGTTTATCGCATCTGT  
 CTTTCATGCTGCACATCTGGGGAAAGTACACCCGCTCCTAA

b. *Dr.cltA* 3xGGS linker mNeonGreen (clathrin light chain A)

ATGGACGATTTTCGATATGCTCAGTGCCCCTCAAGGAAGCGCAGGGAACGGTGTCCG  
 GGCAGACGAGGACCCGGCGGCATTCTGGCCAGCAAGAGAGCGAGATCGCTG  
 GCATCGAGAATGACGAGGGCTTCAGCATCCTGGACAGCGGAGATGTGCCTTCGTCC  
 CTGAGCCAAGACCAGGACGGTGGAGCAATGAATGGAGATCTGCATGGGGAGAGTA  
 ATGGCCCTTCAGATGTGTACGCGGCCATCTCCAGTGTGGATCCGGTTCAGGCTGAGC  
 CGGAGAGCTTGAGGAAGTGGAGAGAGGAGCAGCGAGATAGGCTGGAGGAGCTCGA  
 TGCGAACTCGCGTAAACAGGAGGCCGAGTGGAAAGAGAAGGCAAAGCTGGAGCTG  
 GAGGAATGGCACACCAGGCAGAACGAGCAGCTGGAGAAAACCAAAGTCAACAACA  
 GGGTGTGGATGAGGATTTCTACAACAACCCTTCGCTGATCTGATTGGTTATGTCA  
 CTCACATTAACCATCCTTGCTACCGCCTAGACCAGGCGGCTGAGGAAGCCATGGTGT  
 CGGAGCTGGATGAAAACAGTCTGGCACAGAATGGGAACGTGTGGCGCGTCTTTGC  
 GATTTCAACCCTAAATCCAGCAAGCAGGCAAAGGATGTGTCCCAGCATGCGTTCAGTG  
 CTCATCTCTTAAACAGGCTCCGCTCGTCCGCGGGCGGATCCGGTGGATCCGGTGGAT  
 TCTATGGCAAGCAAGGGCGAGGAGGACAATATGGCCTCTCTGCCCACAACACACGA  
 GCTGCATATTTTCGGAAGCATCAACGGCGTGGATTTTCGATATGGTTGGGCAAGGAAC  
 TGAAACCCAAATGACGGATACGAGGAACTGAATCTGAAGTCAACCAAAGGCGACC  
 TCCAATTCTCACCTTGATTCTCGTTCCCATATTGGCTATGGATTTTCATCAATATCT  
 GCCATATCCTGATGGAATGTCACCATTTCAAGCCGCTATGGTGGATGGATCTGGCTA  
 CCAAGTCCACCGCACCATGCAATTTGAGGACGGCGCCTCCCTGACTGTGAACTACCG  
 CTATACCTACGAGGGATTCATATCAAGGGCGAAGCACAAGTTAAAGGAACAGGAT

TCCCAGCTGACGGCCCCGTCATGACAACTCTCTGACCGCCGCCGACTGGAGCCGGT  
 CCAAGAAAACCTACCCTAACGATAAGACCATCATCTCTACCTTCAAATGGAGTTATA  
 CCACCGGCAACGGAAAGCGCTACAGAAGCACAGCCCGAACCTATACTTTTGCT  
 AAGCCTATGGCTGCAAACCTATCTGAAAAATCAGCCTATGTATGTCTTCCGAAAACC  
 GAATTGAAGCACTCCAAAACAGAACTGAATTTCAAGGAGTGGCAGAAGGCTTTTAC  
 CGATGTTATGGGCATGGACGAGCTGTACAAATAA

c. *Dr.b4galt1(1-60)* 3xGGS linker mNeonGreen (*trans-Golgi apparatus*)

ATGTCGGAGTCGGTGGGATTCTTCACTAAAGCATGCGTCGTGCTCGTGCTGCTCTGC  
 GGGCTTCACCTCATCGTGGCACTGATTTTCTATTTATCAGAGTCGCCTTTAGCTAAAT  
 TTAGGAATTATCGACACATTTCAATTTATCTCTGATATGGTTAATTCACAAACTCACGG  
 AGAATTGGCGGATCCGGTGGATCCGGTGGATCTATGGCAAGCAAGGGCGAGGAGG  
 ACAATATGGCCTCTCTGCCCACACACGAGCTGCATATTTTCGGAAGCATCAACG  
 GCGTGGATTTTCGATATGGTTGGCAAGGAAGTGGAAACCCAAATGACGGATACGAG  
 GAACTGAATCTGAAGTCAACCAAAGGCGACCTCCAATTCTCACCTTGGATTCTCGTT  
 CCCCATATTGGCTATGGATTTCATCAATATCTGCCATATCCTGATGGAATGTCACCAT  
 TTCAAGCCGCTATGGTGGATGGATCTGGCTACCAAGTCCACCGCACCATGCAATTG  
 AGGACGGCGCCTCCCTGACTGTGAACTACCGCTATACCTACGAGGGATCTCATATCA  
 AGGGCGAAGCACAAGTTAAAGGAACAGGATTCCCAGCTGACGGCCCCGTCATGACA  
 AACTCTCTGACCGCCGCCGACTGGAGCCGGTCCAAGAAAACCTACCCTAACGATAA  
 GACCATCATCTCTACCTTCAAATGGAGTTATACCACCGGCAACGGAAAGCGCTACA  
 GAAGCACAGCCCGAACCTATACTTTTGCTAAGCCTATGGCTGCAAACCTATCTGA  
 AAAATCAGCCTATGTATGTCTTCCGAAAACCGAATTGAAGCACTCCAAAACAGAA  
 CTGAATTTCAAGGAGTGGCAGAAGGCTTTTACCGATGTTATGGGCATGGACGAGCTG  
 TACAAATAA

d. *Dr.cox8a(1-34)* 3xGGS linker mCardinal (*mitochondria*)

ATGTCTGGACTTCTGAGGGGACTAGCTCGCGTCCGCGCCGCTCCGGTTCTGCGGGGA  
 TCCACGATACCCAGCGAGCCAACCTCGTTACGCGACCCGCGAAGGGCGGATCCGG  
 TGGATCCGGTGGATCTATGGTGAGCAAGGGCGAGGAGCTGATCAAGGAGAACATGC  
 ACATGAAGCTGTACATGGAAGGCACCGTGAACAACCACCACTTCAAGTGCACCACC  
 GAAGGGGAGGGCAAGCCCTACGAGGGCACCCAGACCCAGAGGATTAAGGTGGTGG  
 AGGGAGGCCCCCTGCCGTTTCGATTCGACATCCTGGCCACCTGCTTTATGTACGGGA

GCAAGACCTTCATCAACCACACCCAGGGCATCCCCGATTTCTTTAAGCAGTCCTTCC  
 CTGAGGGCTTCACATGGGAGAGAGTCACCACATACGAAGACGGGGGCGTGCTTACC  
 GTTACCCAGGACACCAGCCTCCAGGACGGCTGCTTGATCTACAACGTCAAGCTCAG  
 AGGGGTGAACTTCCCATCCAACGGCCCTGTGATGCAGAAGAAAACACTCGGCTGGG  
 AGGCCACCACCGAGACCCTGTACCCCGCTGACGGCGGCCTGGAAGGCAGATGCGAC  
 ATGGCCCTGAAGCTCGTGGGCGGGGGCCACCTGCACTGCAACCTGAAGACCACATA  
 CAGATCCAAGAAACCCGCTAAGAACCTCAAGATGCCCGGCGTCTACTTTGTGGACC  
 GCAGACTGGAAAGAATCAAGGAGGCCGACAATGAGACCTACGTGAGCAGCACGA  
 GGTGGCTGTGGCCAGATACTGCGACCTCCCTAGCAAACCTGGGGCACAACTTAATG  
 GCATGGACGAGCTGTACAAGTAA

e. *Tg(actb2:mem-mCardinal)<sup>hm36</sup>* (*Mm.2x-lyn(1-16)*; *linker*; *mCardinal*)

ATGGGCTGCATCAAGAGCAAGCGCAAGGACAACCTGAACGACGACGAGGCCGCCA  
 TGGGCTGCATCAAGAGCAAGCGCAAGGACAACCTGAACGACGACGAGGGAGCGCC  
 AGCTGGAGGTGCAGGTGCAGCAATGGTGAGCAAGGGCGAGGAGCTGATCAAGGAG  
 AACATGCACATGAAGCTGTACATGGAAGGCACCGTGAACAACCACCACTTCAAGTG  
 CACCACCGAAGGGGAGGGCAAGCCCTACGAGGGCACCCAGACCCAGAGGATTAAG  
 GTGGTGGAGGGAGGCCCTGCGTTCGCATTCGACATCCTGGCCACCTGCTTTATG  
 TACGGGAGCAAGACCTTCATCAACCACACCCAGGGCATCCCCGATTTCTTTAAGCAG  
 TCCTTCCCTGAGGGCTTCACATGGGAGAGAGTCACCACATACGAAGACGGGGGCGT  
 GCTTACCGTTACCCAGGACACCAGCCTCCAGGACGGCTGCTTGATCTACAACGTCAA  
 GCTCAGAGGGGTGAACTTCCCATCCAACGGCCCTGTGATGCAGAAGAAAACACTCG  
 GCTGGGAGGCCACCACCGAGACCCTGTACCCCGCTGACGGCGGCCTGGAAGGCAGA  
 TGCGACATGGCCCTGAAGCTCGTGGGCGGGGGCCACCTGCACTGCAACCTGAAGAC  
 CACATACAGATCCAAGAAACCCGCTAAGAACCTCAAGATGCCCGGCGTCTACTTTGT  
 GGACCGCAGACTGGAAAGAATCAAGGAGGCCGACAATGAGACCTACGTGAGCAG  
 CACGAGGTGGCTGTGGCCAGATACTGCGACCTCCCTAGCAAACCTGGGGCACAACT  
 TAATGGCATGGACGAGCTGTACAAGTAA

## 8. Image Analysis & Visualization

All data acquired using the AO-LLSM were corrected for intensity variation across the light sheet, deconvolved using an experimentally measured PSF for each emission wavelength, and

corrected for photobleaching as noted in table S1 and as described (6). Multi-tile subvolumes were stitched as indicated (table S1) using either the Grid/Collection Stitching plugin in Fiji (66), or a Gradient-Domain stitching routine (67, 68) to merge and smooth the boundaries between adjacent tiles by matching the low spatial frequency components. All processed data sets were visualized using Amira (Thermo Fisher Scientific), Imaris x64 8.4 (Oxford Instruments), or Vision4D (Arivis) for 5D volumetric rendering.

*a. Simultaneous detection of multicellular boundaries in zebrafish embryos*

The cell boundaries within different tissues of zebrafish embryos expressing plasma membrane markers were identified by segmentation using ACME (Automated Cell Morphology Extractor) (69) built using the open-source Insight Toolkit (<http://www.itk.org/>) as follows: (1) convert the 3D tiff stacks acquired by AO-LLSM into mha format, pre-processed using a medial filter ( $\sigma = 0.3$ ); the  $xy$  planes were down-sampled such that the voxels were isotropic for all subsequent processing; (2) subject the imaged volume to a planarity filter ( $\sigma = 0.4$ ) to locate the planar membrane followed by tensor voting ( $\sigma = 0.5$ , rod saliency weight  $\alpha = 0.4$ , plate saliency weight  $\beta = 0.4$ , ball saliency weight  $\gamma = 850$ ) to close the membrane gaps; (3) complete cell boundaries by applying the watershed segmentation algorithm using the salient images generated from tensor voting; (4) up-sample in  $xy$  the segmentation map in order to match the original volume dimensions. Representative examples of the correspondence between the segmentation map and raw data are shown in fig. S20. Segmentation errors were generally infrequent. When they occurred, however, it resulted in hyper-segmentation, represented by the clear fragmentation of a single cell into multiple objects. In such cases, the images were curated by manually merging the labels of the multiple objects using custom routines written in MATLAB R2017a and visualized in ITK-SNAP or Fiji (70, 71).

The code of the planarity filter and tensor voting algorithms were optimized from the published scripts in order to take advantage of high performance computing clusters with larger memory capacities ( $>7.5\text{GB}$  per core). The segmentation was carried out at the Janelia research computing cluster comprising of Intel Sandy Bridge E5-2680, Haswell E5-2698, and Broadwell E5-2683 Xeon processor nodes containing between 16-32 cores with 120-240GB memory.

*b. Segmentation of the cell nucleus based on signal exclusion*

The nucleus of cells within different tissues was identified by segmentation in zebrafish embryos whose cell boundaries were labeled by expression of *mem-citrine* and whose

endomembranes were stained with BODIPY TR methyl ester. In brief, (1) cell boundaries were segmented as described above; (2) Up-sampling in  $z$  the segmented map and the endomembrane imaged 3D volume, such that the interpolated voxels became isotropic; cells near the edge of the 3D volume (i.e., within  $10\mu\text{m}$  in  $x,y$  and  $2.5\mu\text{m}$  in  $z$ ) were excluded from further analysis; (4) generate a 3D ROI for the endomembranes of a given cell defined by the cell surface segmented mask ; (5) remove high frequency noise in the endomembrane volume within the 3D ROI by applying a 3D Gaussian filter ( $\text{sigma} = 1$ ); (6) identify the stained endomembranes using the Otsu variance-based thresholding algorithm; (7) identify the nucleus by finding the largest set of connect voxels of background value using the `bwconncomp` function in MATLAB 2016b. A typical example showing the overlay of the segmented nucleus (green) with the images for the plasma membrane (cyan) and endomembranes (orange) is shown in fig. S20.

### *c. Segmentation of the trans-Golgi apparatus*

The trans-Golgi apparatus was labeled with GalT tagged with mNeonGreen in different cells of zebrafish embryos also expressing *mem-citrine* or *mem-mCardinal*. The trans-Golgi apparatus were identified by segmentation as follows: (1) generate a 3D ROI of the cell containing the trans-Golgi signal of a given cell defined by its segmented mask; (2) remove high frequency noise in the trans-Golgi volume by applying to the 3D ROI a 3D Gaussian filter ( $\text{sigma} = 1$ ); (3) identify the trans-Golgi volume using the Otsu thresholding algorithm; (4) eliminate objects with less than 50 connected voxels using the `bwconncomp` function.

### *d. Surface area and volume of segmented objects*

The volume of segmented cells, nuclei and trans-Golgi apparatus were determined as the sum of the isotropic voxels contained within the segmented mask and then converted to cubic microns ( $\mu\text{m}^3$ ). The area of the cell boundary was calculated using `bwperim` function in MATLAB as the sum of the voxels located at the perimeter of the segmented mask and converted to squared microns ( $\mu\text{m}^2$ ).

### *e. Tracking of crawling immune cells*

Crawling immune cells were evident in 3D data sets consisting of 500-600 time points acquired for 130 minutes corresponding to the interstitial space above the endolymphatic duct and sac of zebrafish embryos expressing *mem-citrine* imaged 72-80 hpf. These cells were first identified as follows: (1) correct the 3D drift between consecutive 3D time points by first measuring the displacement in  $x,y,z$  between the first and last time point using the correct 3D drift function in

FIJI (72) followed by interpolation of the volume between consecutive time points using interp3 function in MATLAB; (2) calculate a background volume to be used for background subtraction by generating a 4D maximum intensity projection obtained from the time points not containing crawling cells; (3) eliminate high frequency noise by applying a 3D Gaussian filter ( $\sigma = 5$ ) to the 4D maximum intensity projection; (4) generate a segmented mask of the crawling cells by subtracting each 3D time point from the smoothed 4D maximum projection followed by eliminating small isolated objects with fewer than 200 connected voxels and by closing any holes in the residual signals of the crawling cells using imdilate, imerode and imfill functions in MATLAB.

The trajectories of the identified crawling cells were then determined using u-track (73) from the centroid positions of the segmented masks. The displacement and speed of each track were calculated using squareform, pdist, and diff functions in MATLAB 2016b.

*f. 3D detection of diffraction limited fluorescent spots*

Spots corresponding to diffraction limited clathrin or AP-2 containing coated pits and coated vesicles visualized in cultured cells (organoids or isolated cells embedded in matrigel or collagen) and transgenic zebrafish for *mem-mCardinal* transiently expressing clathrin light-chain A fused to mNeonGreen were automatically detected and tracked in 3D using MATLAB routines (18). The detection step fitted an anisotropic 3D Gaussian at candidate positions that had been identified as local maxima determined by the 3D Laplacian-of-Gaussian filter. In AO corrected volumes, the  $x,y$  and  $z$  sigmas used in the 3D Gaussian fitting were locked to those determined experimentally using 100 nm beads (FluoSpheres® microspheres, Thermo Fisher) for each excitation wavelength. For the comparison of AO corrected and no AO conditions, however, their  $x,y$  and  $z$  sigmas were not fixed.

*g. Trajectories and lifetimes of coated pits and vesicles and endocytic rates*

The trajectories in 3D and lifetimes of the coated pits and vesicles detected above were determined as described (18). Briefly, the events at the cell surface membrane excluded tracks starting or ending outside of the time series, merging or splitting tracks, and tracks located inside the cell volume. The tracks, color coded for their lifetimes, were visualized in Amira 6.3 (Thermo Fisher Scientific) using the Spatial Graph View module.

An estimate of the endocytic rate mediated by the clathrin dependent endocytic pathway was obtained by (1) counting the number of tracks emanating from the cell surface and lasting longer than 15 sec; (2) estimating the amount of membrane internalized by coated vesicles assuming that on average they encapsulate a 60 nm in diameter vesicle; (3) normalizing this amount by the surface area of the cell and time and expressing it as percent of cell surface internalized per unit time.

*h. Relative intracellular location of organelles in a dividing cell in the brain zebrafish embryo*

The intracellular location of mitochondria (MitoTracker Deep Red), trans-Golgi apparatus (galT-mNeonGreen) and endoplasmic reticulum (Sec61b-tagRFPT) was monitored every 45 sec for 150 min with respect to the cell surface (*mem-citrine*) of a dividing cell located in the brain of a zebrafish embryo 14 - 16 hpf. The mapping procedure was as follows: (1) determine the cell boundary as described above; (2) determine the Euclidian distance to the cell surface of each voxel within the volume of the cell accounting for the anisotropy along the z-axis due to the sample step size using a custom MATLAB function (74); (3) calculate the relative location of organelles as the average fluorescence intensity associated with a given distance from the cell surface by dividing the integrated values of the corresponding voxels by the total number of voxels; (4) express the relative location of organelles as probability and cumulative frequency distributions.

*i. Software-aided displacement*

The cell boundaries within different tissues of zebrafish embryos expressing plasma membrane markers were automatically segmented using ACME (69). Using the segmented masks, a novel software-aided displacement (SAD) approach was implemented to facilitate the visualization and inspection of the morphology and dynamics of individual cells contained within a portion of the living tissue of the zebrafish embryo. Each cell within a given 3D volume was computationally separated from the others using the following steps: (1) determine all cell boundaries as described above to detect multicellular boundaries in zebrafish embryos; (2) generate a 3D ROI for each cell using a dilated (2 voxels) segmentation mask; (3) displace the centroid position of the cell by multiplying the distance of the cell centroid to the center of the imaged 3D volume by a constant expansion factor. Thus, cells farther from the center of the 3D volume are displaced more than the cells closer to the volume center; (4) sequentially repeat step (3) with incremental expansion factors.

### *j. Wavefront Reconstruction for Visualization*

Visualized wavefronts (e.g., Fig. 4C, D, Movies 6-8) were calculated from valid Shack-Hartmann spots using a zonal wavefront reconstruction (75) in MATLAB. Invalid points in the Shack-Hartmann image are recovered by smoothly interpolating using the neighboring points via the gridfit function in MATLAB. The waveforms were then least-squares fitted with the first 55 Zernike modes. The tip, tilt, and defocus modes were set zero. Since the wavefront fit is unconstrained at the edges, the wavefront is mostly clearly plotted when just the inner 80% of the rear pupil diameter is shown. The wavefronts were rendered using Amira 6.3 at the tiled locations where the measurements and corrections took place.

## **9. Control Electronics**

Control electronics were similar to those described previously (6), with the primary changes concerning the SLM and computer. In the new configuration, synchronization is simplified because the SLM now displays fixed images and only updates when the excitation correction is changed via software command between volume scans. A Field-Programmable Gate Array card (FPGA, National Instruments, PCIe-7852R) serves as the master clock supplying camera triggers and control voltage waveforms during image acquisition. Additional PCIe slots are needed to accommodate the added cameras and DM, and thus the control computer has been upgraded to a SuperMicro 4027GR-TRT with dual Intel E5-2670 processors.

## Supplementary Figures

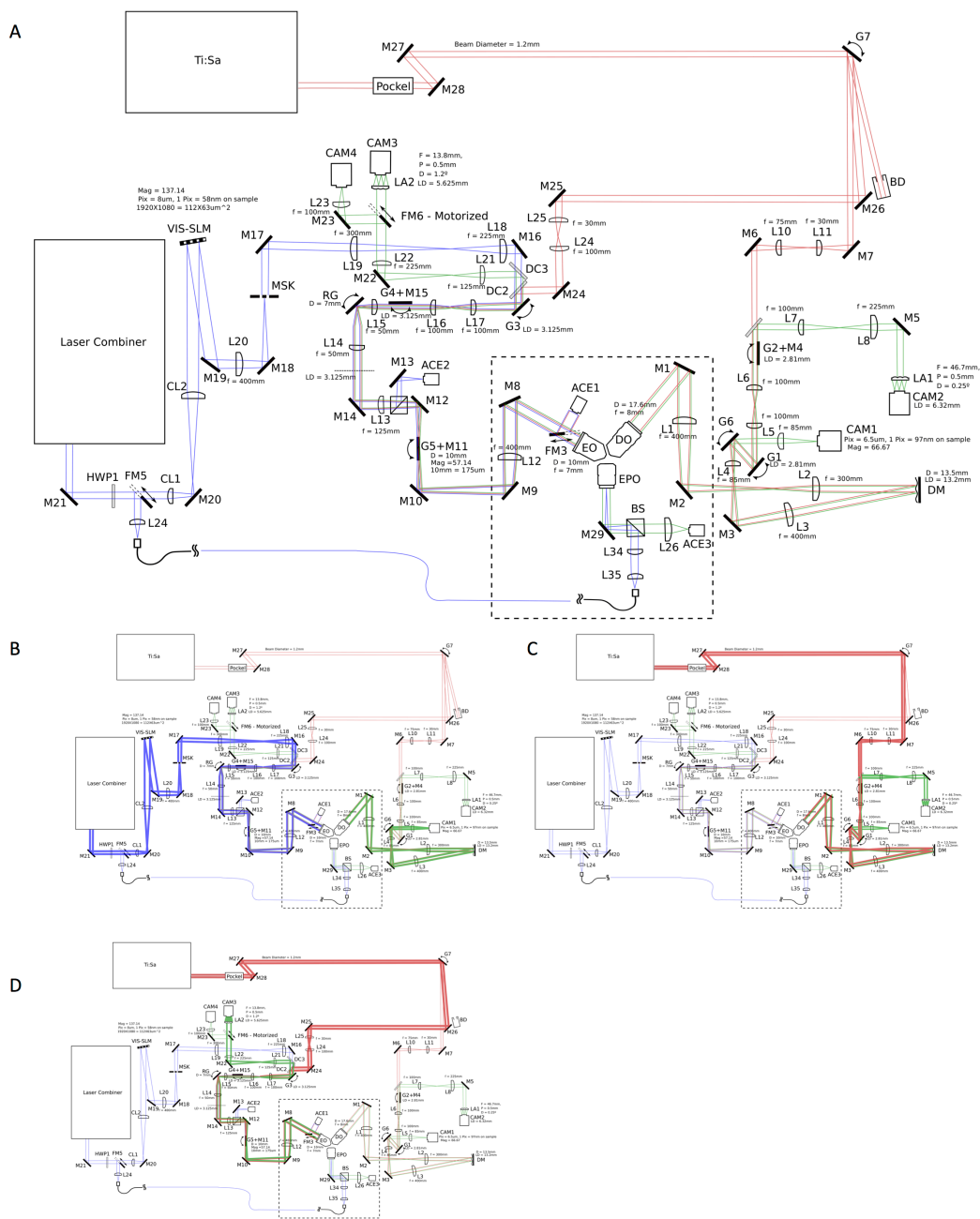


**Fig. S1. Schematic design of the adaptive optics lattice light sheet microscope. (A)** The complete microscope. **(B) *LLS path*:** Beams from the laser combiner (blue) are elongated using a pair of cylindrical lenses (CL1, CL2), which then illuminate three thin strips of spatial light

modulator VIS-SLM vertically separated by 1.5 mm. The reflected diffraction orders are filtered using annular mask MSK and conjugated to galvanometer mirrors G3, G4 to dither the light sheet along the  $x$  axis and axially scan it along the  $z$  axis at the sample plane. Resonant galvanometer RG is placed conjugate to the sample plane to wobble the light sheet in the  $xy$  plane. The light then enters the back focal plane of custom manufactured excitation objective EO, which is conjugate to MSK, G3, and G4, to generate the lattice light sheet. Fluorescence generated by the light sheet within the specimen is collected using detection objective DO and reflected off deformable mirror DM conjugate to DO before being focused onto sCMOS camera CAM1. **(C)** *Detection correction path*: An ultrafast pulsed laser beam (Ti:Saph) is directed towards the detection arm of the LLSM by galvanometer G7, expanded by lenses L10, L11, and reflected from galvanometer mirrors G1, G2 conjugate to the rear pupil of DO before reflecting from switching galvanometer G6 and DM and expanded by lens airs L3, L4 and L1, L2 to enter DO. The TPE guide star fluorescence generated at the sample was collected through DO and reflected back by galvos G1, G2, and a dichroic mirror to a Shack-Hartmann wavefront sensor consisting of microlens array LA1 focused onto EMCCD camera CAM2 (*c.f.* supplementary note 2). **(D)** *Excitation correction path*: The Ti:Saph beam is directed towards the excitation arm of the LLSM by galvo G7 and injected into the excitation light sheet path by reflecting from dichroic filter DC2. The beam is scanned by galvanometers G3, G4, each conjugate to the back pupil of the excitation objective, to generate a plane of TPE fluorescence at the sample. This was collected by the excitation objective, descanned by back reflection across G3 and G4, and directed via a dichroic filter (DC3) to a Shack-Hartmann wavefront sensor consisting of microlens array LA2 focused onto EMCCD camera CAM3 (*c.f.*, supplementary note 1).

### Abbreviations used in Fig S1:

EO: excitation objective (Special Optics, 0.65 NA water dipping)

DO: detection objective (Nikon 25x 1.1NA water dipping)

EPO: epi objective (Olympus LUMPLFLN40XW, 0.8 NA, oil immersion)

M: mirrors (Thorlabs P1 or EO2)

L: lens with labeled focal length

BD: beam dump

MSK: annular mask (Photo Sciences Inc)

CAM1: camera for lattice light sheet imaging (Hamamatsu Orca 4.0 V2)

CAM2: camera for sensing the detection wavefront (Andor iXon 3 EMCCD)

CAM3: camera for sensing the excitation wavefront (Andor iXon + EMCCD)

- CAM4: camera for imaging sample plane through EO (Hamamatsu Orca 4.0 V2, used for autofocus)
- ACE1: camera for imaging illumination at the back pupil of EO (Baselar ACE)
- ACE2: sample-conjugate camera for inspecting cross-sectional pattern of the lattice light sheet (Baselar ACE)
- ACE3: view finding camera for imaging sample through the epi objective (Baselar ACE))
- G1, G2: *xy* galvos for scanning/descanning TPE guide star through DO
- G3, G4: *xz* galvos for scanning lattice light sheet and scanning/descanning TPE guide star through EO
- G5: pitch galvo conjugated to the sample plane, to correct for light sheet pitch angle error
- G6: 10 mm galvo to select beam path between imaging (M3→G6→CAM1) and detection correction (M3→G6→G1)
- G7: 3mm galvo to switch two photon laser beam between: a beam dump (M27→G7→BD); the excitation pathway (M27→G7→M26); or the detection pathway (M27→G7→M7)
- RG: resonant galvo conjugated to the sample plane, to wobble the light sheet in the *xy* plane to minimize shadowing artifacts
- DM: deformable mirror (ALPAO 97-15)
- FM3: magnetic mirror mount, inserted when inspecting illumination pattern at rear pupil of EO using ACE1
- FM5: manual flip mirror to choose between epi illumination and light sheet illumination
- FM6: motorized flip mirror (Thorlabs MFF101) to choose between sending fluorescence emission from EO to the wavefront sensor (CAM3) or the auto-focus camera (CAM4)
- DC2: dichroic mirror, reflects NIR, transmits VIS beams (Semrock, 670 nm edge BrightLine® multiphoton short-pass dichroic beamsplitter)
- DC3: dichroic mirror, reflects fluorescence emission, transmits VIS excitation (Yokogawa dichroic beamsplitter, Di01-T405/488/561 or Di01-T442/488/561)

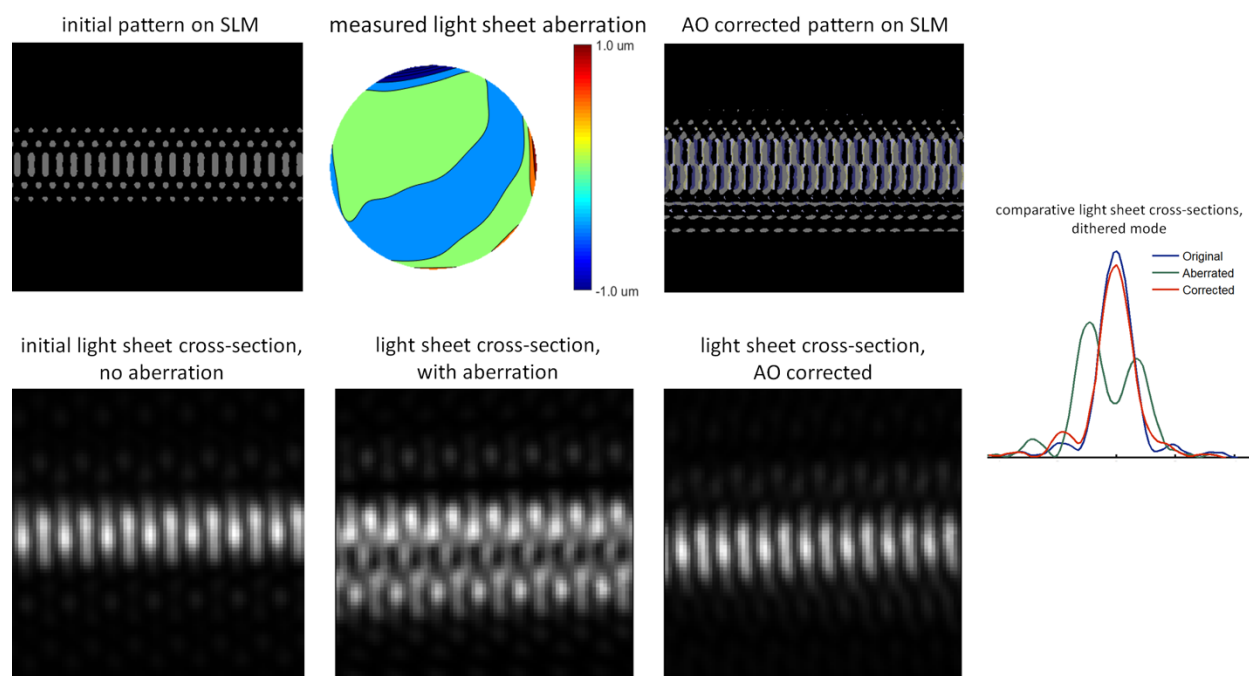


**Fig. S2. Correction of lattice light sheet excitation aberrations.** In an aberration-free setting, the initial binary phase pattern at the SLM (**top left**) generates an ideal lattice light sheet cross-section at the sample (**bottom left**). However, sample-induced aberrations (e.g., **center top**), distort the light sheet within the specimen (**center bottom**). These aberrations can be canceled by applying an appropriate corrective greyscale pattern at the SLM (**right top**), thereby recovering the desired light sheet pattern within the specimen (**right bottom**), (*c.f.* supplementary note 3).

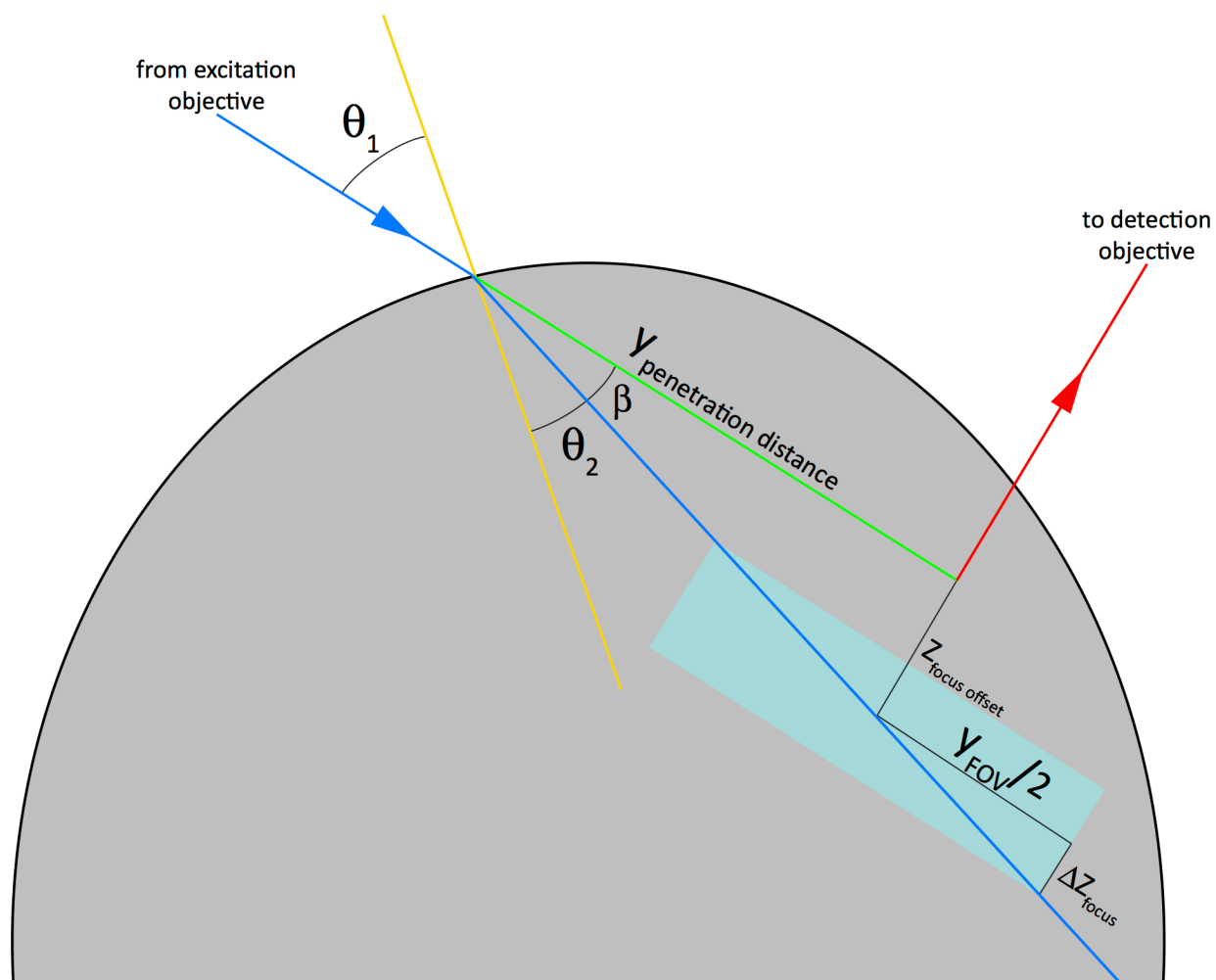


**Fig. S3. Curvature-induced pitch angle error of a lattice light sheet.** Schematic representation of the deflection  $\beta$  of a light sheet incident at an angle  $\theta_1$  at the interface between an imaging media of refractive index  $n_1$  and a specimen of refractive index  $n_2$  (*c.f.* supplementary note 4).

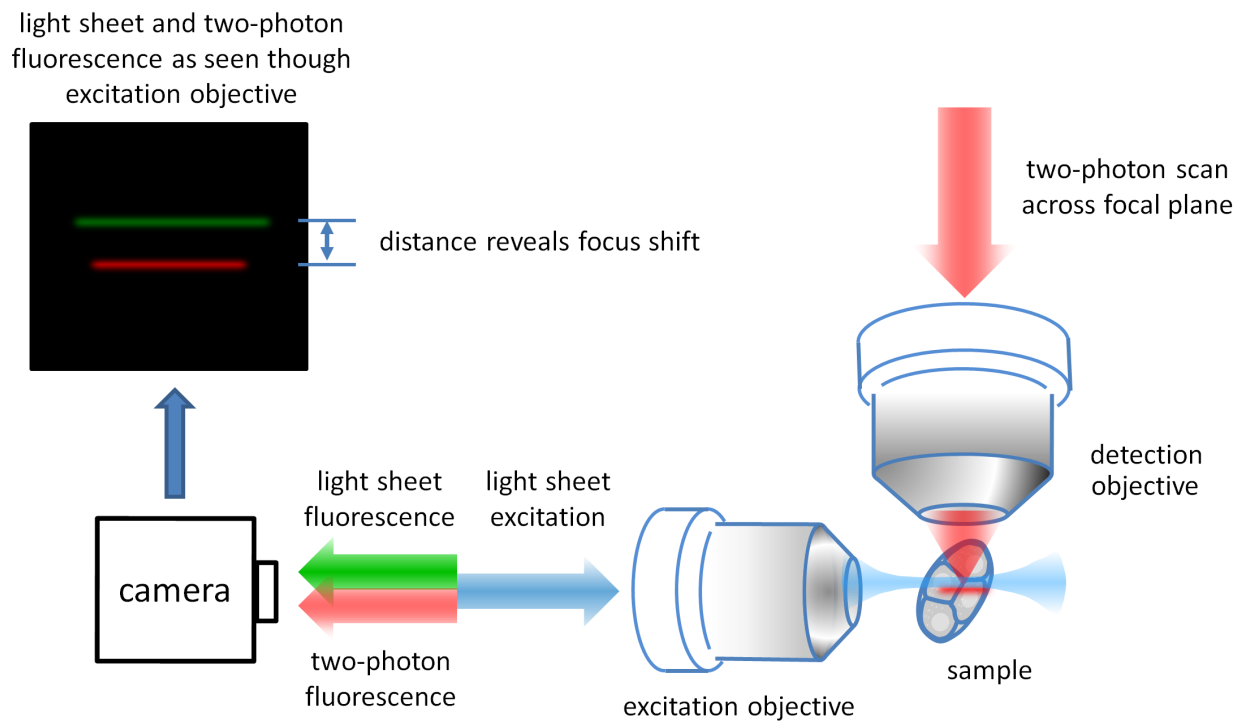


**Fig. S4. Focus correction sequence.** The offset between the excitation light sheet (blue) and detection objective (DO) focal plane (red) is corrected by: (1) recording a side-view image of the light sheet fluorescence (green) and a two-photon scan across the focal plane of DO (red) through the excitation objective camera; (2) fitting the centers of the light sheet and two-photon fluorescence with sub-pixel precision; (3) calculating the axial difference; and (4) adjusting the z-galvo offset to correct the focus (*c.f.* supplement note 5).

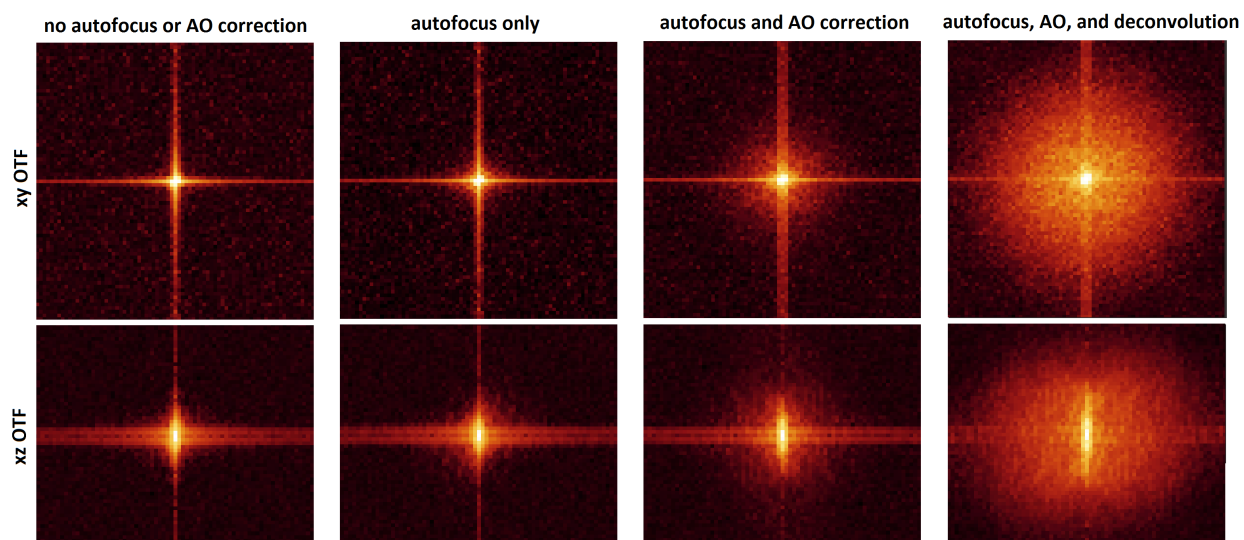


**Fig. S5. OTF comparisons of human stem cell derived organoids.** Maximum intensity projections along  $z$  ( $xy$  OTF, top row) and  $y$  ( $xz$  OTF, bottom row) of the optical transfer function quantitatively show the recovery of information through progressive rounds of increasing correction (*c.f.*, Fig. 1E, Movie 1).

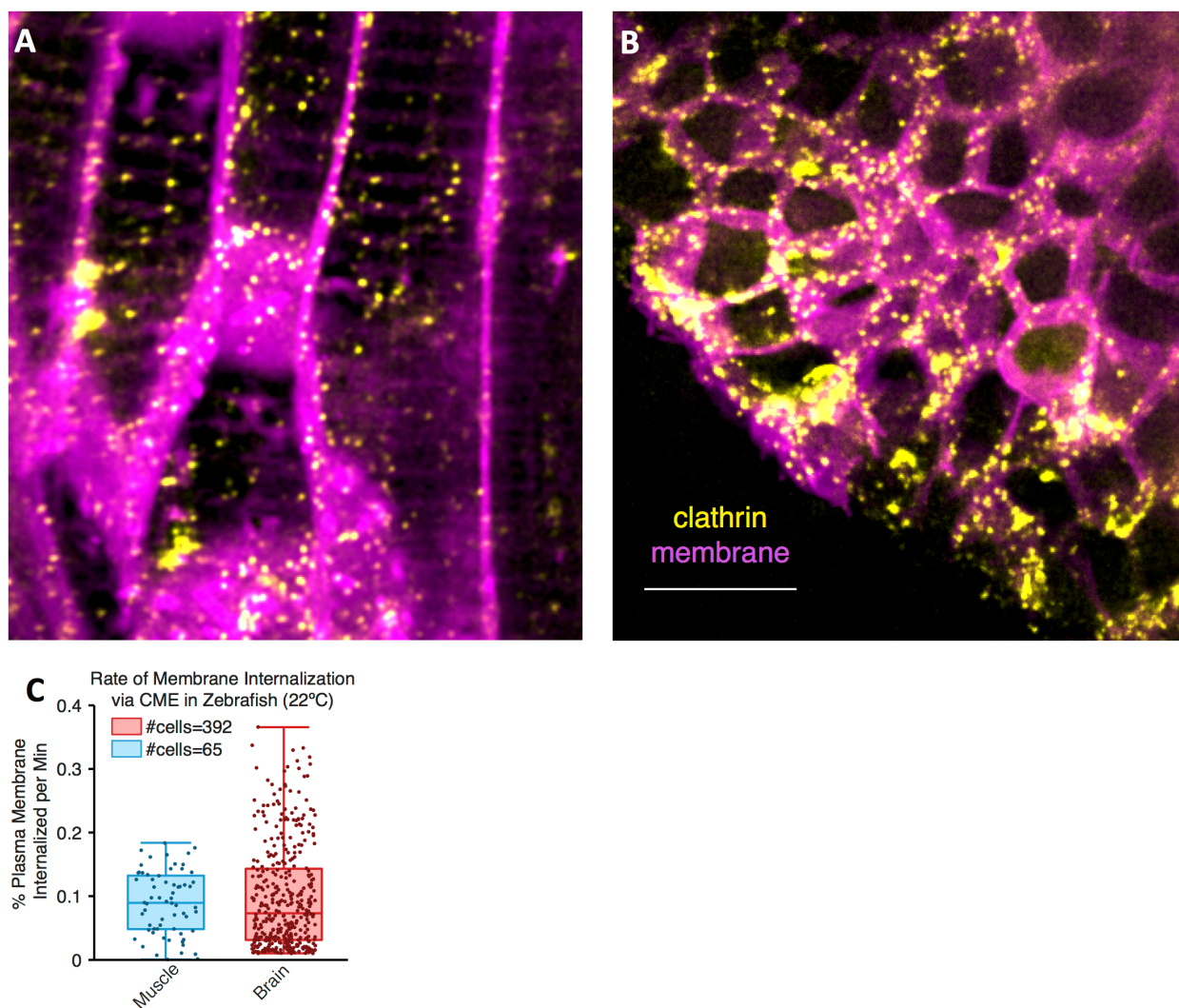


**Fig. S6. Clathrin-mediated endocytosis in zebrafish.** (A,B) Slab rendering of 2 $\mu$ m z-projections from (A) muscle and (B) brain cells expressing clathrin-LCA-mNeonGreen to highlight clathrin-coated pits and coated vesicles (yellow) and mem-mCardinal to label plasma membranes (magenta) in a developing zebrafish embryo 55 hpf. Scale Bar = 10  $\mu$ m. (C) Estimates of the relative amount of cell surface internalized by the clathrin-dependent pathway in muscle and brain.

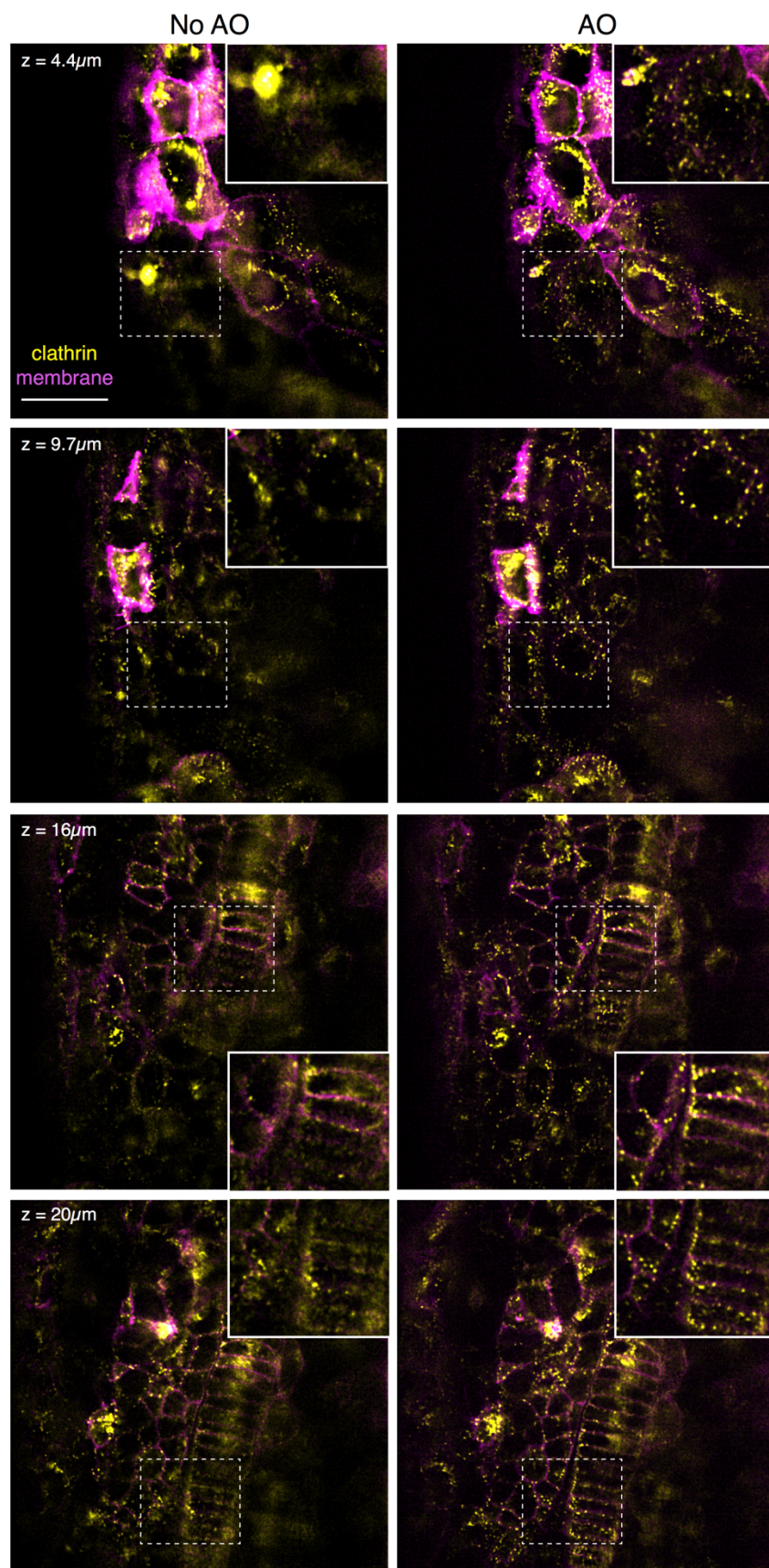


**Fig. S7. Comparison of zebrafish images with and without adaptive optics.** Orthoslices corresponding to four different depths from the spine and notochord of a developing embryo 55 hpf expressing clathrin-LCA-mNeonGreen to highlight clathrin-coated pits and vesicles (yellow) and mem-Cardinal to label plasma membranes (magenta). Both sets of images, before (left) and after (right) adaptive optical correction are shown deconvolved. Scale bar, 10  $\mu\text{m}$ .

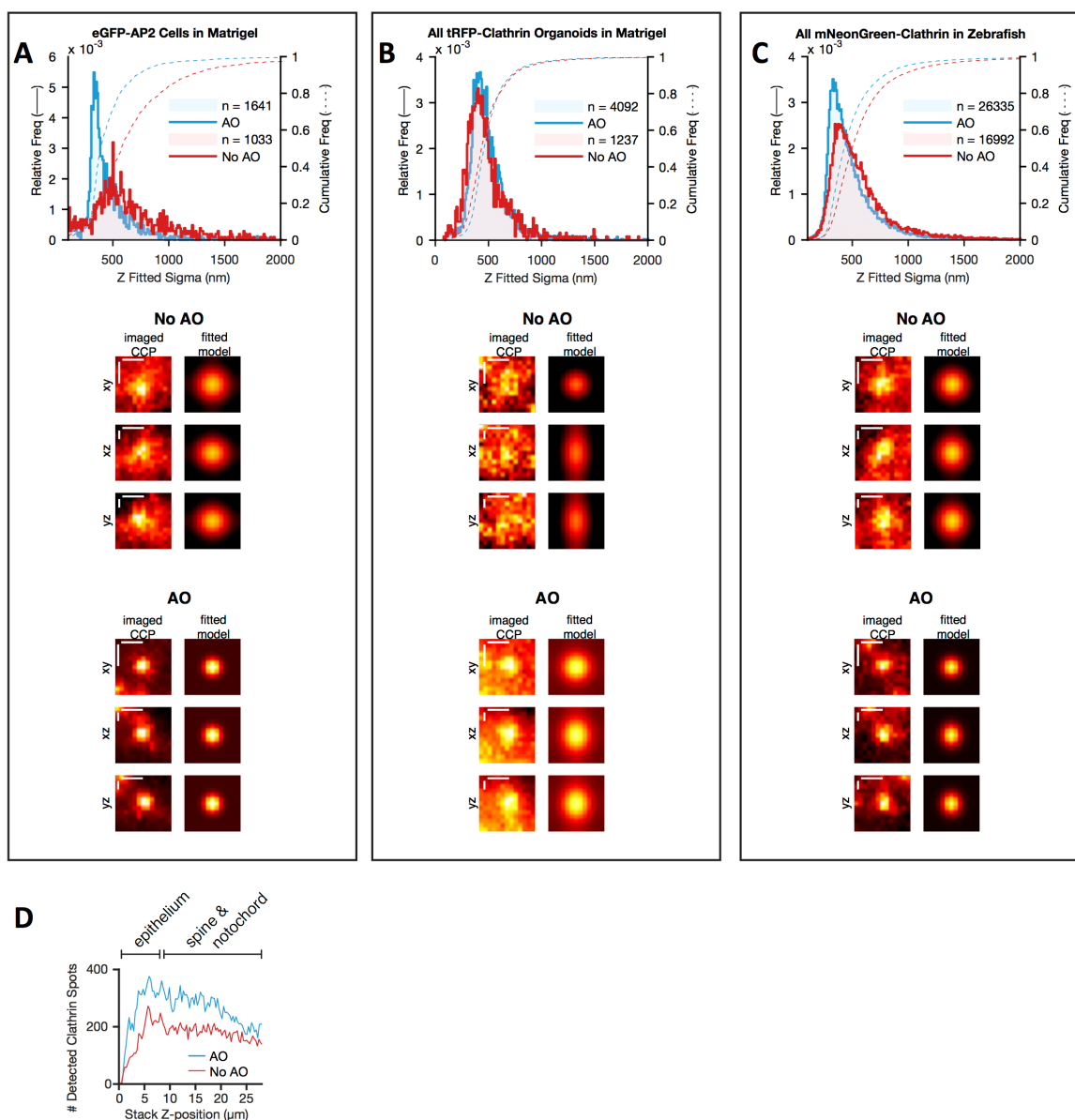


**Fig. S8. Effect of AO in aberrating samples.** Effect of adaptive optical correction on the detection of clathrin coated structures located at: **(A)** the surface of an isolated, gene edited SUM cell expressing AP2-EGFP and embedded in  $\sim 200 \mu\text{m}$  of Matrigel; **(B)** an intestinal epithelial organoid derived from gene-edited *hESCs* expressing clathrin light chain A-tRFP and embedded in Matrigel; and **(C)** the dorsal surface of a zebrafish embryo 24 hpf expressing *Dr.cltA-3xGSS-mNeonGreen*. Top row compares the localization precision along the z-axis of the fluorescent puncta from a single time point extracted from a time series, visualized using LLSM with and without adaptive optics. Middle row shows three representative images, before adaptive optical correction, of diffraction-limited clathrin coated structures and their corresponding 3D Gaussian fits. Bottom row shows similar images and fits of three additional clathrin puncta after AO correction. Scale bar,  $0.5 \mu\text{m}$ . **(D)** Comparison in the number of detects spots imaged with and without adaptive optics at different z-positions from the surface (epithelium) to deeper regions (spine & notochord) of the zebrafish embryo.

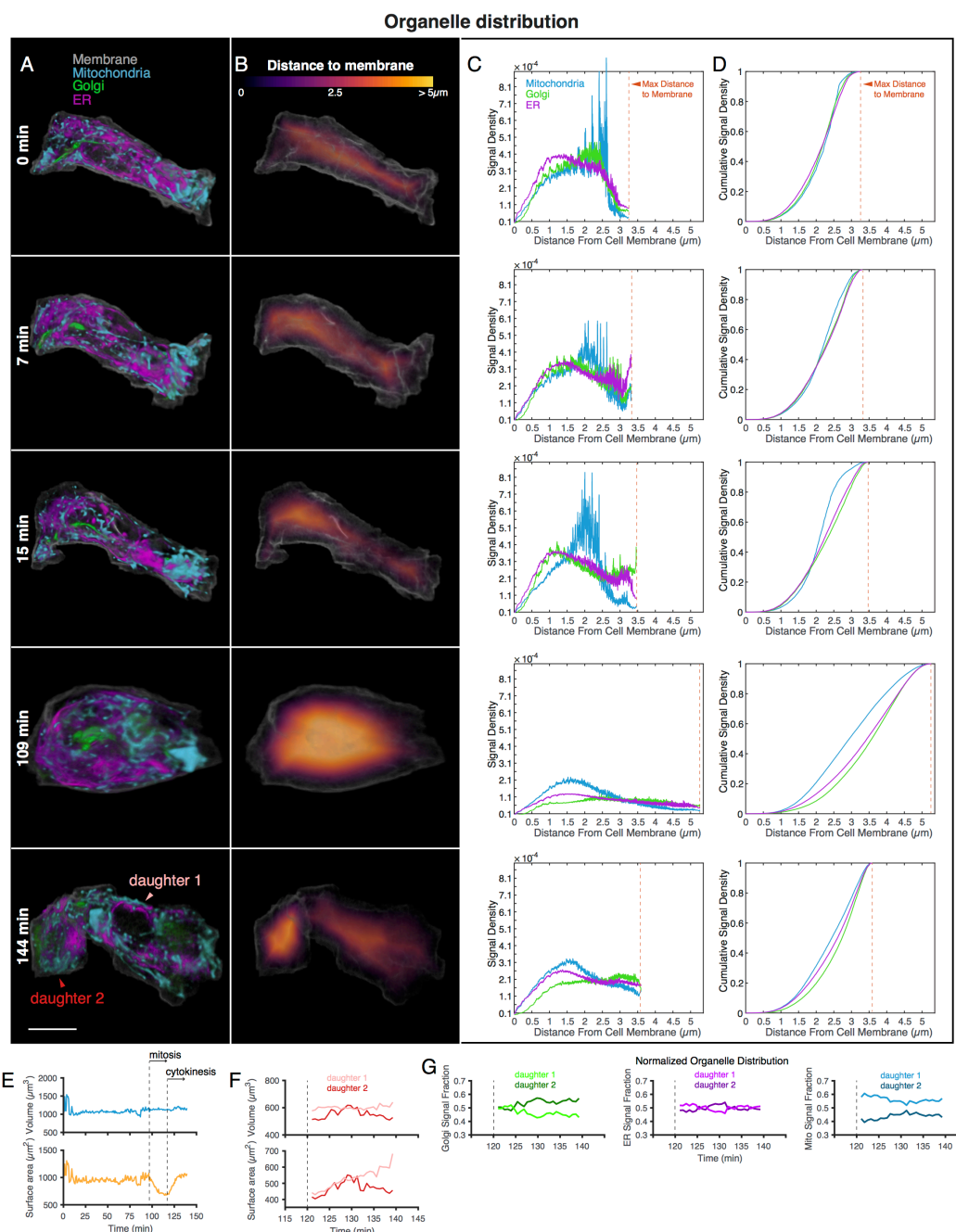


**Fig. S9. Spatial distribution of subcellular organelles in a dividing zebrafish brain cell.** The brain of a zebrafish embryo expressing markers for the cell surface (mem-citrine), trans-Golgi apparatus (GalT-mNeonGreen) and endoplasmic reticulum (Sec61b-tagRFPT) and stained for mitochondria (MitoTracker Deep Red) was imaged 14-16 hpf. **(A)** 3D volume rendering of a single cell imaged at different stages during cell division from interphase through cytokinesis. Scale bar, 5  $\mu\text{m}$ . **(B)** Distance map from the cell surface to the cell center. **(C, D)** Relative location of the organelles expressed as: **(C)** probability; and **(D)** cumulative frequency distributions. **(E-F)** Changes in cell area and volume during mitosis and cytokinesis (*c.f.*, Movie 4). **(G)** Fraction of total organelle fluorescence distributed in the daughter cells.

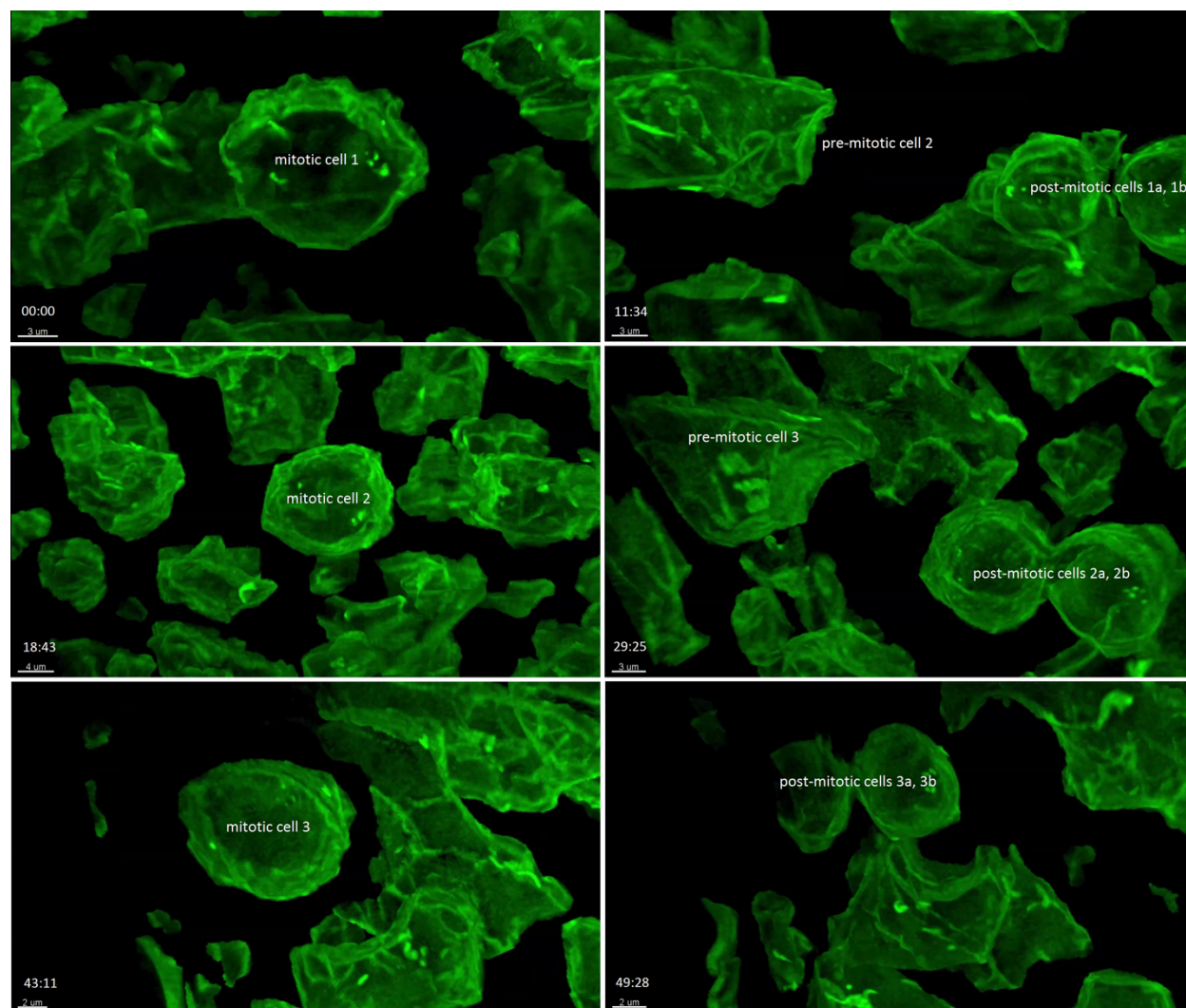


**Fig. S10. Spatial correlation of adjacent dividing cells in the brain of the zebrafish embryo.** Example of three neighboring cells undergoing sequential cell division. The images correspond to the indicated time points from the time series in Movie 4; the cells were computationally displaced from one another for easier identification. Scale bars, 3  $\mu\text{m}$ .

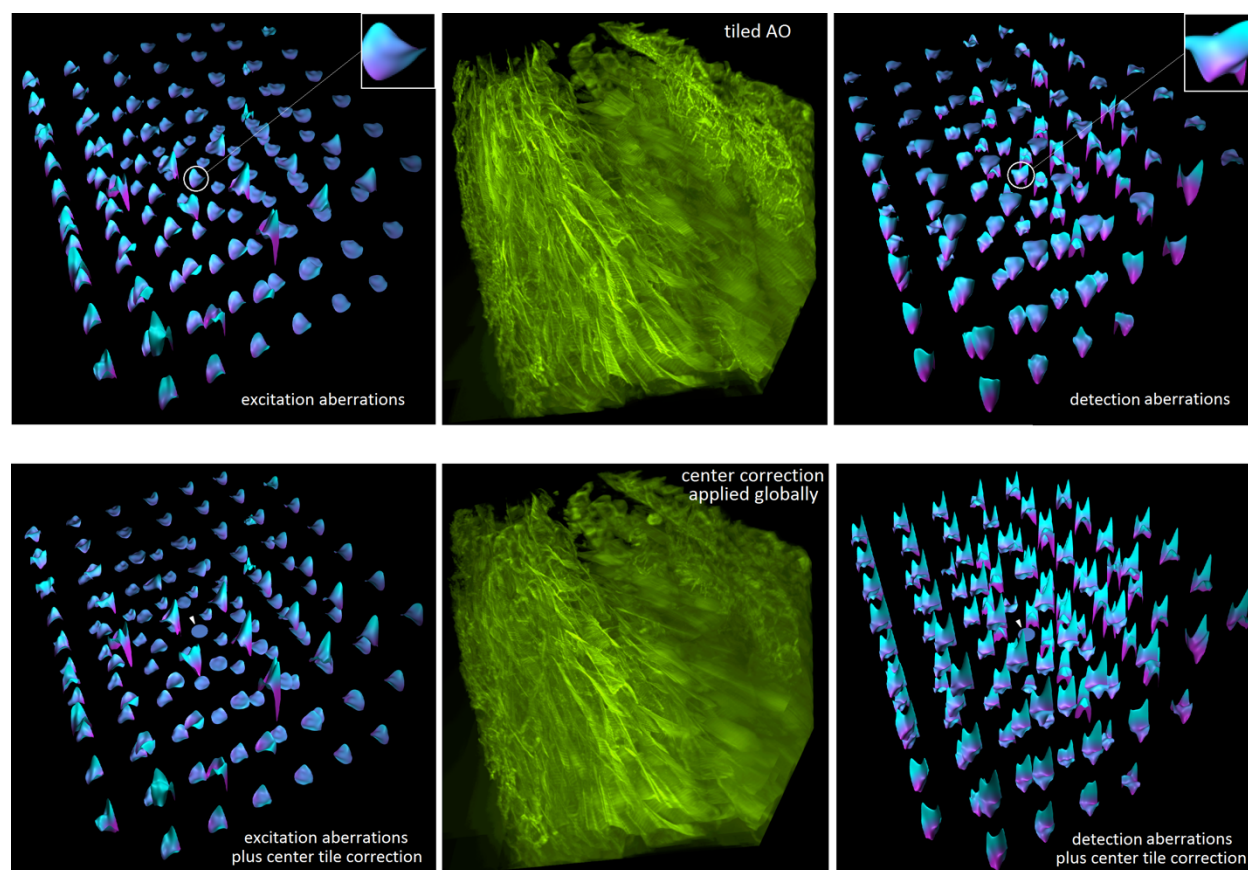


**Fig. S11. Multi-tile AO-LLSM volume acquisition.** A  $213 \times 213 \times 113 \mu\text{m}$  volume of muscle and spinal cells in a zebrafish embryo expressing an EGFP plasma membrane marker, imaged 96 hpf. The volume was stitched together from  $7 \times 7 \times 3$  subvolumes, where it is assumed that a single pair of excitation and detection corrections can recover diffraction-limited performance in each subvolume. In the top example, independent excitation (left) and detection (right) corrections measured and applied to each subvolume indeed recover optimal performance. In the bottom example, the AO corrections (insets, top row) determined for the central tile (top row, circled) are applied to all subvolumes, under the assumption that a single corrective pair is sufficient to cover the entire volume. While this correctly cancels the aberrations in the center tile, it can actually increase the total aberration in surrounding tiles (bottom, left and right), where different aberrations exist in practice, and thereby reduce the overall imaging performance (bottom center) (*c.f.*, Fig. 4A, movie S4).

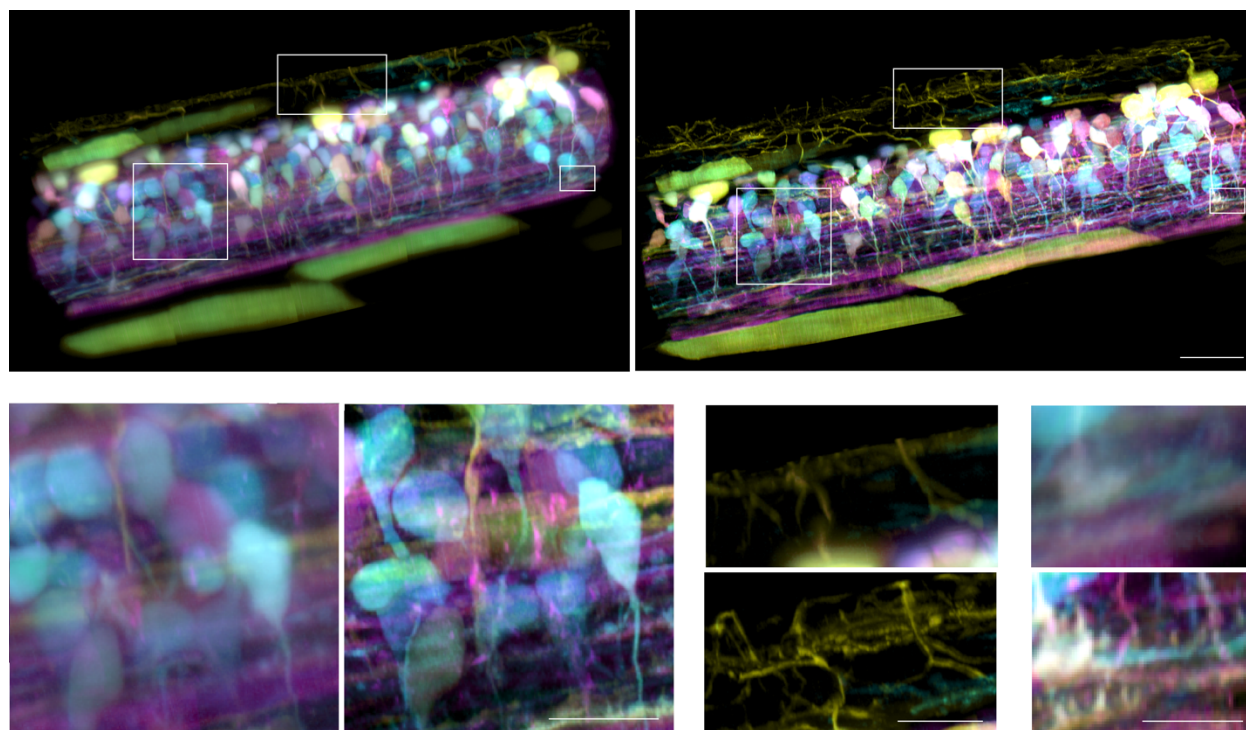


**Fig. S12. *In vivo* imaging of a developing neural circuit.** Newly differentiated neurons in a developing zebrafish spinal cord expressing stochastic combinations of three fluorophores (volume rendered in cyan, yellow and magenta) are shown in uncorrected (top left) and AO corrected (top right) stitched volumes. Three boxed regions at top are shown at higher magnification below to show before and after AO comparisons in more detail (*c.f.*, Fig. 6A-D, Movie 8, movie S6).

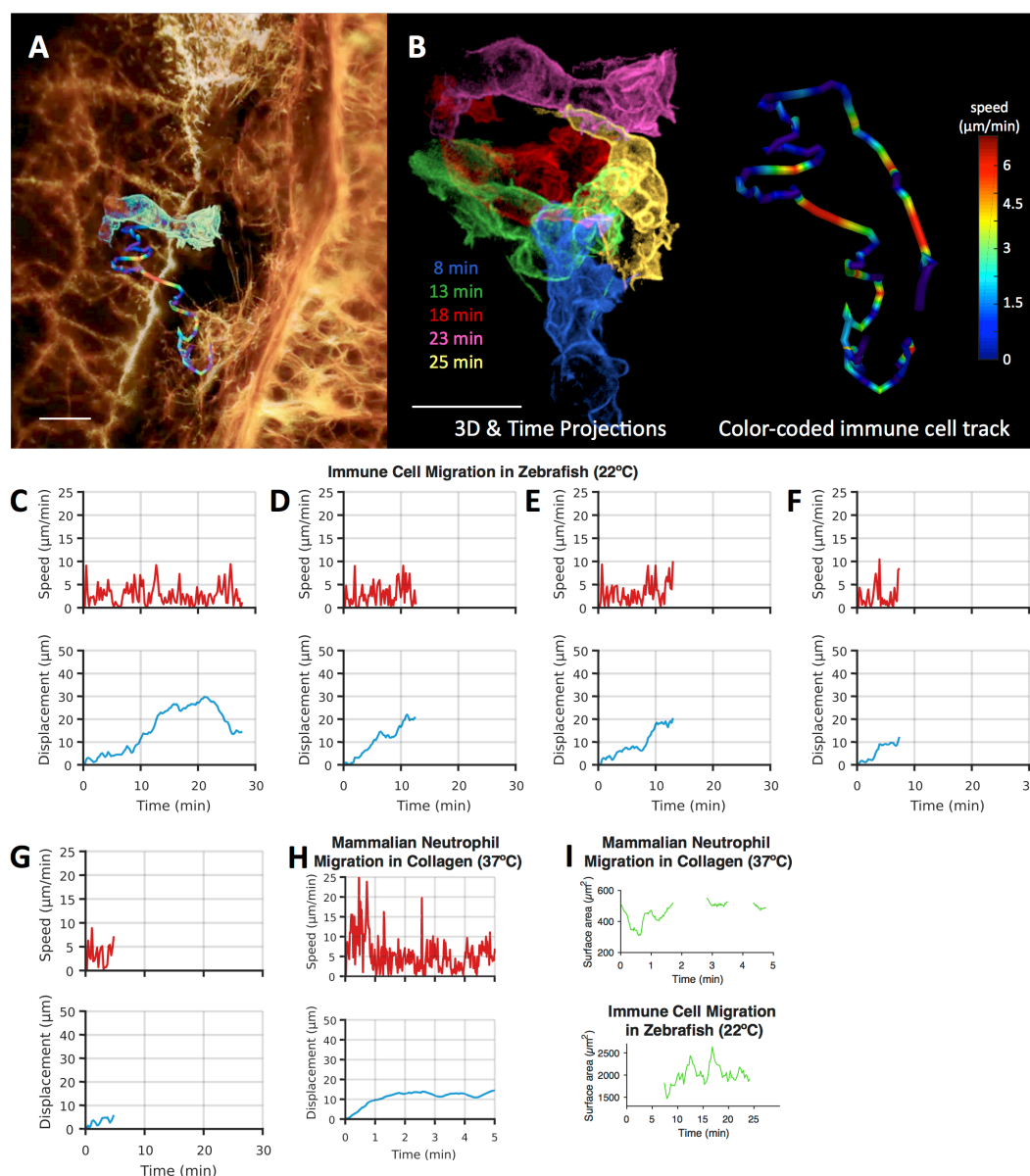


**Fig. S13. Comparative migration rates of immune cells in zebrafish embryos versus a collagen mesh.** (A) 3D volume rendering at a single time point from a time series (22 min, Movie 9) showing a migrating immune cell in the interstitial space near the ear of a zebrafish embryo expressing a citrine membrane marker, 70 hpf. The segmented immune cell (green) and its past 3D-trajectory color coded by speed are overlaid. Scale bar, 10  $\mu\text{m}$ . (B) Volume renderings of the same cell, projected at five different time points spanning 25 min, together with the corresponding complete 3D-trajectory during this time interval. (C-G) Speed and displacement from the initial position for five immune cells in three different zebrafish embryos; plot (C) corresponds to the cell depicted in (A, B). (H) Speed and displacement from the initial position for a mammalian HL-60 neutrophil migrating in a 3D collagen mesh, taken from the data were extracted from the time series in Movie 9 of (6). (I) Changes in surface area of the immune cell in (C) and the HL-60 cell in (H).

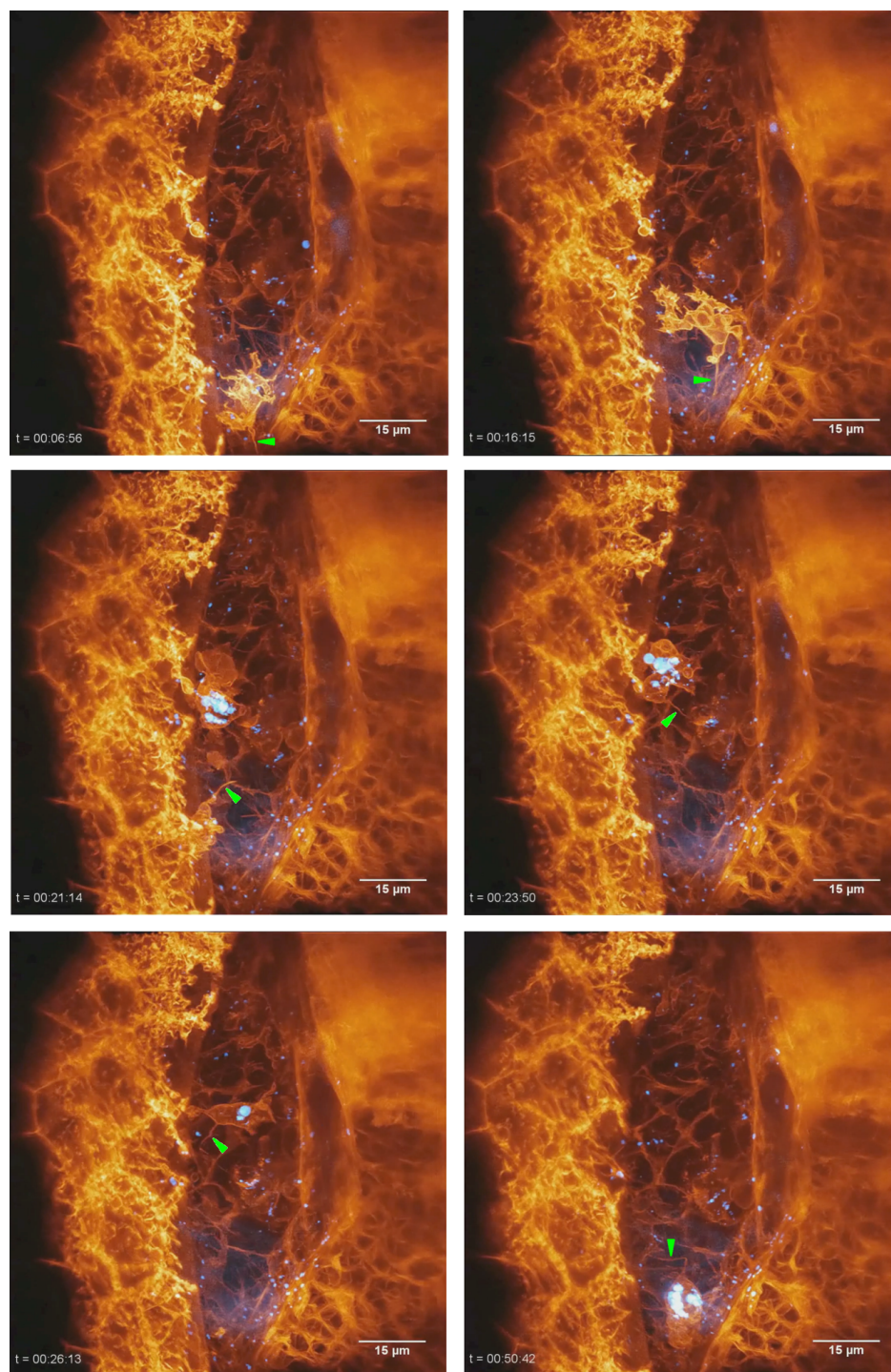


**Fig. S14. Trailing tail of a migrating immune cell in the ear of a zebrafish embryo.** Green arrows highlight the presence of a tail trailing at the end of an immune cell at six different time points during its migration in the interstitial space near the ear of a zebrafish embryo expressing a citrine membrane marker, 70 hpf (*c.f.*, Movie 9).

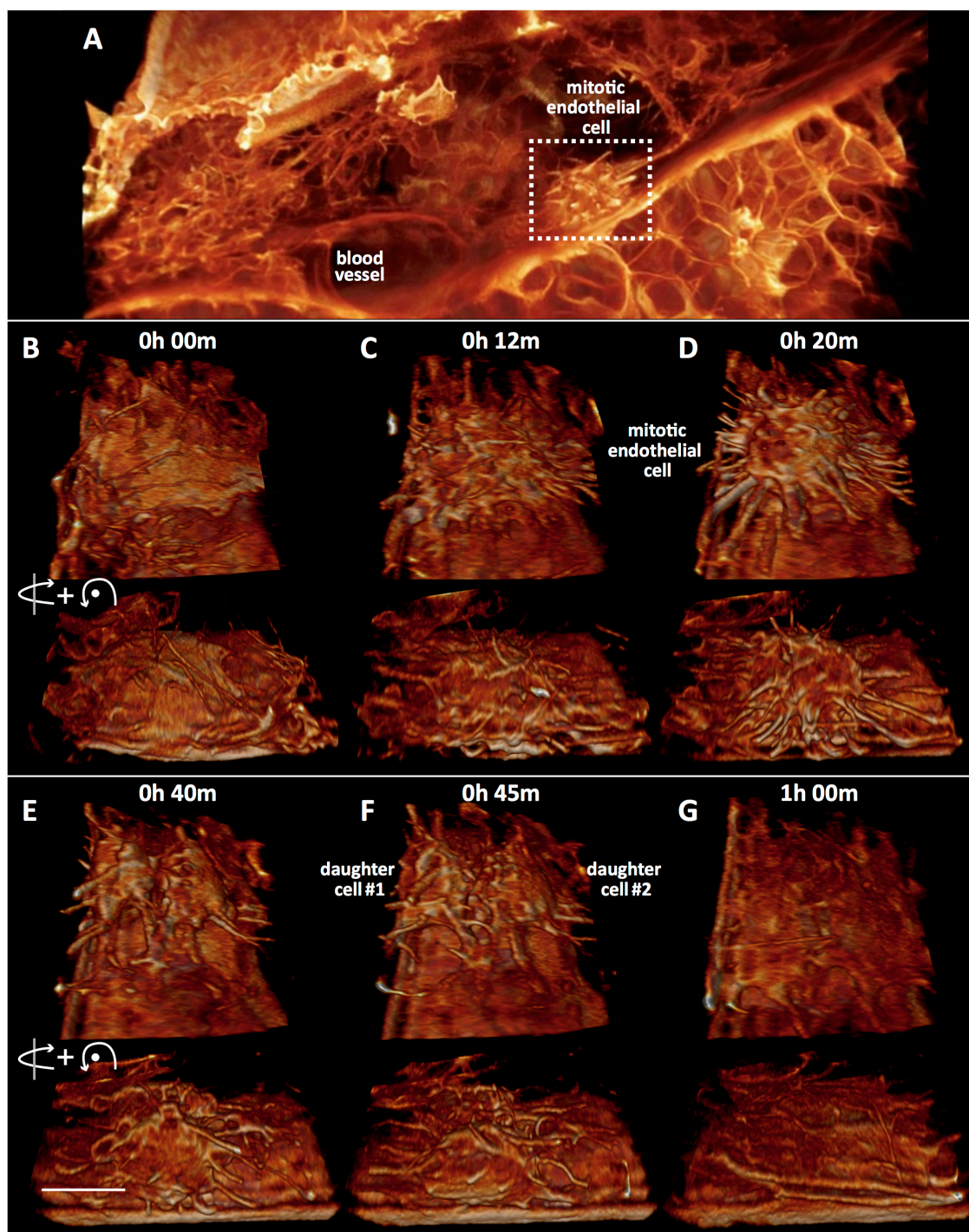


**Fig. S15. Division of an endothelial cell lining the hindbrain in a zebrafish embryo.** (A-G) 3D renderings at six time points from a time series (Movie 9) illustrating an endothelial cell undergoing division. (A) The cell and its surroundings at  $t = 20$  min. (B-G) Enlarged views presenting two orientations. The cell is flat before (B) and after (G) mitosis, and a number of projections anchor the cell to the underlying hindbrain lining during mitosis (C-F).

## Extravasated Cancer Cell Membrane Dynamics

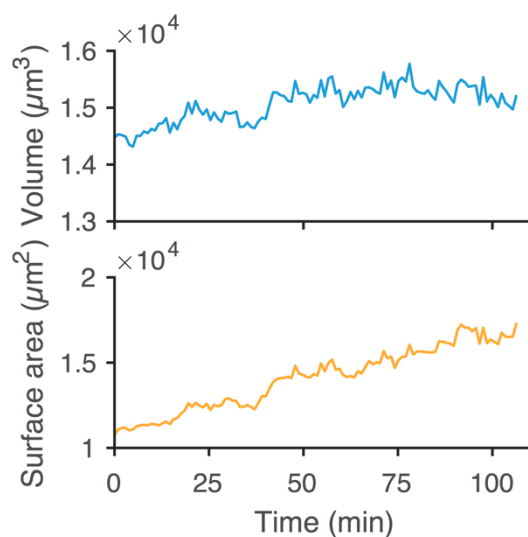


**Fig. S16. Morphological changes in an extravasating cancer cell.** Volume and surface area versus time of a MDA-MB-231 cell in the process of transendothelial migration. While portion of this extravasating cell remained outside the blood vessel, it generated actin-rich projections to survey the surrounding tissue, resulting in an increase of its surface area by  $\sim 50\%$  within two hours (*c.f.*, Fig 6I, Movie 10).

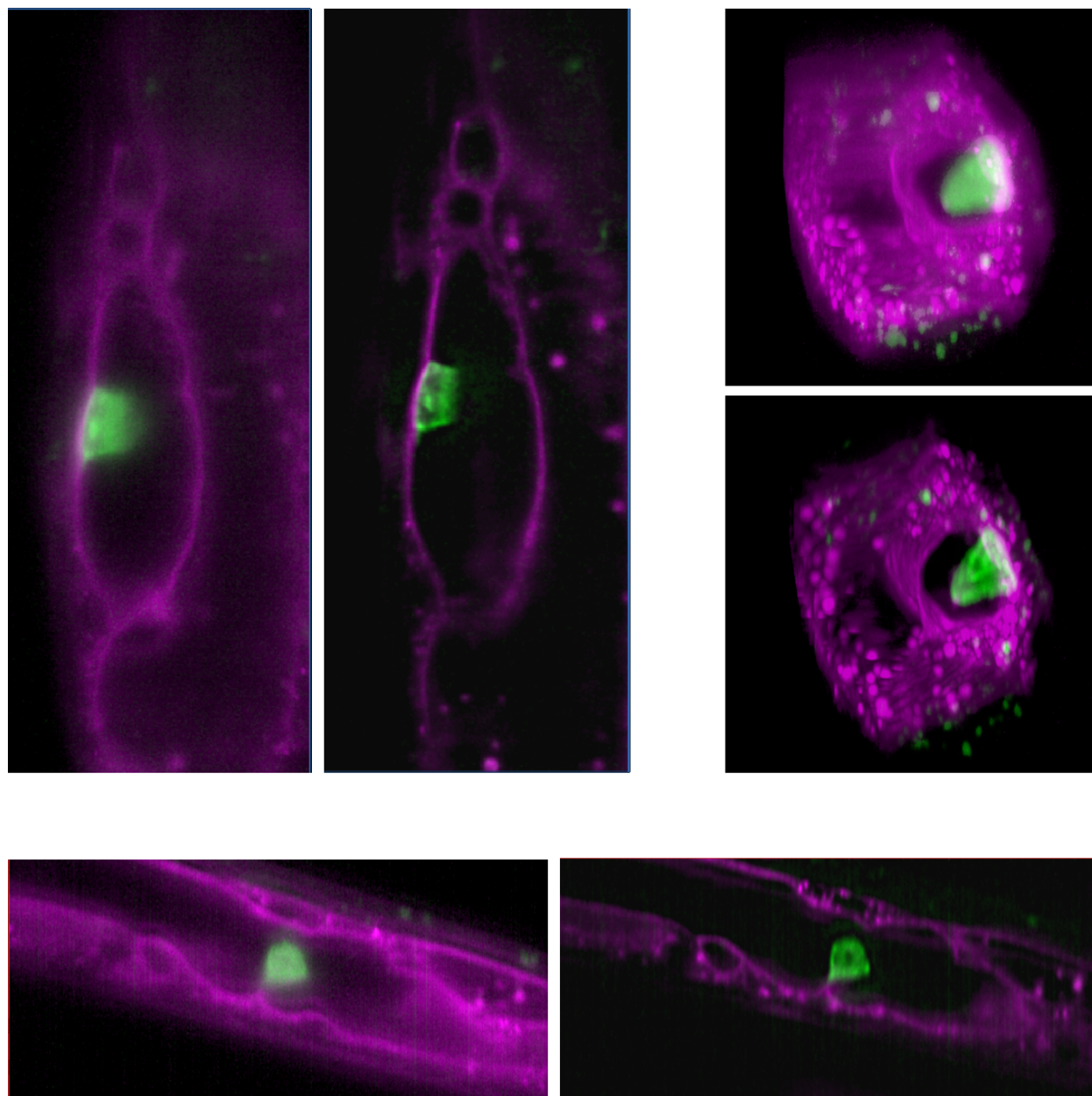


**Fig. S17. *C. elegans* anchor cell invasion into the vulval epithelium.** (Top left) Uncorrected (left) and AO corrected (right) single  $xy$  orthoslices depicting a lateral view of the *C. elegans* anchor cell (AC), visualized with mCherry::moesinABD (green), and the basement membrane, labelled with laminin::GFP (magenta), prior to the initial basement membrane breach. (Top right) Volume rendered transverse views, uncorrected (top) and AO corrected (bottom), of the AC adhering to the basement membrane prior to invasion. (Bottom) Ventral uncorrected (left) and AO corrected (right) views from single  $xz$  orthoslices of the AC prior to invasion. (*c.f.*, movie S7)

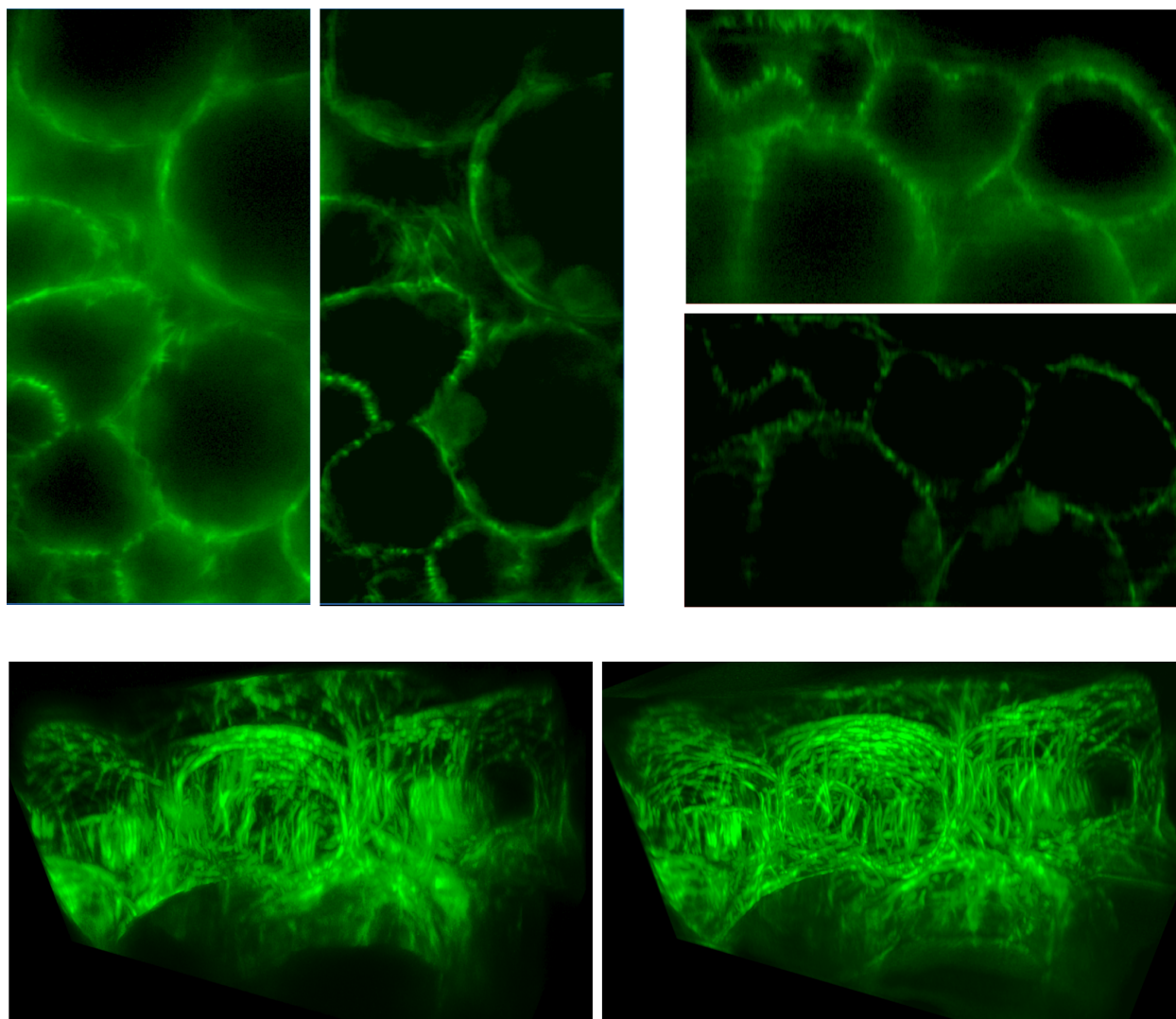


**Fig. S18. AO-LLSM of *Arabidopsis* cotyledon epidermal cells.** (Top left) Uncorrected (left) and AO corrected (right) single  $xy$  orthoslices from a plant transgenic for microtubule reporter  $p35S::GFP-MBD$ . (Top right) A similar comparison from a single pair of  $xz$  orthoslices. (Bottom) 3D volumetric rendering of microtubules in the epidermal cells before (left) and after (right) AO correction. (*c.f.*, movie S8).

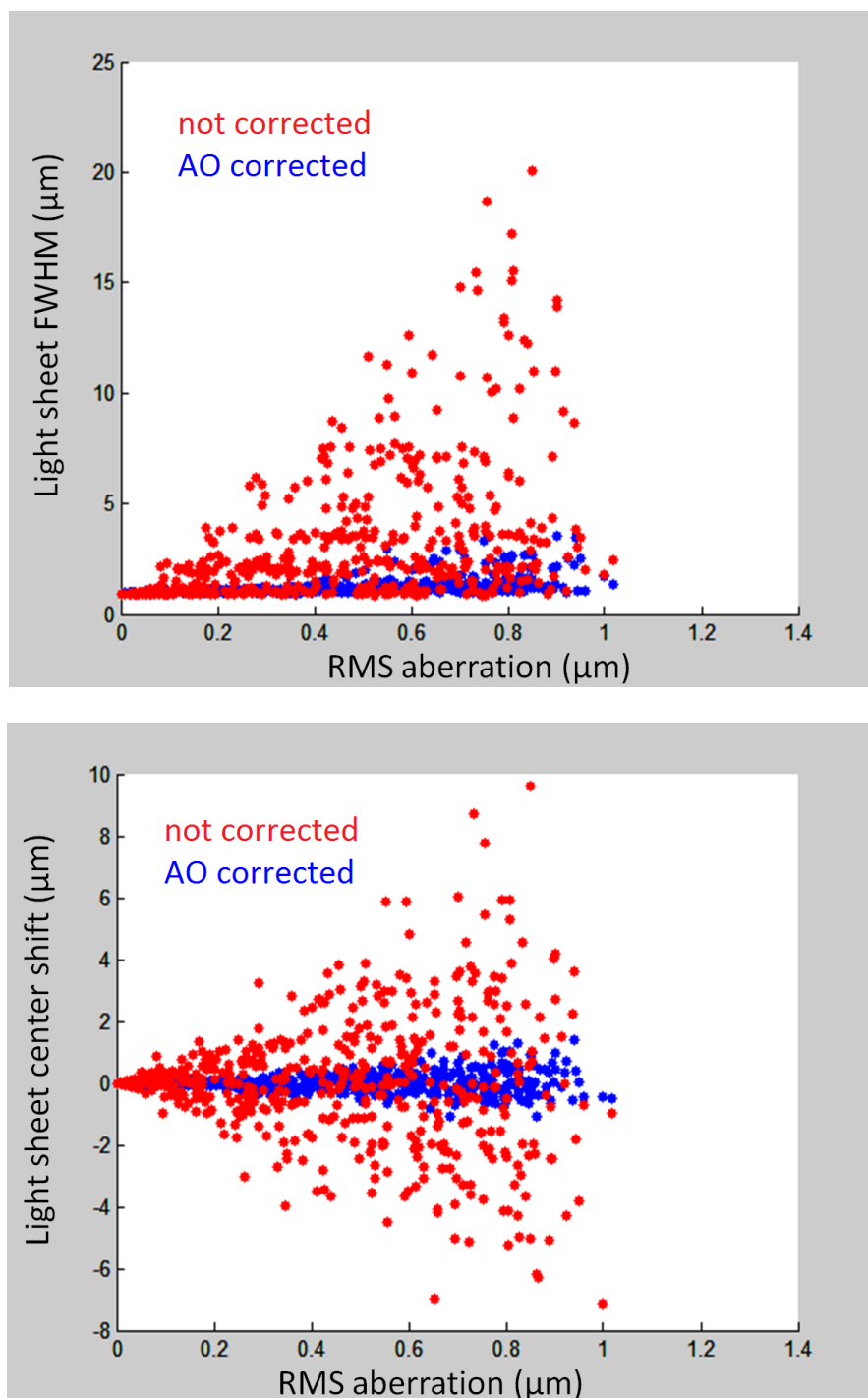


**Fig. S19. Monte Carlo simulations of aberration-induced distortions to a lattice light sheet.** Blooming (top) and axial displacement (bottom) of a lattice light sheet before (red) and after (blue) application of adaptive optics, for simulated aberrations of RMS amplitude as shown, with each simulation comprised of randomly selected combinations of Zernike modes  $Z_n^m(x', y')$  through  $n = 9$ .

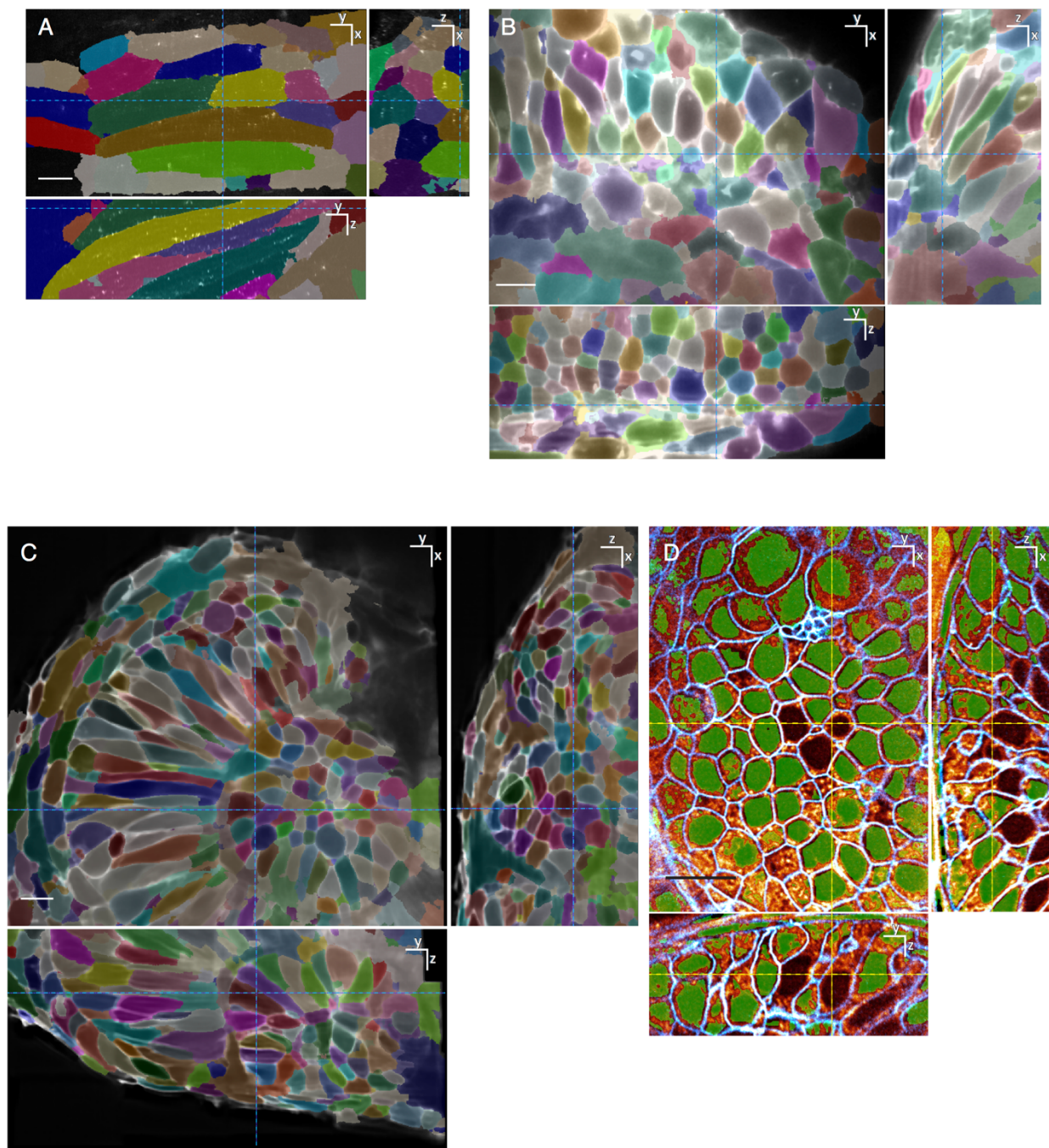


**Fig. S20. Detection of boundaries in zebrafish embryos.** Examples of the correspondence between the segmentation map of the cell surface obtained with ACME and imaging data corresponding to: (A) muscle (*c.f.*, Fig 2, Movie 3); (B) brain (*c.f.*, Fig 3, Movie 4); and (C) the eye (*c.f.*, Fig 5, Movie 7). A random color was assigned to each cell. (D) Correspondence between the segmentation map of the nucleus (green) and imaging data in the eye (*c.f.*, Fig 3, Movie 5). Imaging data of clathrin in (A) and the cell surface in (B, C) is raw, but deconvolved data for the cell surface and endomembranes is shown in (D).

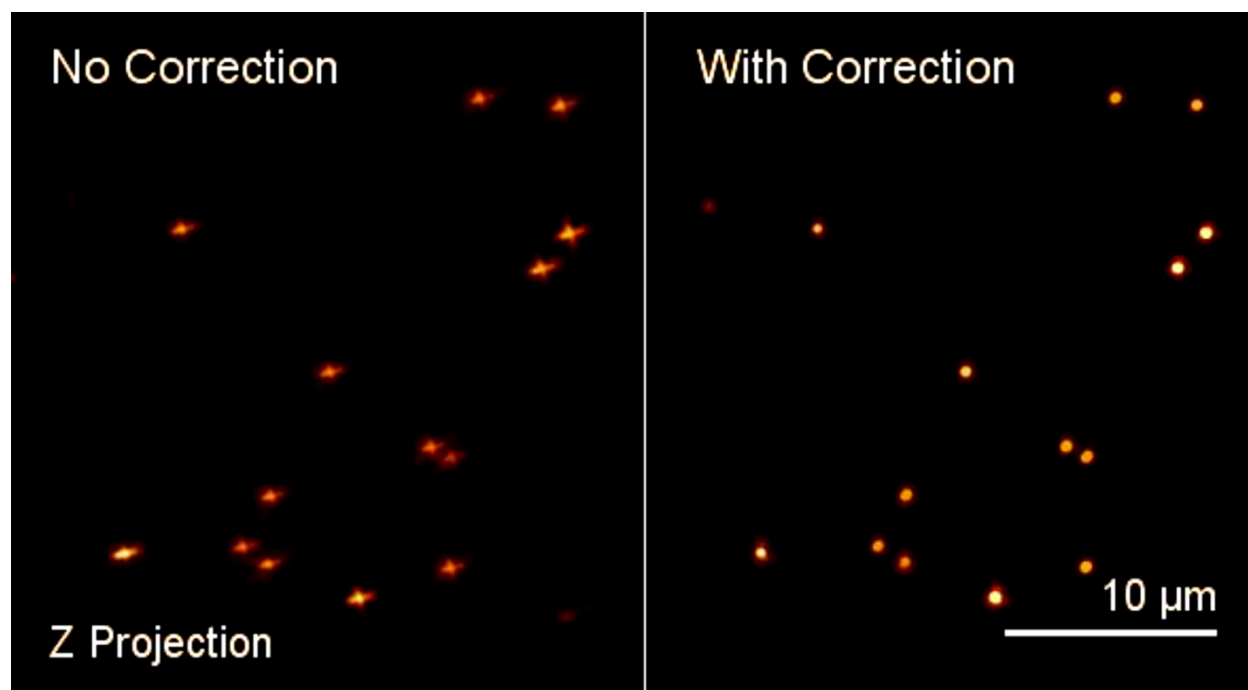
## Supplementary Table

Table S1. Imaging conditions for all experiments.

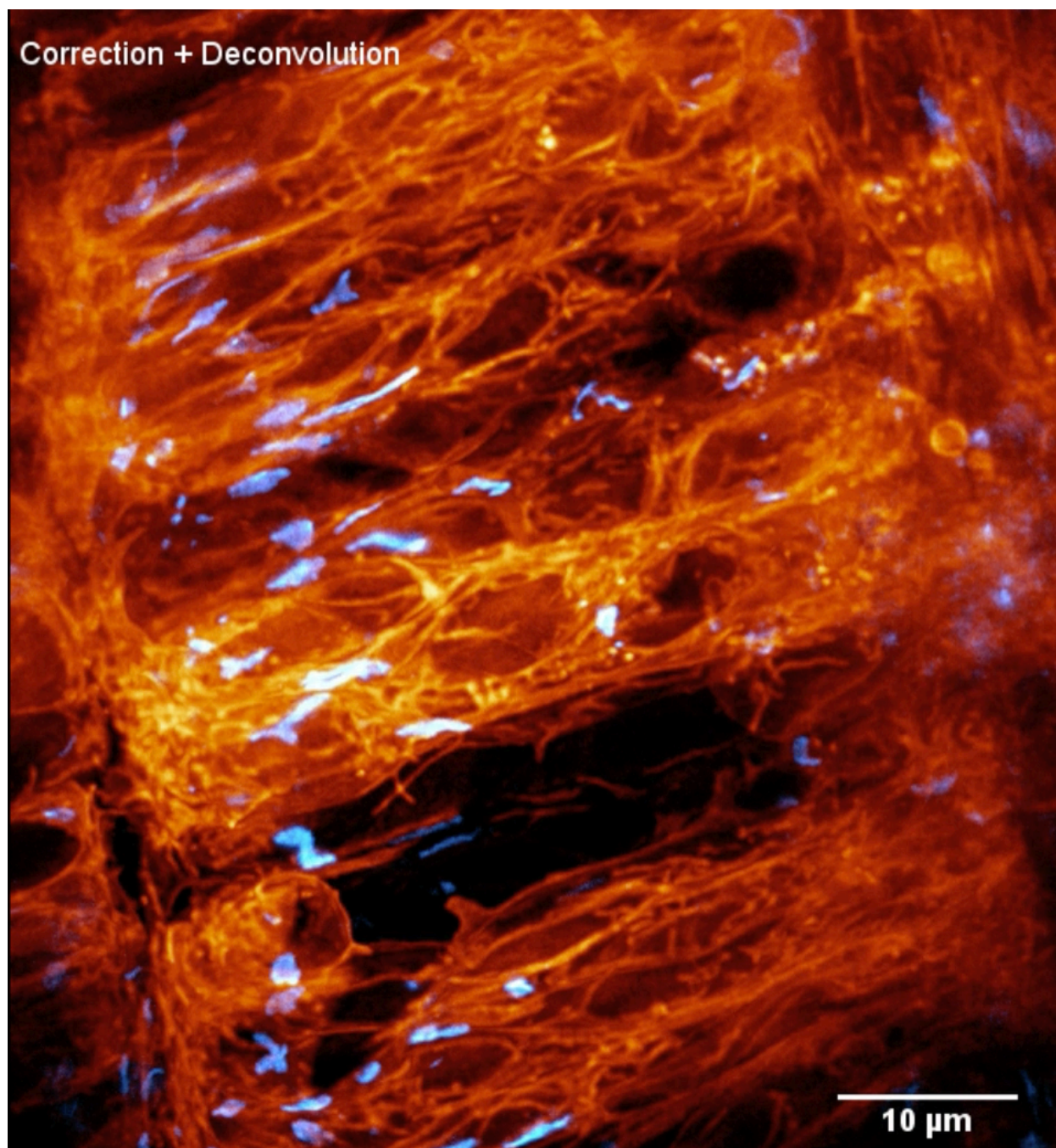
	Sample (imaging T, °C) (Age)	Fluorescent label	Voxel volume (dx, dy, dz/ds nm <sup>3</sup> )	Image Volume (x,y,z) μm <sup>3</sup>	Exposure time (ch1, ch2...) (# time pts) (image+rest)	λ: Power (μW)	Square Lattice Excitation NA (outer, inner), beam length (μm)	Photo- bleaching correction	# volumes; Stitched?; Stitching Algorithm
1B, M1	Organoid hESCs 37°C	tagRFPT-Clathrin LCA EGFP-Dynamin	97 x 97 x 200	49.7 x 68.3 x 30.2	(5ms, 5ms) (240pts, 240pts) (2.8s)	488: (104) 560: (149)	0.517, 0.55, 30	Vision4D	1; no
1D, 3F, MS2	Zebrafish 22°C 24hpf	Citrine-membrane mNeonGreen-galt1 mCardinal-cox8a	97 x 97 x 200	49.7 x 68.3 x 9.8	(26ms, 26ms) (100pts, 100pts) (7.85s+6.13s)	488: (27) 560: (31)	0.517, 0.55, 30	Vision4D	1; no
2A, M2	Zebrafish 22°C 82hpf	dsRed-Clathrin LCA	97 x 97 x 250	74.5 x 99.3 x 40.25	45ms 100pts (7.24s+2.7s)	560: (186)	0.517, 0.55, 30	Image J – histogram matching	1; no
2BC, M3, MS3	Zebrafish 22°C 55hpf	mNeonGreen- Clathrin LCA mCardinal-membrane	97 x 97 x 200	74.5 x 99.3 x 30.2	(26ms, 26ms) (100pts, 1pt) (3.93s+3.57s)	488: (27) 560: (31)	0.517, 0.55, 30	no	1; no
3AB, S9A, S10, M4	Zebrafish 22°C 14hpf	Citrine-membrane mNeonGreen-galt1 tRFPT-sec61β Mito FM dye	97 x 97 x 200	74.5 x 99.3 x 40.6	(19ms, 19ms, 19ms) (200pts, 200pts, 200pts) (11.46s+32.29s)	488: (16) 560: (31) 642: (27)	0.517, 0.55, 30	no	1; no
3CD, M5	Zebrafish 22°C 30hpf	Citrine-membrane endomembranes (bodipyMethylEster)	97 x 97 x 200	45.3 x 64.1 x 44.5	(10ms, 10ms) (200pts, 200pts) (4.02s+6.51s)	488: (16) 560: (31)	0.517, 0.55, 30	no	1; no
4A,B, S11, MS4	Zebrafish 22°C 96 hpf	EGFP-membrane	97 x 97 x 180	34.1 x 34.1 x 50.2 (per volume) 213 x 213 x 113 (stitched)	8ms, 1pts (2.23 + 2.1s per tile; 11.1 min per time point)	488: (16)	0.517, 0.55, 30	Vision4D	7x7x3; yes MATLAB Stitching + DMG
4C	Zebrafish 22°C 30hpf	EGFP-membrane	97 x 97 x 250	34.9 x 46.6 x 25.3 (per volume) 166.6 x 180.2 x 134.7 (stitched)	10ms, 76pts (1.01s + 2.35 per tile; 7.4 min per time point)	488: (32)	0.517, 0.55, 30	Vision4D	5x4x7; yes MATLAB Stitching + DMG
4D, M6, MS5	Zebrafish 22°C 30hpf	Bodipy green, nuclear-localized GCaMP6fast, DsRed (glutamatergic ipsilateral projecting neurons)	97 x 97 x 150	34.9 x 49.6 x 35.1 (per volume) 156 x 220 x 162 (stitched)	(10ms, 10ms) (30pts, 30pts) (4.68s+2.34s per tile; 30 min per time point)	488: (32) 560: (47)	0.517, 0.55, 30	Vision4D	5x5x6; yes MATLAB Stitching + DMG
5A-D, M7	Zebrafish 22°C 24hpf	Citrine-membrane mNeonGreen-galt1 tRFPT-sec61β Mito FM dye	97 x 97 x 200	34.9 x 40.6 x 30.2 (per volume) 134 x 149.2 x 68.2 (stitched)	(9ms, 9ms, 9ms) (29pts, 29pts, 29pts) (4.07s per tile; 5.9 min per time point)	488: (16) 560: (31) 642: (27)	0.517, 0.55, 30	no	4x4x3; yes ImageJ Grid/Collection Stitching
6A-D, S12-15, M8, MS6	Zebrafish 22°C 58hpf	Autobow, stochastic expression of phi-YFP, Cerulean and mKate	97 x 97 x 150	34.9 x 40.6 x 90.2 (per volume) 60.5 x 228.9 x 90.2 (stitched)	(30ms, 30ms, 30ms) (72pts, 72pts, 72pts) (54.09s + 6.7s per tile; 20.9 min per time point)	445 488: (40) 560: (93)	0.517, 0.55, 30	Vision4D	5x2x1; yes MATLAB Stitching + DMG
6EF, M9	Zebrafish 22°C 70hpf	Citrine-membrane TexasRed - 3kDa Dextran	97 x 97 x 200	99.3 x 99.3 x 40.2	(10ms, 10ms) (597pts, 597pts) (4.02s+9.00s)	488: (11) 560: (22)	0.517, 0.55, 30	no	1; no

6G, M10	Zebrafish 22°C 48hpf xenograft with MDA- MB-231 Human Cells	EGFP- <i>kdr1</i> mCherry-CAAX	97 x 97 x 180	34.9 x 68.3 x 50.2	(10ms, 10ms) (47pts, 47pts) (5.58s+50.97s)	488: (8) 560: (31)	0.517, 0.55, 30	Vision4D	1; no
6H, M10	Zebrafish 22°C 48hpf xenograft with MDA- MB-231 Human Cells	EGFP- <i>kdr1</i> mCherry-CAAX	97 x 97 x 180	34.9 x 68.3 x 50.2	(10ms, 10ms) (60pts, 60pts) (5.58s+50.99s)	488: (8) 560: (31)	0.517, 0.55, 30	Vision4D	1; no
6I, M10	Zebrafish 22°C 48hpf xenograft with MDA- MB-231 Human Cells	EGFP- <i>kdr1</i> mCherry-CAAX	97 x 97 x 180	34.9 x 68.3 x 50.2	(10ms, 10ms) (60pts, 60pts) (5.58s+52.97s)	488: (16) 560: (46)	0.517, 0.55, 30	Vision4D	1; no
S6	Zebrafish 22°C 55hpf	mNeonGreen- Clathrin LCA mCardinal-membrane	97 x 97 x 200	74.5 x 99.3 x 30.2 74.5 x 99.3 x 2 (shown, z- projection)	(26ms, 26ms) (100pts, 1pt) (3.93s+3.57s)	488: (16) 560: (31)	0.517, 0.55, 30	no	1; no
S7, S8C	Zebrafish 22°C 24hpf	mNeonGreen - Clathrin LCA mCardinal-membrane	97 x 97 x 200	74.5 x 99.3 x 30.2	(26ms, 26ms) (100pts, 1pt) (3.93s+3.57s)	488: (16) 560: (31)	0.517, 0.55, 30	no	1; no
S8A	SUM159 cell embedded in matrigel 37°C	EGFP-AP-2	97 x 97 x 250	49.7 x 49.7 x 25.2	20ms 2pts (2.02s+0.46s)	488: (53)	0.517, 0.55, 30	no	1; no
S8B	Organoid SUM159 embedded in matrigel 37°C	tagRFPT -AP-2	97 x 97 x 250	77.6 x 99.3 x 24.5	26ms 100pts (2.55s+0.47s)	560: (46)	0.517, 0.55, 30	no	1; no
S17, MS7	<i>C. elegans</i> 22°C L3 stage	GFP-laminin mCherry-moesinABD	97 x 97 x 180	34.9 x 68.3 x 30.2	(10ms, 10ms) (30pts, 30pts) (3.36s+115.5s)	488: (16) 560: (46)	0.517, 0.55, 30	no	1; no
MS8	<i>Arabidopsis</i> 22°C	P32S-GFP-MBD	97 x 97 x 180	34.9 x 68.3 x 40.1	20ms 120pts (4.46s+0.87s)	488: (32)	0.517, 0.55, 30	no	1; no

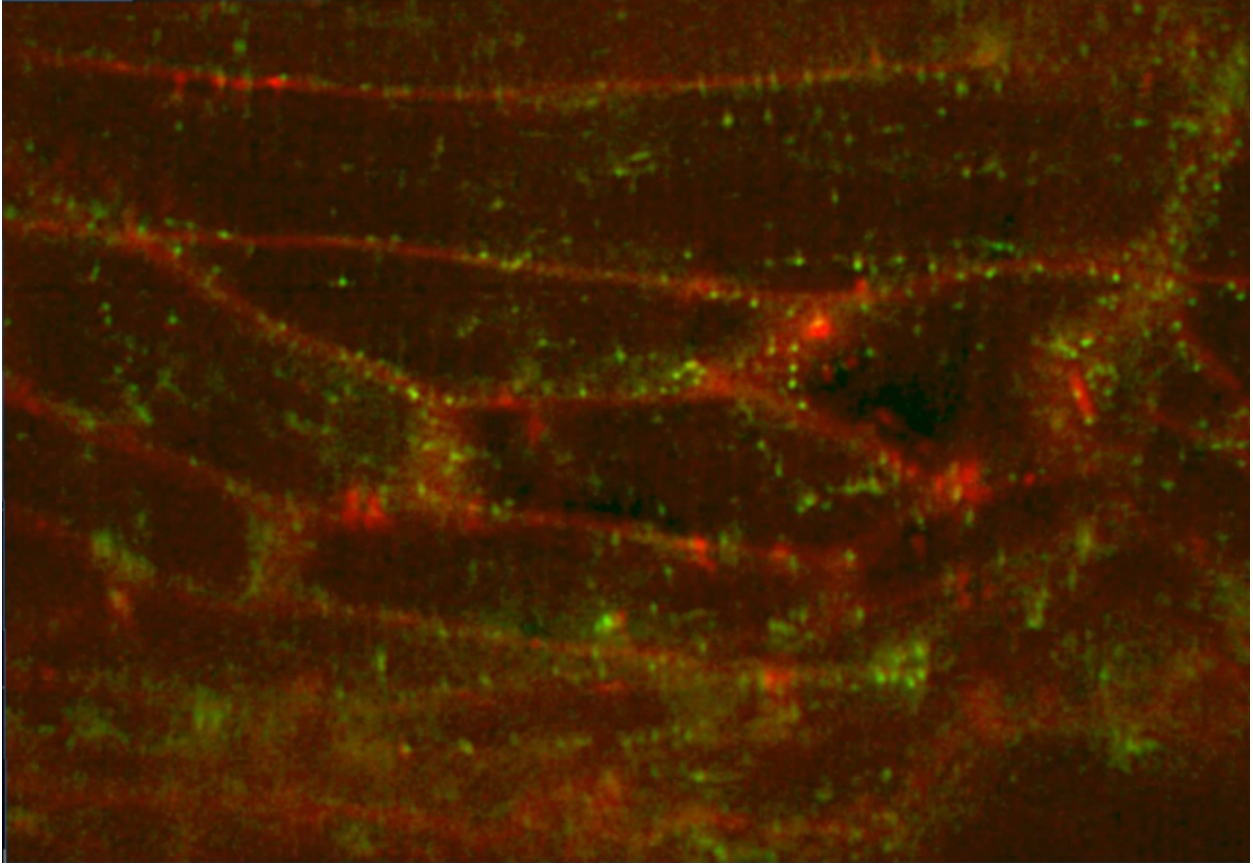
## Captions for Supplementary Movies



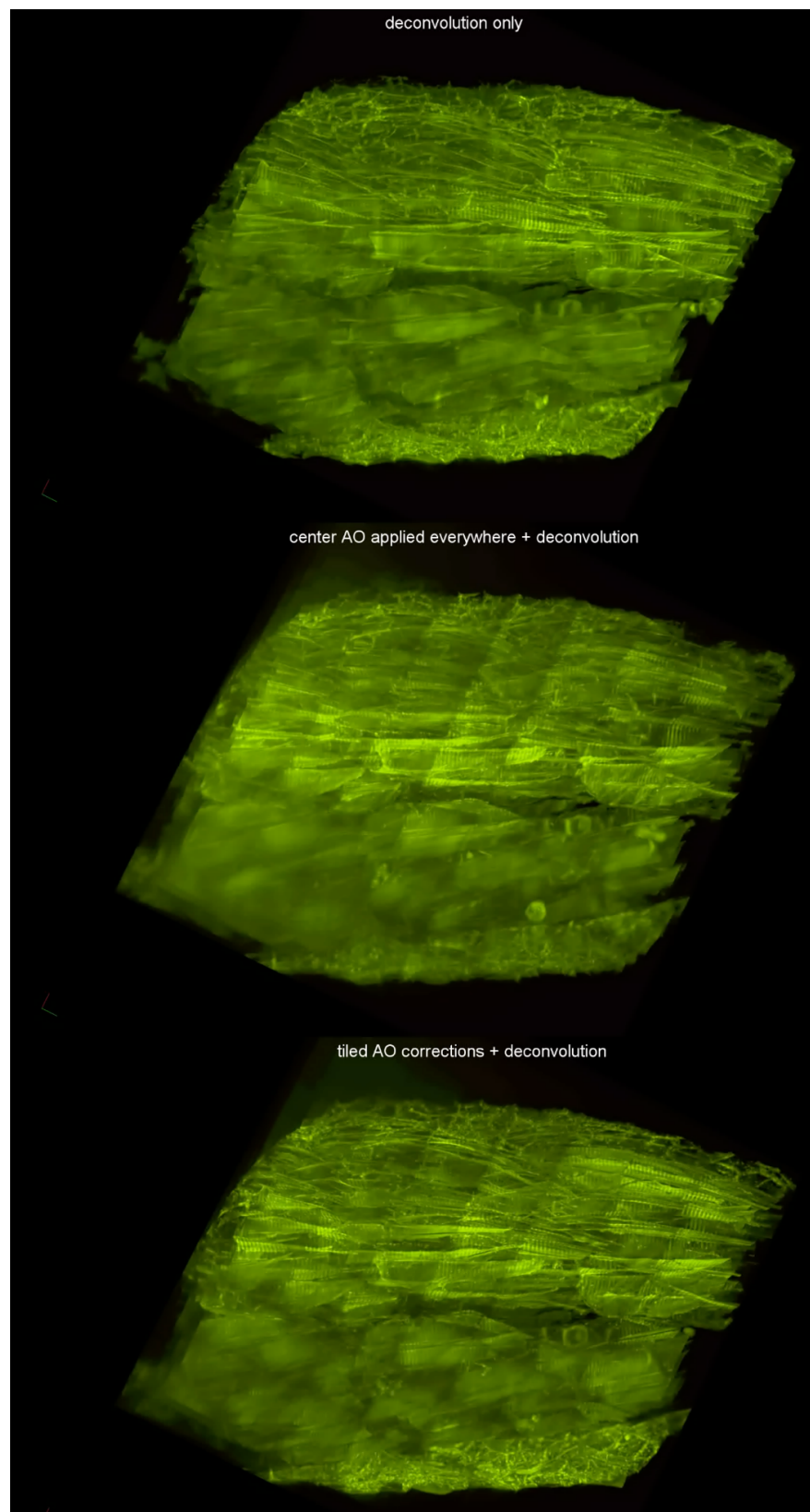
**Movie S1.** Volume rendering of 200 nm beads embedded in 1% agarose imaged with no correction (left) and with complete AO correction (detection, excitation and autofocus, right). The volume is rotated around the  $x$  axis showing its  $z$  and  $y$  projections (*c.f.*, Fig 1).



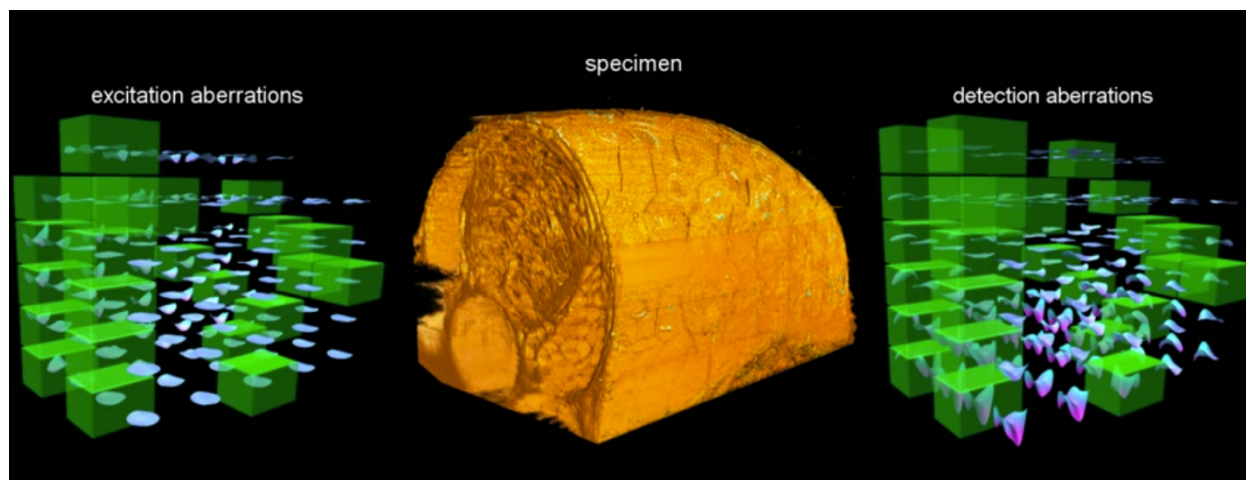
**Movie S2.** Subcellular structure and dynamics in the spine of a zebrafish embryo 24 hpf expressing markers for the cell surface (mCardinal-membrane), trans-Golgi apparatus (mNeonGreen-GalT) and mitochondria (TagRFpt-cox8a). Part 1 of the movie compares volume renderings at a single time point using unprocessed data, deconvolved data without AO correction, and deconvolved data with AO correction. Part 2 compares, at a single time point,  $xy$  maximum intensity projections of unprocessed data, data with AO correction only, and data with AO and deconvolution Part 3 shows the dynamics of the organelles after AO correction plus deconvolution (*c.f.*, Fig 1D).



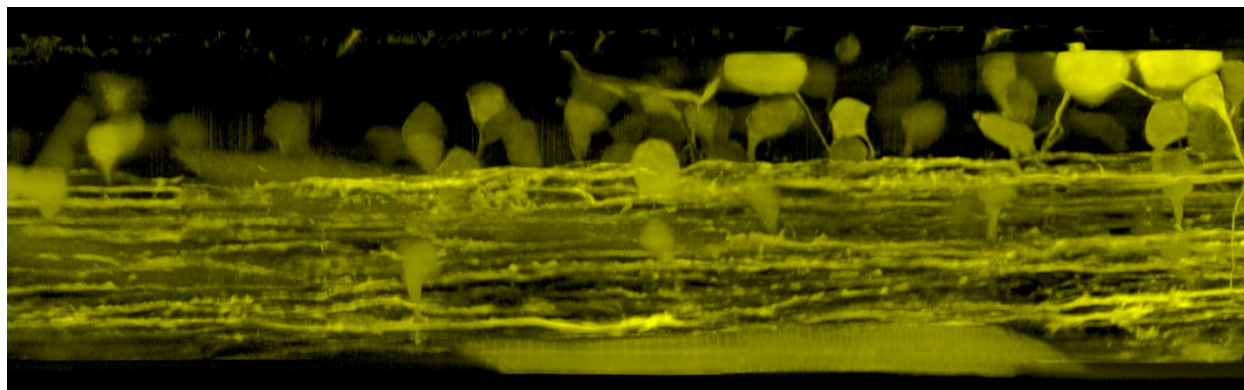
**Movie S3.** Dynamics of CCPs and CCVs (green) relative to muscle cell membranes, including their t-tubules (red), in a 2µm slab through the tail of a zebrafish embryo 50-55 hpf. Both CCPs pinned to t-tubules and CCVs rapidly shuttling between t-tubules along the fiber axis are observed. (*c.f.*, Fig. 2, Movie 3).



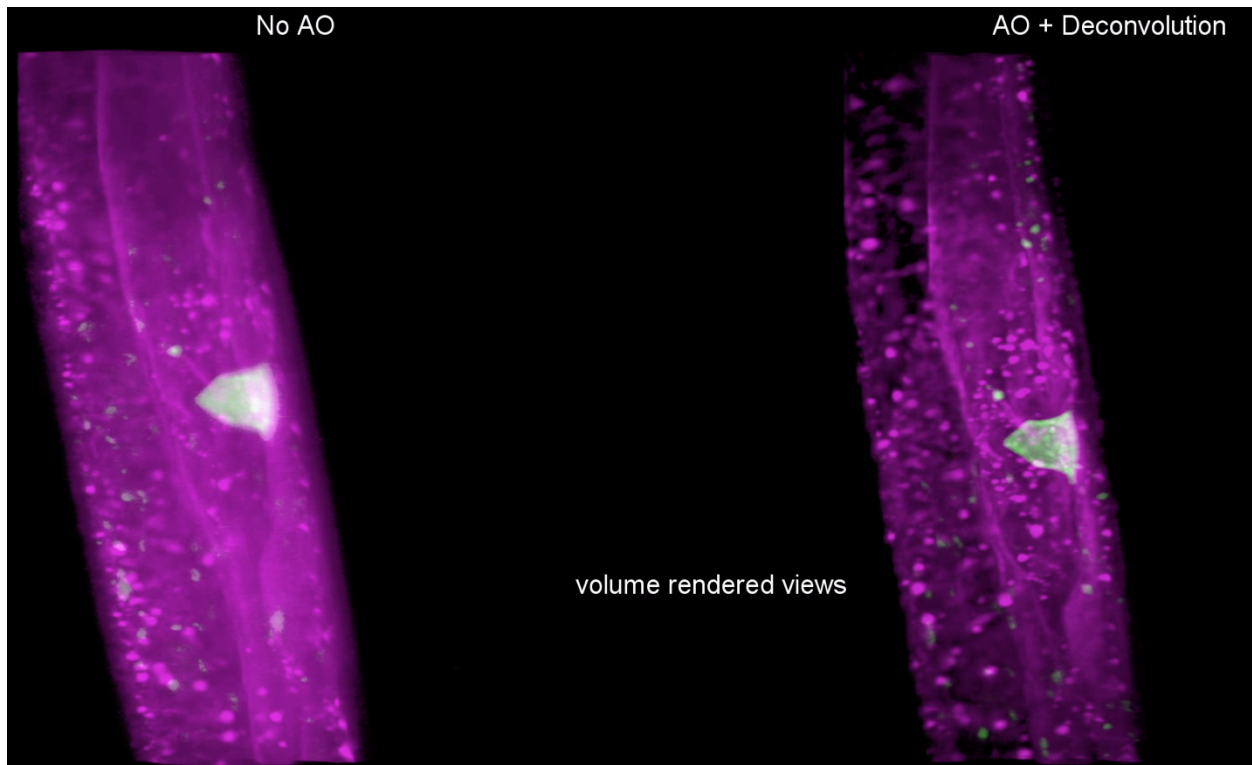
**Movie S4.** A large image volume assembled from 7 x 7 x 3 subvolumes in the tail of a zebrafish embryo 96 hpf comparing three stitched and deconvolved datasets: (top) no AO correction; (middle) AO correction from center tile applied to all tiles; and (bottom) independent correction applied to each tile (*c.f.*, fig 4).



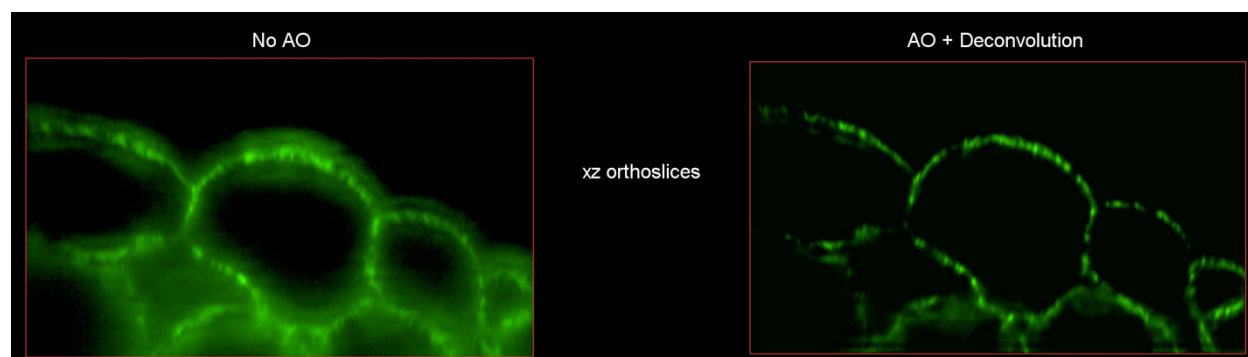
**Movie S5.** Volume rendered time series of zebrafish spine development from 30-34 hpf imaged at 30 min intervals. The excitation and detection path aberrations are shown on either side of the aberration corrected spine volume. The subset of tiles at a given time point where AO corrections are updated are highlighted with green boxes (*c.f.*, Fig 4D).



**Movie S6.** Sagittal view of the migration of rostrally projecting axons of newly differentiated neurons labeled by Autobow, imaged at 10.4 min intervals from 58 to 70 hpf (*c.f.*, Fig. 6A-C).



**Movie S7. Visualizing *C. elegans* AC invasion *in vivo*.** Basement membrane (magenta) and AC-specific F-actin (green) in the *C. elegans* L3 stage somatic gonad and vulval epithelium, prior to the time of AC invasion, showing  $xy$  and  $xz$  orthoslices and volume rendered views before (left) and after (right) AO correction and deconvolution (*c.f.*, fig S17).



**Movie S8.** *Arabidopsis* cotyledon epidermal cells expressing microtubule reporter *p35S::GFP-MBD*, showing *xy* and *xz* orthoslices and volume rendered views before (left) and after (right) AO correction and deconvolution (*c.f.*, fig. S18).

## References and Notes

1. J. Icha, M. Weber, J. C. Waters, C. Norden, Phototoxicity in live fluorescence microscopy, and how to avoid it. *BioEssays* **39**, 1700003 (2017). [doi:10.1002/bies.201700003](https://doi.org/10.1002/bies.201700003) [Medline](#)
2. P. P. Laissue, R. A. Alghamdi, P. Tomancak, E. G. Reynaud, H. Shroff, Assessing phototoxicity in live fluorescence imaging. *Nat. Methods* **14**, 657–661 (2017). [doi:10.1038/nmeth.4344](https://doi.org/10.1038/nmeth.4344) [Medline](#)
3. F. Pampaloni, E. G. Reynaud, E. H. Stelzer, The third dimension bridges the gap between cell culture and live tissue. *Nat. Rev. Mol. Cell Biol.* **8**, 839–845 (2007). [doi:10.1038/nrm2236](https://doi.org/10.1038/nrm2236) [Medline](#)
4. M. J. Pittet, R. Weissleder, Intravital imaging. *Cell* **147**, 983–991 (2011). [doi:10.1016/j.cell.2011.11.004](https://doi.org/10.1016/j.cell.2011.11.004) [Medline](#)
5. R. Weigert, M. Sramkova, L. Parente, P. Amornphimoltham, A. Masedunskas, Intravital microscopy: A novel tool to study cell biology in living animals. *Histochem. Cell Biol.* **133**, 481–491 (2010). [doi:10.1007/s00418-010-0692-z](https://doi.org/10.1007/s00418-010-0692-z) [Medline](#)
6. B. C. Chen, W. R. Legant, K. Wang, L. Shao, D. E. Milkie, M. W. Davidson, C. Janetopoulos, X. S. Wu, J. A. Hammer 3rd, Z. Liu, B. P. English, Y. Mimori-Kiyosue, D. P. Romero, A. T. Ritter, J. Lippincott-Schwartz, L. Fritz-Laylin, R. D. Mullins, D. M. Mitchell, J. N. Bembenek, A.-C. Reymann, R. Böhme, S. W. Grill, J. T. Wang, G. Seydoux, U. S. Tulu, D. P. Kiehart, E. Betzig, Lattice light-sheet microscopy: Imaging molecules to embryos at high spatiotemporal resolution. *Science* **346**, 1257998 (2014). [doi:10.1126/science.1257998](https://doi.org/10.1126/science.1257998) [Medline](#)
7. N. Ji, Adaptive optical fluorescence microscopy. *Nat. Methods* **14**, 374–380 (2017). [doi:10.1038/nmeth.4218](https://doi.org/10.1038/nmeth.4218) [Medline](#)
8. D. Wilding, P. Pozzi, O. Soloviev, G. Vdovin, M. Verhaegen, Adaptive illumination based on direct wavefront sensing in a light-sheet fluorescence microscope. *Opt. Express* **24**, 24896–24906 (2016). [doi:10.1364/OE.24.024896](https://doi.org/10.1364/OE.24.024896) [Medline](#)
9. C. Bourgenot, C. D. Saunter, J. M. Taylor, J. M. Girkin, G. D. Love, 3D adaptive optics in a light sheet microscope. *Opt. Express* **20**, 13252–13261 (2012). [doi:10.1364/OE.20.013252](https://doi.org/10.1364/OE.20.013252) [Medline](#)
10. R. Aviles-Espinosa, J. Andilla, R. Porcar-Guezenec, O. E. Olarte, M. Nieto, X. Levecq, D. Artigas, P. Loza-Alvarez, Measurement and correction of in vivo sample aberrations employing a nonlinear guide-star in two-photon excited fluorescence microscopy. *Biomed. Opt. Express* **2**, 3135–3149 (2011). [doi:10.1364/BOE.2.003135](https://doi.org/10.1364/BOE.2.003135) [Medline](#)
11. K. Wang, D. E. Milkie, A. Saxena, P. Engerer, T. Misgeld, M. E. Bronner, J. Mumm, E. Betzig, Rapid adaptive optical recovery of optimal resolution over large volumes. *Nat. Methods* **11**, 625–628 (2014). [doi:10.1038/nmeth.2925](https://doi.org/10.1038/nmeth.2925) [Medline](#)
12. L. A. Royer, W. C. Lemon, R. K. Chhetri, Y. Wan, M. Coleman, E. W. Myers, P. J. Keller, Adaptive light-sheet microscopy for long-term, high-resolution imaging in living organisms. *Nat. Biotechnol.* **34**, 1267–1278 (2016). [doi:10.1038/nbt.3708](https://doi.org/10.1038/nbt.3708) [Medline](#)

13. F. Arbizzani, M. Mayrhofer, M. Mione, Novel transgenic lines to fluorescently label clathrin and caveolin endosomes in live zebrafish. *Zebrafish* **12**, 202–203 (2015). [doi:10.1089/zeb.2015.1501](https://doi.org/10.1089/zeb.2015.1501) [Medline](#)
14. M. Ehrlich, W. Boll, A. Van Oijen, R. Hariharan, K. Chandran, M. L. Nibert, T. Kirchhausen, Endocytosis by random initiation and stabilization of clathrin-coated pits. *Cell* **118**, 591–605 (2004). [doi:10.1016/j.cell.2004.08.017](https://doi.org/10.1016/j.cell.2004.08.017) [Medline](#)
15. D. Li, L. Shao, B.-C. Chen, X. Zhang, M. Zhang, B. Moses, D. E. Milkie, J. R. Beach, J. A. Hammer 3rd, M. Pasham, T. Kirchhausen, M. A. Baird, M. W. Davidson, P. Xu, E. Betzig, Extended-resolution structured illumination imaging of endocytic and cytoskeletal dynamics. *Science* **349**, aab3500 (2015). [doi:10.1126/science.aab3500](https://doi.org/10.1126/science.aab3500) [Medline](#)
16. C. Kural, S. K. Tacheva-Grigorova, S. Boulant, E. Cocucci, T. Baust, D. Duarte, T. Kirchhausen, Dynamics of intracellular clathrin/AP1- and clathrin/AP3-containing carriers. *Cell Rep* **2**, 1111–1119 (2012). [doi:10.1016/j.celrep.2012.09.025](https://doi.org/10.1016/j.celrep.2012.09.025) [Medline](#)
17. S. Vassilopoulos, C. Gentil, J. Lainé, P.-O. Buclez, A. Franck, A. Ferry, G. Précigout, R. Roth, J. E. Heuser, F. M. Brodsky, L. Garcia, G. Bonne, T. Voit, F. Piétri-Rouxel, M. Bitoun, Actin scaffolding by clathrin heavy chain is required for skeletal muscle sarcomere organization. *J. Cell Biol.* **205**, 377–393 (2014). [doi:10.1083/jcb.201309096](https://doi.org/10.1083/jcb.201309096) [Medline](#)
18. F. Aguet, S. Upadhyayula, R. Gaudin, Y. Y. Chou, E. Cocucci, K. He, B.-C. Chen, K. Mosaliganti, M. Pasham, W. Skillern, W. R. Legant, T.-L. Liu, G. Findlay, E. Marino, G. Danuser, S. Megason, E. Betzig, T. Kirchhausen, Membrane dynamics of dividing cells imaged by lattice light-sheet microscopy. *Mol. Biol. Cell* **27**, 3418–3435 (2016). [doi:10.1091/mbc.E16-03-0164](https://doi.org/10.1091/mbc.E16-03-0164) [Medline](#)
19. Z. Kadlecova, S. J. Spielman, D. Loerke, A. Mohanakrishnan, D. K. Reed, S. L. Schmid, Regulation of clathrin-mediated endocytosis by hierarchical allosteric activation of AP2. *J. Cell Biol.* **216**, 167–179 (2017). [doi:10.1083/jcb.201608071](https://doi.org/10.1083/jcb.201608071) [Medline](#)
20. L. Lu, M. S. Ladinsky, T. Kirchhausen, Cisternal organization of the endoplasmic reticulum during mitosis. *Mol. Biol. Cell* **20**, 3471–3480 (2009). [doi:10.1091/mbc.E09-04-0327](https://doi.org/10.1091/mbc.E09-04-0327) [Medline](#)
21. E. Boucrot, T. Kirchhausen, Endosomal recycling controls plasma membrane area during mitosis. *Proc. Natl. Acad. Sci. U.S.A.* **104**, 7939–7944 (2007). [doi:10.1073/pnas.0702511104](https://doi.org/10.1073/pnas.0702511104) [Medline](#)
22. J. Icha, C. Kunath, M. Rocha-Martins, C. Norden, Independent modes of ganglion cell translocation ensure correct lamination of the zebrafish retina. *J. Cell Biol.* **215**, 259–275 (2016). [doi:10.1083/jcb.201604095](https://doi.org/10.1083/jcb.201604095) [Medline](#)
23. J. Sidhaye, C. Norden, Concerted action of neuroepithelial basal shrinkage and active epithelial migration ensures efficient optic cup morphogenesis. *eLife* **6**, e22689 (2017). [doi:10.7554/eLife.22689](https://doi.org/10.7554/eLife.22689) [Medline](#)
24. J. Icha, C. Schmied, J. Sidhaye, P. Tomancak, S. Preibisch, C. Norden, Using light sheet fluorescence microscopy to image zebrafish eye development. *J. Vis. Exp.* **110**, e53966 (2016).

25. F. C. Sauer, Mitosis in the neural tube. *J. Comp. Neurol.* **62**, 377–405 (1935).  
[doi:10.1002/cne.900620207](https://doi.org/10.1002/cne.900620207)
26. P. J. Strzyz, H. O. Lee, J. Sidhaye, I. P. Weber, L. C. Leung, C. Norden, Interkinetic nuclear migration is centrosome independent and ensures apical cell division to maintain tissue integrity. *Dev. Cell* **32**, 203–219 (2015). [doi:10.1016/j.devcel.2014.12.001](https://doi.org/10.1016/j.devcel.2014.12.001) [Medline](#)
27. L. A. Lowery, D. Van Vactor, The trip of the tip: Understanding the growth cone machinery. *Nat. Rev. Mol. Cell Biol.* **10**, 332–343 (2009). [doi:10.1038/nrm2679](https://doi.org/10.1038/nrm2679) [Medline](#)
28. D. Bentley, A. Toroian-Raymond, Disoriented pathfinding by pioneer neurone growth cones deprived of filopodia by cytochalasin treatment. *Nature* **323**, 712–715 (1986).  
[doi:10.1038/323712a0](https://doi.org/10.1038/323712a0) [Medline](#)
29. C. B. Chien, D. E. Rosenthal, W. A. Harris, C. E. Holt, Navigational errors made by growth cones without filopodia in the embryonic *Xenopus* brain. *Neuron* **11**, 237–251 (1993).  
[doi:10.1016/0896-6273\(93\)90181-P](https://doi.org/10.1016/0896-6273(93)90181-P) [Medline](#)
30. J. Q. Zheng, J. J. Wan, M. M. Poo, Essential role of filopodia in chemotropic turning of nerve growth cone induced by a glutamate gradient. *J. Neurosci.* **16**, 1140–1149 (1996).  
[Medline](#)
31. D. Cai, K. B. Cohen, T. Luo, J. W. Lichtman, J. R. Sanes, Improved tools for the Brainbow toolbox. *Nat. Methods* **10**, 540–547 (2013). [doi:10.1038/nmeth.2450](https://doi.org/10.1038/nmeth.2450)
32. A. Kinkhabwala, M. Riley, M. Koyama, J. Monen, C. Satou, Y. Kimura, S. Higashijima, J. Fetcho, A structural and functional ground plan for neurons in the hindbrain of zebrafish. *Proc. Natl. Acad. Sci. U.S.A.* **108**, 1164–1169 (2011). [doi:10.1073/pnas.1012185108](https://doi.org/10.1073/pnas.1012185108)  
[Medline](#)
33. S. de Oliveira, E. E. Rosowski, A. Huttenlocher, Neutrophil migration in infection and wound repair: Going forward in reverse. *Nat. Rev. Immunol.* **16**, 378–391 (2016).  
[doi:10.1038/nri.2016.49](https://doi.org/10.1038/nri.2016.49) [Medline](#)
34. N. Reymond, B. B. d'Água, A. J. Ridley, Crossing the endothelial barrier during metastasis. *Nat. Rev. Cancer* **13**, 858–870 (2013). [doi:10.1038/nrc3628](https://doi.org/10.1038/nrc3628) [Medline](#)
35. A. Marki, K. Buscher, Z. Mikulski, A. Pries, K. Ley, Rolling neutrophils form tethers and slings under physiologic conditions in vivo. *J. Leukoc. Biol.* **103**, 67–70 (2017).
36. K. Stoletov, H. Kato, E. Zardouzian, J. Kelber, J. Yang, S. Shattil, R. Klemke, Visualizing extravasation dynamics of metastatic tumor cells. *J. Cell Sci.* **123**, 2332–2341 (2010).  
[doi:10.1242/jcs.069443](https://doi.org/10.1242/jcs.069443) [Medline](#)
37. M. B. Ahrens, M. B. Orger, D. N. Robson, J. M. Li, P. J. Keller, Whole-brain functional imaging at cellular resolution using light-sheet microscopy. *Nat. Methods* **10**, 413–420 (2013). [doi:10.1038/nmeth.2434](https://doi.org/10.1038/nmeth.2434) [Medline](#)
38. R. Tomer, K. Khairy, F. Amat, P. J. Keller, Quantitative high-speed imaging of entire developing embryos with simultaneous multiview light-sheet microscopy. *Nat. Methods* **9**, 755–763 (2012). [doi:10.1038/nmeth.2062](https://doi.org/10.1038/nmeth.2062) [Medline](#)

39. R. K. Chhetri, F. Amat, Y. Wan, B. Höckendorf, W. C. Lemon, P. J. Keller, Whole-animal functional and developmental imaging with isotropic spatial resolution. *Nat. Methods* **12**, 1171–1178 (2015). [doi:10.1038/nmeth.3632](https://doi.org/10.1038/nmeth.3632) [Medline](#)
40. A. Kumar, Y. Wu, R. Christensen, P. Chandris, W. Gandler, E. McCreedy, A. Bokinsky, D. A. Colón-Ramos, Z. Bao, M. McAuliffe, G. Rondeau, H. Shroff, Dual-view plane illumination microscopy for rapid and spatially isotropic imaging. *Nat. Protoc.* **9**, 2555–2573 (2014). [doi:10.1038/nprot.2014.172](https://doi.org/10.1038/nprot.2014.172) [Medline](#)
41. J. Swoger, P. Verveer, K. Greger, J. Huisken, E. H. Stelzer, Multi-view image fusion improves resolution in three-dimensional microscopy. *Opt. Express* **15**, 8029–8042 (2007). [doi:10.1364/OE.15.008029](https://doi.org/10.1364/OE.15.008029) [Medline](#)
42. R. D. Simmonds, M. J. Booth, Modelling of multi-conjugate adaptive optics for spatially variant aberrations in microscopy. *J. Opt.* **15**, 094010 (2013). [doi:10.1088/2040-8978/15/9/094010](https://doi.org/10.1088/2040-8978/15/9/094010)
43. I. A. Swinburne, K. R. Mosaliganti, A. A. Green, S. G. Megason, Improved long-term imaging of embryos with genetically encoded  $\alpha$ -bungarotoxin. *PLOS ONE* **10**, e0134005 (2015). [doi:10.1371/journal.pone.0134005](https://doi.org/10.1371/journal.pone.0134005) [Medline](#)
44. H. I. Campbell, S. Zhang, A. H. Greenaway, S. Restaino, Generalized phase diversity for wave-front sensing. *Opt. Lett.* **29**, 2707–2709 (2004). [doi:10.1364/OL.29.002707](https://doi.org/10.1364/OL.29.002707) [Medline](#)
45. R. Gerchberg, W. Saxton, A practical algorithm for the determination of phase from image and diffraction plane pictures. *Optik* **35**, 237–246 (1972).
46. J. J. Dirckx, L. C. Kuypers, W. F. Decraemer, Refractive index of tissue measured with confocal microscopy. *J. Biomed. Opt.* **10**, 044014 (2005). [doi:10.1117/1.1993487](https://doi.org/10.1117/1.1993487) [Medline](#)
47. T. Boothe, L. Hilbert, M. Heide, L. Berninger, W. B. Huttner, V. Zaburdaev, N. L. Vastenhouw, E. W. Myers, D. N. Drechsel, J. C. Rink, A tunable refractive index matching medium for live imaging cells, tissues and model organisms. *eLife* **6**, e27240 (2017). [doi:10.7554/eLife.27240](https://doi.org/10.7554/eLife.27240) [Medline](#)
48. M. Westerfield, *The Zebrafish Book: A Guide for the Laboratory Use of Zebrafish* (Brachydanio rerio) (M. Westerfield, 1993).
49. F. Xiong, W. Ma, T. W. Hiscock, K. R. Mosaliganti, A. R. Tentner, K. A. Brakke, N. Rannou, A. Gelas, L. Souhait, I. A. Swinburne, N. D. Obholzer, S. G. Megason, Interplay of cell shape and division orientation promotes robust morphogenesis of developing epithelia. *Cell* **159**, 415–427 (2014). [doi:10.1016/j.cell.2014.09.007](https://doi.org/10.1016/j.cell.2014.09.007) [Medline](#)
50. F. Xiong, A. R. Tentner, P. Huang, A. Gelas, K. R. Mosaliganti, L. Souhait, N. Rannou, I. A. Swinburne, N. D. Obholzer, P. D. Cowgill, A. F. Schier, S. G. Megason, Specified neural progenitors sort to form sharp domains after noisy Shh signaling. *Cell* **153**, 550–561 (2013). [doi:10.1016/j.cell.2013.03.023](https://doi.org/10.1016/j.cell.2013.03.023) [Medline](#)
51. F. Knopf, K. Schnabel, C. Haase, K. Pfeifer, K. Anastassiadis, G. Weidinger, Dually inducible TetON systems for tissue-specific conditional gene expression in zebrafish.

- Proc. Natl. Acad. Sci. U.S.A.* **107**, 19933–19938 (2010). [doi:10.1073/pnas.1007799107](https://doi.org/10.1073/pnas.1007799107) [Medline](#)
52. H. C. Park, C.-H. Kim, Y.-K. Bae, S.-Y. Yeo, S.-H. Kim, S.-K. Hong, J. Shin, K.-W. Yoo, M. Hibi, T. Hirano, N. Miki, A. B. Chitnis, T.-L. Huh, Analysis of upstream elements in the HuC promoter leads to the establishment of transgenic zebrafish with fluorescent neurons. *Dev. Biol.* **227**, 279–293 (2000). [doi:10.1006/dbio.2000.9898](https://doi.org/10.1006/dbio.2000.9898) [Medline](#)
53. C. H. Kim, E. Ueshima, O. Muraoka, H. Tanaka, S.-Y. Yeo, T.-L. Huh, N. Miki, Zebrafish elav/HuC homologue as a very early neuronal marker. *Neurosci. Lett.* **216**, 109–112 (1996). [doi:10.1016/0304-3940\(96\)13021-4](https://doi.org/10.1016/0304-3940(96)13021-4) [Medline](#)
54. K. Kawakami, Transgenesis and gene trap methods in zebrafish by using the Tol2 transposable element. *Methods Cell Biol.* **77**, 201–222 (2004). [doi:10.1016/S0091-679X\(04\)77011-9](https://doi.org/10.1016/S0091-679X(04)77011-9) [Medline](#)
55. D. G. Gibson, L. Young, R.-Y. Chuang, J. C. Venter, C. A. Hutchison 3rd, H. O. Smith, Enzymatic assembly of DNA molecules up to several hundred kilobases. *Nat. Methods* **6**, 343–345 (2009). [doi:10.1038/nmeth.1318](https://doi.org/10.1038/nmeth.1318) [Medline](#)
56. J. Choi, L. Dong, J. Ahn, D. Dao, M. Hammerschmidt, J.-N. Chen, FoxH1 negatively modulates *flkl1* gene expression and vascular formation in zebrafish. *Dev. Biol.* **304**, 735–744 (2007). [doi:10.1016/j.ydbio.2007.01.023](https://doi.org/10.1016/j.ydbio.2007.01.023) [Medline](#)
57. D. Hockemeyer, H. Wang, S. Kiani, C. S. Lai, Q. Gao, J. P. Cassady, G. J. Cost, L. Zhang, Y. Santiago, J. C. Miller, B. Zeitler, J. M. Cherone, X. Meng, S. J. Hinkley, E. J. Rebar, P. D. Gregory, F. D. Urnov, R. Jaenisch, Genetic engineering of human pluripotent cells using TALE nucleases. *Nat. Biotechnol.* **29**, 731–734 (2011). [doi:10.1038/nbt.1927](https://doi.org/10.1038/nbt.1927) [Medline](#)
58. F. Soldner, D. Hockemeyer, C. Beard, Q. Gao, G. W. Bell, E. G. Cook, G. Hargus, A. Blak, O. Cooper, M. Mitalipova, O. Isacson, R. Jaenisch, Parkinson’s disease patient-derived induced pluripotent stem cells free of viral reprogramming factors. *Cell* **136**, 964–977 (2009). [doi:10.1016/j.cell.2009.02.013](https://doi.org/10.1016/j.cell.2009.02.013) [Medline](#)
59. J. B. Doyon, B. Zeitler, J. Cheng, A. T. Cheng, J. M. Cherone, Y. Santiago, A. H. Lee, T. D. Vo, Y. Doyon, J. C. Miller, D. E. Paschon, L. Zhang, E. J. Rebar, P. D. Gregory, F. D. Urnov, D. G. Drubin, Rapid and efficient clathrin-mediated endocytosis revealed in genome-edited mammalian cells. *Nat. Cell Biol.* **13**, 331–337 (2011). [doi:10.1038/ncb2175](https://doi.org/10.1038/ncb2175) [Medline](#)
60. D. Dambournet, S. H. Hong, A. Grassart, D. G. Drubin, Tagging endogenous loci for live-cell fluorescence imaging and molecule counting using ZFNs, TALENs, and Cas9. *Methods Enzymol.* **546**, 139–160 (2014). [doi:10.1016/B978-0-12-801185-0.00007-6](https://doi.org/10.1016/B978-0-12-801185-0.00007-6) [Medline](#)
61. R. Forster, K. Chiba, L. Schaeffer, S. G. Regalado, C. S. Lai, Q. Gao, S. Kiani, H. F. Farin, H. Clevers, G. J. Cost, A. Chan, E. J. Rebar, F. D. Urnov, P. D. Gregory, L. Pachter, R. Jaenisch, D. Hockemeyer, Human intestinal tissue with adult stem cell properties derived from pluripotent stem cells. *Stem Cell Rep.* **2**, 838–852 (2014). [doi:10.1016/j.stemcr.2014.05.001](https://doi.org/10.1016/j.stemcr.2014.05.001) [Medline](#)

62. H. Miyoshi, T. S. Stappenbeck, In vitro expansion and genetic modification of gastrointestinal stem cells in spheroid culture. *Nat. Protoc.* **8**, 2471–2482 (2013). [doi:10.1038/nprot.2013.153](https://doi.org/10.1038/nprot.2013.153) [Medline](#)
63. S. Brenner, The genetics of *Caenorhabditis elegans*. *Genetics* **77**, 71–94 (1974). [Medline](#)
64. E. J. Hagedorn, J. W. Ziel, M. A. Morrissey, L. M. Linden, Z. Wang, Q. Chi, S. A. Johnson, D. R. Sherwood, The netrin receptor DCC focuses invadopodia-driven basement membrane transmigration in vivo. *J. Cell Biol.* **201**, 903–913 (2013). [doi:10.1083/jcb.201301091](https://doi.org/10.1083/jcb.201301091) [Medline](#)
65. J. Marc, C. L. Granger, J. Brincat, D. D. Fisher, Th. Kao, A. G. McCubbin, R. J. Cyr, A GFP-MAP4 reporter gene for visualizing cortical microtubule rearrangements in living epidermal cells. *Plant Cell* **10**, 1927–1940 (1998). [Medline](#)
66. S. Preibisch, S. Saalfeld, P. Tomancak, Globally optimal stitching of tiled 3D microscopic image acquisitions. *Bioinformatics* **25**, 1463–1465 (2009). [doi:10.1093/bioinformatics/btp184](https://doi.org/10.1093/bioinformatics/btp184) [Medline](#)
67. M. Kazhdan, D. Surendran, H. Hoppe, Distributed gradient-domain processing of planar and spherical images. *ACM Trans. Graph.* **29**, 14 (2010).
68. M. Kazhdan, K. Lillaney, W. Roncal, D. Bock, J. Vogelstein, R. Burns, Gradient-domain fusion for color correction in large EM image stacks. [arXiv:1506.02079](https://arxiv.org/abs/1506.02079) [cs.GR] (5 June 2015).
69. K. R. Mosaliganti, R. R. Noche, F. Xiong, I. A. Swinburne, S. G. Megason, ACME: Automated cell morphology extractor for comprehensive reconstruction of cell membranes. *PLOS Comput. Biol.* **8**, e1002780 (2012). [doi:10.1371/journal.pcbi.1002780](https://doi.org/10.1371/journal.pcbi.1002780) [Medline](#)
70. P. A. Yushkevich, J. Piven, H. C. Hazlett, R. G. Smith, S. Ho, J. C. Gee, G. Gerig, User-guided 3D active contour segmentation of anatomical structures: Significantly improved efficiency and reliability. *Neuroimage* **31**, 1116–1128 (2006). [doi:10.1016/j.neuroimage.2006.01.015](https://doi.org/10.1016/j.neuroimage.2006.01.015) [Medline](#)
71. J. Schindelin, I. Arganda-Carreras, E. Frise, V. Kaynig, M. Longair, T. Pietzsch, S. Preibisch, C. Rueden, S. Saalfeld, B. Schmid, J.-Y. Tinevez, D. J. White, V. Hartenstein, K. Eliceiri, P. Tomancak, A. Cardona, Fiji: An open-source platform for biological-image analysis. *Nat. Methods* **9**, 676–682 (2012). [doi:10.1038/nmeth.2019](https://doi.org/10.1038/nmeth.2019) [Medline](#)
72. A. Parslow, A. Cardona, R. J. Bryson-Richardson, Sample drift correction following 4D confocal time-lapse imaging. *J. Vis. Exp.* **86**, e51086 (2014).
73. K. Jaqaman, D. Loerke, M. Mettlen, H. Kuwata, S. Grinstein, S. L. Schmid, G. Danuser, Robust single-particle tracking in live-cell time-lapse sequences. *Nat. Methods* **5**, 695–702 (2008). [doi:10.1038/nmeth.1237](https://doi.org/10.1038/nmeth.1237) [Medline](#)
74. Y. Mishchenko, A fast algorithm for computation of discrete Euclidean distance transform in three or more dimensions on vector processing architectures. *Signal Image Video Process.* **9**, 19–27 (2015). [doi:10.1007/s11760-012-0419-9](https://doi.org/10.1007/s11760-012-0419-9)
75. W. H. Southwell, Wave-front estimation from wave-front slope measurements. *J. Opt. Soc. Am.* **70**, 998–1006 (1980). [doi:10.1364/JOSA.70.000998](https://doi.org/10.1364/JOSA.70.000998)